Correlation between Structural Properties and Intermolecular Coupling in Molecular Donor/Acceptor Thin Film Heterostructures

Dissertation
der Mathematisch-Naturwissenschaftlichen Fakultät
der Eberhard Karls Universität Tübingen
zur Erlangung des Grades eines
Doktors der Naturwissenschaften
(Dr. rer. nat.)

vorgelegt von
Valentina Belova
aus Nischni Nowgorod
Russland

Tübingen
2018

Gedruckt mit Genehmigung der Mathematisch-Naturwissenschaftlichen Fakultät der Eberhard Karls Universität Tübingen.

Tag der mündlichen Qualifikation:		23.10.2018
Dekan:		Prof. Dr. Wolfgang Rosenstiel
1.	Berichterstatter:	Prof. Dr. Frank Schreiber
2.	Berichterstatter:	Prof. Dr. Martin Oettel

CONTENTS

I. Fundamentals 1

1 Introduction 3

2 Organic Semiconductors 7
2.1 Structure and Properties of Organic Compounds 7
2.1.1 Molecular Electronic Structure and Energy Levels 7
2.1.2 sp^2 Hybridization in Conjugated Molecules 8
2.1.3 Excitation and Deactivation Processes 9
2.2 Noncovalent Intermolecular Interactions 11
2.3 Intermolecular Coupling in Organic Assemblies 13
2.3.1 Kasha's Model 13
2.3.2 Charge Transfer 15

3 Experimental Methods 19
3.1 Sample Preparation by Organic Molecular Beam Deposition (OMBD) 19
3.2 X-Ray Diffraction Techniques 21
3.3 Optical Spectroscopy 24
3.3.1 Variable Angle Spectroscopic Ellipsometry (VASE) 24
3.3.2 Photoluminescence (PL) Spectroscopy 25
3.3.3 Differential Reflectance Spectroscopy (DRS) 26
3.4 Further Methods 28
3.4.1 Morphology and IR/NIR/Vis/UV Spectroscopies 28
3.4.2 Ultraviolet Photoelectron Spectroscopy (UPS) 28
3.4.3 Device Fabrication and Characterization 29
3.4.4 Near-Edge X-ray Absorption Fine Structure (NEXAFS) 29

4 Materials 31
4.1 Donors: Diindenoperylene (DIP) and Pentacene (PEN) 31
4.2 Acceptors: Perylene Diimide Derivatives PDIR-CN_2 and PDIF-CN_2 33

II. Results and Discussion 37

5 Growth and Packing Behavior of PDIR-CN_2 and PDIF-CN_2 Thin Films 39
5.1 Structural Investigation by X-Ray Diffraction 39
5.2 Optical Absorption Spectra 46
5.3 Real-Time Study: GIXD and DRS 47
5.4 Photoluminescence 51

5.5 Morphology 53
5.6 Discussion 55

6 Anisotropic Electronic Coupling of Charge Transfer States in DIP:PDIR-CN_2 59
6.1 Structural Characterization 59
6.2 Ground State Properties 66
6.3 Excited State Properties 70
6.4 Device Behavior 76
6.5 Discussion 78

7 Structure-Dependent Charge Transfer in DIP/PEN – PDIR-CN_2/PDIF-CN_2 Systems 81
7.1 Structure Analysis 81
7.2 FTIR Measurements 83
7.3 Optical Absorption and Emission Spectra 84
7.4 AFM Images of 1:1 Mixtures 86
7.5 DRS on 1:1 Mixtures 88
7.6 Structure – CT Properties in DIP:PDIF-CN_2 90
7.7 Discussion 92

III. Conclusion and Outlook 97

8 Summary and Conclusion 99
8.1 Results on Acceptor Materials 99
8.2 Results on CT Complex Formation in DIP:PDIR-CN_2 100
8.3 Overview of Four *D*/*A* Systems 101
8.4 Outlook 102

Appendices 105

Appendix A 105
Appendix B 107
Appendix C 111

List of Abbreviations 113

Bibliography 117

List of Publications 137

Deutsche Zusammenfassung 139

Acknowledgments 141

Part I

Fundamentals

Chapter 1

Introduction

The section is based on the introductory parts of Refs. [1,2].

Organic semiconductors (OSCs, i. e. small molecules along with polymers) as active layers in organic field-effect transistors (OFETs) [3–5], photovoltaic devices (OPV) [6–8], and light-emitting diodes (OLEDs) [9,10] provide not only benefits such as high efficiency, low costs [11], processability, and device flexibility, but also uncountable possibilities for tuning their optoelectronic properties in a controlled way. The most obvious and most frequently explored approach for this is the modification of the chemical structure of these compounds. One can distinguish roughly two strategies of molecular modification: a) a direct change of the electronic properties of the compound, for instance by fluorination, b) a change of the geometry of the compound to modify the crystal packing, which has indirectly an impact on the film properties.

Fluorination is commonly applied to shift both ionization energy (IE) and electron affinity (EA) to lower energies in order to create efficient n-type semiconductors with low electron injection barriers and high electron mobilities [10,12–16]. Partial fluorination generally improves thermal, air and photostability [17–19] and can induce non-covalent bonding between fluorinated and non-fluorinated parts and thus favor the crystallization process [20–23]. Furthermore, the molecular packing in the solid state is governed by a balance of interactions, including a combination of quadrupolar stabilization, van der Waals forces and steric requirements [24,25]. Chemical modification by highly polar substituents or by spacer groups (e.g. side chains) often leads to a change of the intermolecular coupling in solids [26–31] and in the adsorption behavior on substrates [32,33], which in turn determines the device performance [34–36]. For thin film growth via organic molecular beam deposition (OMBD), also the preparation conditions such as deposition rate, substrate temperature and base pressure are crucial [37–39] and have a strong impact on the growth.

One of the fundamental processes in devices based on organic semiconductors is the charge transfer (CT) between electron donor (*D*) and electron acceptor (*A*) molecules at interfaces or in molecular mixed systems [9,40–42]. The concept of CT as a mechanism of intermolecular interaction was described in the framework of Mulliken theory in the 1950s [43,44]. In this theory, a donor and an acceptor form a CT complex, where the energy levels of ground and excited states depend on the overlap of the *D*/*A* wave functions and an electronic transition to the excited state is accompanied by partial or integer charge transfer.

The presence of CT interaction between donor and acceptor materials has recently attracted attention due to its importance for organic solar cells and organic light-emitting diodes [45–47] as well as the associated fundamental challenges. It was shown, e.g., that

the CT energy can serve as a limit for the open circuit voltage in solar cells [48,49]. However, even if the resulting exciton has charge transfer character, ground-state interactions are still present [50,51]. This complex process mediates both excitation and recombination of charge carries and, therefore, its mechanism needs to be explicitly understood.

The most explored approach in the field of OPV devices over the last couple decades has employed polymer/fullerene (or derivatives) combinations [52–56]. However, despite the trustworthy results on efficiency up to 10 % fullerene-based solar cells meet a number of limitations, making room for a search of new solutions among small molecule semiconductors [6,57–60]. Organic small molecule semiconductors provide countless possibilities for tailoring of device properties. By choosing different organic compounds the resulting energy gap (ΔE_{DA}) between a donor ionization energy (IE) and an acceptor electron affinity (EA) can be tuned in a desirable way: on the one hand, the larger ΔE_{DA} results in a higher open circuit voltage (V_{OC}) [61] and smaller non-radiative energy losses (in absence of morphology influence) [62], on the other hand, a direct excitation of low-lying CT states leads to broadening of the optical absorption wavelength range in the near-infrared region most favorable for solar energy harvesting [63]. However, the CT states might serve as efficient recombination channels for excitons [64–67]. This aspect is particularly important to be taken into consideration when designing an active layer in a bulk (planar-mixed) heterojunction (BHJ) configuration. Compared with planar heterojunctions (PHJ), the BHJ configurations provide larger interface area between donor and acceptor and are therefore more favorable in terms of photon to charge carrier quantum yield. However, in this case the morphology of the mixed layer plays a crucial role [68,69]. First of all, lattice disorder introduces numerous ingap trap states hindering charge transport [70]. Another factor is the nucleation of one of the pure phases, in particular an acceptor phase, along with the presence of a mixed phase and is considered as a beneficial condition for increasing charge separation rates [71,72]. A higher dielectric constant lowers the Coulomb exciton binding energy facilitating exciton dissociation [73]. Furthermore, crystalline domains of pure phases provide percolation pathways for delivering charge carriers to the electrodes [74]. In order to minimize exciton trapping at grain boundaries, the grain size should not be smaller than the average exciton diffusion length L_D in single-crystalline thin-films of 20-30 nm [35,75,76]. Thus, processes of intermixing, phase separation, crystallization in binary molecular mixtures of donor and acceptor species, and the correlation with formation of CT complexes require an explicit investigation.

The previous studies carried out in these frames considered aspects of sterical compatibility in two-phase mixed systems, which is the dominating factor for phase segregation when the components differ in the geometry and shape (e. g. fullerenes mixed with rod-like molecules or planar tile-shaped molecules) [77]. Even a deviation of a conjugated core length or an alternating aromatic ring fusion induces nucleation of the pure phases [78,79]. However, when mixing electron-donating (donor) and electron-withdrawing (acceptor) species an additional electrostatic attraction component plays a role of a stabilizing force for the co-crystal [80,81]. The competition of different kind of intermolecular interactions is therefore of great interest for *D*/*A* blends.

When considering *D*/*A* interfaces in a simplified view, one can distinguish three nominal cases of CT systems depending on the degree of intermolecular interaction (Figure 1.1). To the first category (Figure 1.1a), one may assign systems where the intermolecular energy gap ΔE_{DA} between the highest occupied molecular orbital (HOMO) of a donor and the lowest unoccupied molecular orbital (LUMO) of an acceptor are almost identical to the individual energy gaps of the donor ΔE_D or the acceptor ΔE_A [82]. Thus, CT in the electronic ground state (GS-CT) is unlikely to be observed, and integer charges are mainly transferred due to exciton (*D** and *A** states) formation and dissociation. As examples the material combinations employed for planar heterojunction (PHJ) solar cells such as α-sexithiophene (6T)/diindenoperylene (DIP) [83], 6T/tetra-phenyldibenzoperiflanthene (DBP) [84] and DBP/zinc chlorodipyrrin (ZCl) [85] can be considered. A second category (Figure 1.1b) describes weakly coupled molecules, where $\Delta E_{DA} < \Delta E_D$ or ΔE_A. These weakly bound complexes result, on average, in a partial charge transfer from the donor to the acceptor in the ground state and the CT state can be directly excited, but the molecular orbitals do not undergo a significant change. Examples for such mixed molecular systems are DIP:fullerene (C_{60}) [86], DBP:C_{60} [84], DIP:N,N′-dioctyl-3,4,9,10-perylene tetracarboxylicdiimide (PTCDI-C_8) [87], N,N'-bis(1-naphthyl)-N,N'-diphenyl-1,1'-biphenyl-4,4'-diamine (NPD):C_{60} [88]. In a third category (Figure 1.1c), there are systems with stronger intermolecular coupling, where ΔE_{DA} is insignificant compared to the optical gap of each component, ΔE_D or ΔE_A. In this case, the formation of hybridized molecular orbitals with an energy splitting ΔE^{CPX} can be observed, as has been shown for quaterthiophene (4T): 2,3,5,6-tetrafluoro-7,7,8,8-tetracyanoquinodimethane (F_4-TCNQ) [89], pentacene (PEN):F_4-TCNQ [90] or picene (PIC):F_4-TCNQ [91].

Note that the three different scenarios presented in Figure 1.1 change gradually from one to another and sharp boundaries are difficult to define. As an additional criterion for

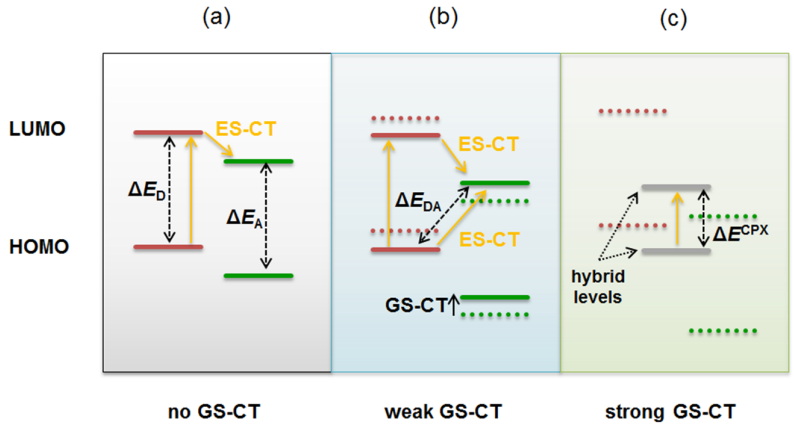


Figure 1.1: Simplified schematic illustration of possible scenarios for energy levels at interfaces. (a) $\Delta E_{DA} \approx \Delta E_D$ or ΔE_A, no ground state interaction present, charges are transferred through preliminary formed molecular excitons (*D** or *A**), yellow arrows depict electron transitions; (b) $\Delta E_{DA} < \Delta E_D$ or ΔE_A, weakly coupled molecules, partial GS-CT contributes to energy level shift, original levels are dotted, CT can occur either under direct excitation or via exciton dissociation; (c) $\Delta E_{DA} << \Delta E_D$ or ΔE_A, strong ground state interaction, orbital hybridization resulting in energy splitting of a CT complex (ΔE^{CPX}) is observed. Note that the full picture may be more complex, and that for electronic transitions the exciton binding energy must be taken into account [82].

classification one may consider the strength of the direct absorption into a CT state, e.g. a very weak CT absorption may be observed for type (a) requiring highly sensitive techniques, whereas type (b) reveals relatively strong CT bands detectable with standard ultraviolet-visible-near infrared (UV/Vis/NIR) absorption spectroscopy. So far, photoinduced CT via singlet exciton formation and dissociation (as in (a)) [92] and CT doping (as in (c)) [93] are widely discussed in the literature. However, the focus is here on the type (b) (weak ground state interaction – strong excited state interaction) and its fundamental characteristics since the complete understanding of the CT mechanism in this type of systems has not been achieved yet.

This thesis presents a comprehensive study on the intermolecular interactions and CT mechanism in organic binary mixtures in thin films prepared by vacuum deposition starting from morphological and structural investigations, via complementary forms of spectroscopy to the implications in device applications. As a case study, thin films of the small-molecule semiconductors DIP with PEN as donors and N,N′-bis-(2-ethylhexyl)-1,7-dicyanoperylene-3,4:9,10-bis(dicarboxyimide) (PDIR-CN_2 where R = C_8H_{17} branched) with N,N′-1H,1H-perfluorobutyl-dicyanoperylene-3,4:9,10-bis(dicarboxyimide) (PDIF-CN_2 with $C_4F_7H_2$ linear side substituents) as acceptors were chosen. Motivation for the material choice is rationalized in Chapter 4.

The thesis is organized as follows. Chapter 2 reviews basic physical phenomena and kinds of intermolecular interactions in OSCs. The experimental techniques, as well as sample preparation details, are provided in Chapter 3. Introductory information about materials studied here is combined in Chapter 4. Chapter 5 is devoted to investigation of properties of the pristine acceptor materials in thin films in dependence on growth temperature. The influence of the side substituents on the structural and optical properties is examined. Chapter 6 elucidates formation of a CT complex in the DIP:PDIR-CN_2 system observed for the electronic ground and excited states and its impact on the devices performance and anisotropy of the CT transition. A detailed comparison between four *D*/*A* systems is given in Chapter 7. A correlation between intermolecular coupling, mixing behavior and a CT complex formation is found. Finally, the findings are summarized in the "Summary and Conclusion" section.

CHAPTER 2

ORGANIC SEMICONDUCTORS

2.1 Structure and Properties of Organic Compounds

2.1.1 Molecular Electronic Structure and Energy Levels

Organic molecules consist of atoms held together by strong covalent bonds. Formation of the covalent bonds can be described by two basic theories: a) valence bond (VB) theory and b) molecular orbital (MO) theory. The VB approach is based on an assumption that a covalent bond is formed by overlap of the atomic orbitals of the dissociated atoms and the electronic pair is localized in the overlap region [94,95]. On the contrary, the MO theory describes molecules in a similar way to atoms with electrons distributed between a set of the molecular orbitals and delocalized over adjacent atoms [96]. One of the different approximations applicable for MO calculation is the linear combination of atomic orbitals (LCAO), which can be considered in the simplest case as the hydrogen molecules H_2. Here, the linear combination of two atomic 1*s*-orbitals can be achieved by their addition and subtraction (Figure 2.1).

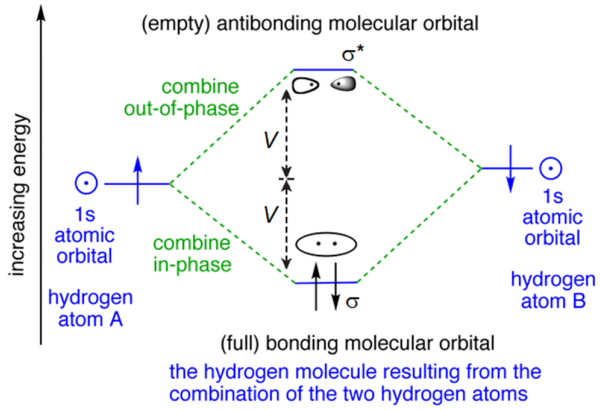


Figure 2.1: Atomic and molecular orbitals in H_2; *V* is the transfer or resonance integral; ovals indicate regions of isosurfaces, i. e. surfaces where the probability of finding an electron is the same.

The resulting orbitals σ and σ^* (also called as bonding and antibonding MOs) correspond to the electronic ground and the first excited state of the molecule. A transfer integral *V* determines the energy stabilizing the electron when the covalent bond is formed. Generally, the number of molecular orbitals is equal to the number of atomic orbitals that are used to form the molecular orbitals. Electrons fill the MOs in order of lower to higher energy according to the Pauli exclusion principle [97]. Thus, when describing a molecule's

electronic structure, the following frontier orbital definitions are used: the HOMO and the LUMO. These orbitals are separated in energy by the energy gap ΔE, whose size is determined by the molecule's nature.

The total energy of a free molecule (non-interacting with the environment) is the sum of the electronic, nuclear, vibrational and rotational components:

$$E = E_{el} + E_{n} + E_{vib} + E_{rot}, \tag{2.1}$$

where each component depends on the coordinates and motion rates of the corresponding particles. The very different time scales of the various types of motion in a molecule lead to substantial energy differences between the series of molecular energy levels in which the components are quantized, allowing to consider each of them separately (Table 2.1) (this approach is known as the Born-Oppenheimer-approximation [98]).

The first ionization potential or the ionization energy (IE) of a molecule in gas phase represents the minimal energy required to move an electron to the vacuum with zero kinetic energy and generate a cation. The electron affinity (EA) in gas phase is defined as an energy release upon the addition of an electron and formation of an anion. These negative values can be considered as the energies of the HOMO and LUMO levels correspondingly.

Table 2.1. Typical time and energy scales of different types of motion.

Motion/Transitions	Time scale	Energy Scale	Region of electro-magnetic spectrum
nuclear spin in magnetic field	1-100 μs	E_n < 0.4 μeV	radio
rotational	0.1 – 1 fs	E_{rot} = 0.12-12 meV	microwave
vibrational	10 – 100 fs	E_{vib}= 37-370 meV	infrared
electronic	0.1 – 10 ps	E_{el} > 0.62 eV	NIR-Vis-UV

2.1.2 sp^2 Hybridization in Conjugated Molecules

The basic element of organic compounds is carbon. The outermost shell of a carbon atom has two unpaired electrons (Figure 2.2a). However, in most organic compounds carbon has four valent orbitals and a changed configuration in the bound state (Figure 2.2b). In conjugated molecules, the carbon atoms are held together by σ-bonds which involve each one of the three sp^2 hybrid orbitals (ring or chain backbone) and a π-bond formed by an overlap of the p_z orbitals (Figure 2.2c,d). In an aromatic molecule, the electrons of the overlapping p_z orbitals undergo delocalization, i.e. a homogeneous distribution of the electron wavefunction over the whole molecule with formation of a π-electron cloud.

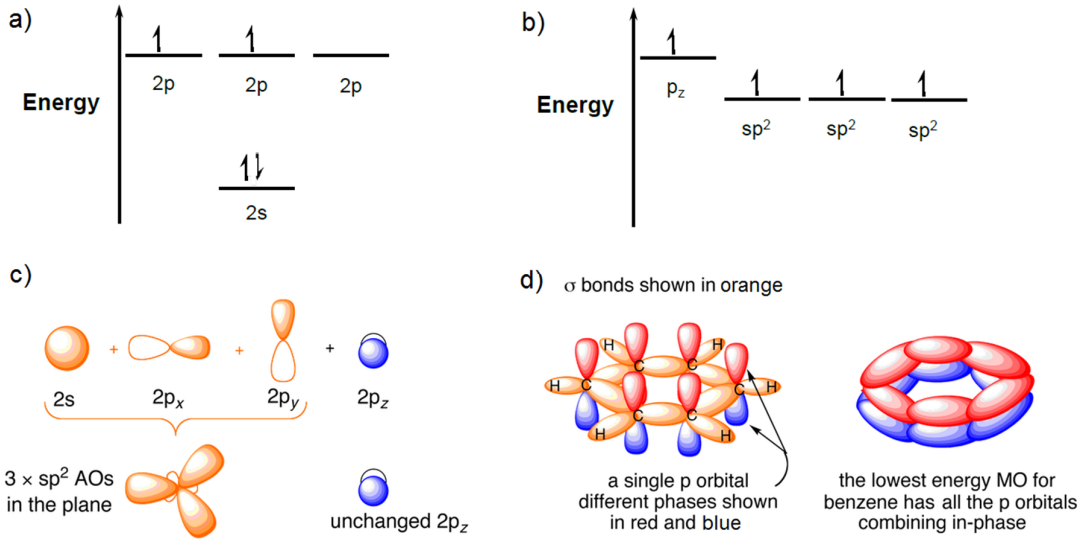


Figure 2.2: Electronic configuration of the outermost shell of a carbon atom (a) corresponding to its place in the periodic table and (b) in case of sp^2 hybridization; (c) sp^2 hybrid orbitals formation; (d) scheme of a benzene molecule formation.

2.1.3 Excitation and Deactivation Processes

An electron can have a spin quantum number of +1/2 or −1/2. In a conjugated organic system, the number or the π-electrons is mostly even. When all electrons are paired the total spin is $S = 0$. In case of a system with two unpaired electrons the spin is $S = 1$. A quantum angular momentum vector L associated with these electrons is allowed to have $2S + 1$ total values. Therefore, for the former case $L = 1$, i.e. only one state called singlet exists, whereas for the latter case $L = 3$ three triplet states occur. The singlet ground state is usually referred to as S_0 and the excited states – S_1, S_2, ..., accordingly. For each excited singlet state exists the corresponding triplet state (T_1, T_2, etc.) (Figure 2.3), whose energy is always lower due to enlarged distances between the electrons.

Processes governing basic optical phenomena (absorption, fluorescence, phosphorescence) in organic compounds are related to electronic transitions between the

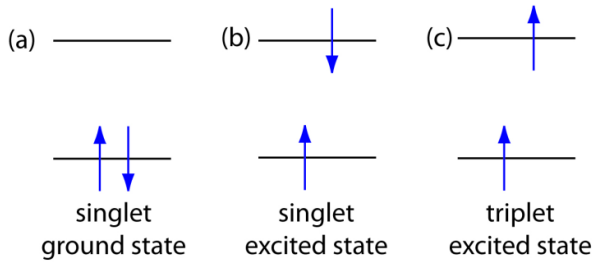


Figure 2.3: Electronic configurations of (a) a singlet ground, (b) an excited and (c) a triplet excited state.

three lowest electronic states: the ground singlet S_0, the first excited singlet S_1, and the first triplet T_1 states (Figure 2.4a). The key role of these states is based on ultrafast development of two kinds of non-radiative transitions after the molecule excitation: internal conversion (IC, no spin change) and intersystem crossing (ISC, spin changes).

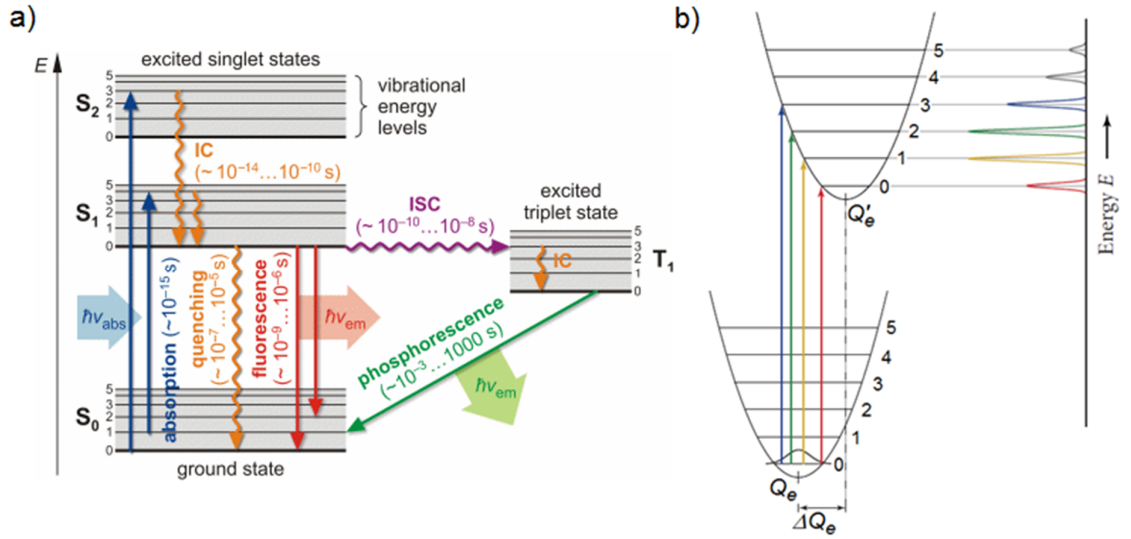


Figure 2.4: (a) Scheme of deexcitation processes (also known as the Jablonski diagram); waved lines mark non-radiative transitions; IC means internal conversion, ISC - intersystem crossing. (b) Configuration coordinate diagram of two electronic states illustrating formation of optical absorption band. Multiple transitions are possible in the absorption process (arrows shown) and the emission process (arrows not shown). The image (b) is taken from [100].

Since each electronic state has a subset of vibrational states corresponding to different vibration energy values in a given electronic state, absorption and emission spectra show structured or broad bands depending on the degree of disorder of the system called a vibronic progression. For a majority of conjugated molecules, the vibronic progression originates from a symmetric vinyl stretching mode with energy ~1400 cm^{-1} which corresponds to the nuclei reorganization energy ω_0 of ~0.17 eV. Figure 2.4b depicts potential curves and vibrational levels of the ground state S_0 and the first singlet state S_1. According to the Franck-Condon principle [99], the transition between S_0 and S_1 is considered to be vertical because the nuclei respond to the change of electronic structure on a much longer timescale than the electronic transition itself. The offset in nuclear coordinates ΔQ_e between the ground (Q_e) and excited state (Q'_e) shows a new equilibrium position for nuclear interaction potential.

Internal conversion brings the excited electron into the lowest vibrational state. Thus, the absorption and emission bands of a single molecule are mirror-symmetric (Figure 2.5). The difference in energy between their maxima is called Stokes shift. The intensities of the vibronic progression peaks of the spectra can be generally described by the Poisson distribution [100]:

$$I_n = e^{-S} S^n / n!, \tag{2.2}$$

where I is the intensity of the subband n, S is the Huang-Rhys parameter (a function of the ΔQ_e related to the coupling between electronic excitations and internal vibrations).

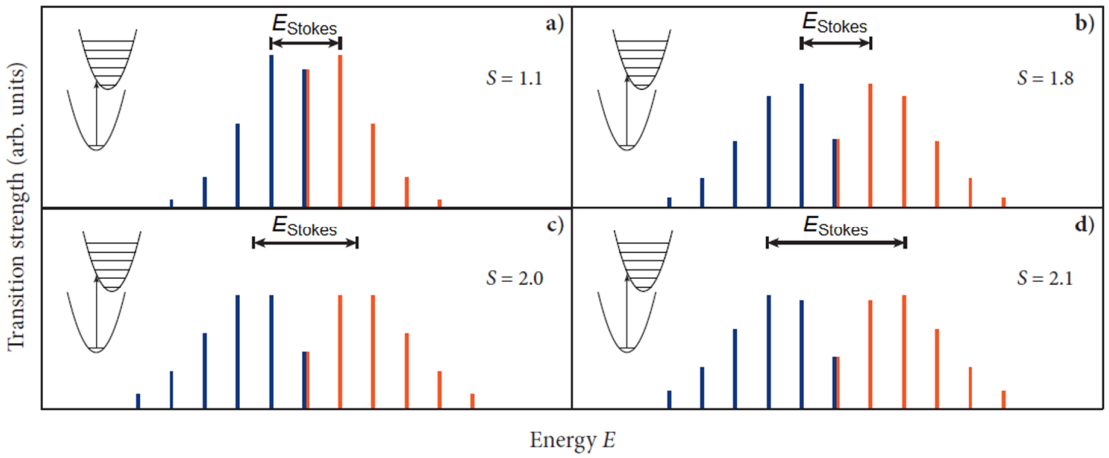


Figure 2.5: Calculated emission (blue) and absorption (orange) spectra for four different Huang-Rhys parameters S (a – d). The Stokes shift E_{Stokes} changes abruptly with increasing S. The image is taken from [100]

2.2 Noncovalent Intermolecular Interactions

Molecular packing plays a significant role in the determination of the physical properties in organic materials in the condensed state [101]. Here, thin film preparation methods and conditions (whether it is a vacuum-deposited or solution-processed film) are left out of the discussion. The section focuses only on weak non-covalent forces, whose balanced combination stabilizes the molecules kept together. Generally, all these forces are distance-dependent and are used to be called van der Waals forces (however, some texts exclude repulsion). The dominant interactions include exchange repulsion, induction, electrostatics and dispersion forces (Figure 2.6). The first term is a short-range destabilizing force following from the Pauli exclusion principle, which forbids two fermions to occupy the same quantum state. The exchange repulsion is the main reason for steric repulsion.

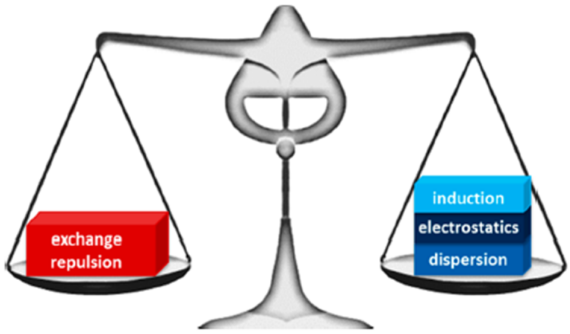


Figure 2.6: The repulsive exchange energy is balanced by the attractive dispersion, electrostatic, and induction components. The image is taken from [101].

Repulsion can be overcome by dispersion, electrostatic and induction non-covalent interactions. Dispersion forces, also known as London forces, arise between electrostatically neutral molecules (atoms). Though non-polar molecules do not have a permanent multipole moment, they do reveal spontaneous dipoles due to fluctuations in the electron density, which can in turn polarize a neighbor molecule. Attraction between a spontaneous dipole and an induced dipole follows an r^{-6} distance dependence [102]. Polar molecules with permanent dipoles (multipoles) interact through the electrostatic dipole-dipole attraction or repulsion. Induction or polarization is the attractive interaction between a permanent multipole of one molecule with an induced multipole of the second one.

When considering aromatic π-conjugated molecular packing, the term "π-π-interaction" in context of driving and stabilizing forces comes up. The scientific community has been struggling to give a clear definition of such interaction [101,103–107]. Basically, electrostatic and exchange repulsion are considered to counteract the attractive dispersion interaction between π-conjugated systems. Therefore, the interaction is stronger for larger aromatic molecules (containing more than 10 carbon atoms) [105]. Parallel slip-stacking and face-to-edge ("T-shaped") configurations help to minimize repulsion and thus, are generally more favorable than face-centered sandwich stacking, unless the participants are an electron-rich (donor) and an electron-deficient (acceptor) molecules (Figure 2.7) [106].

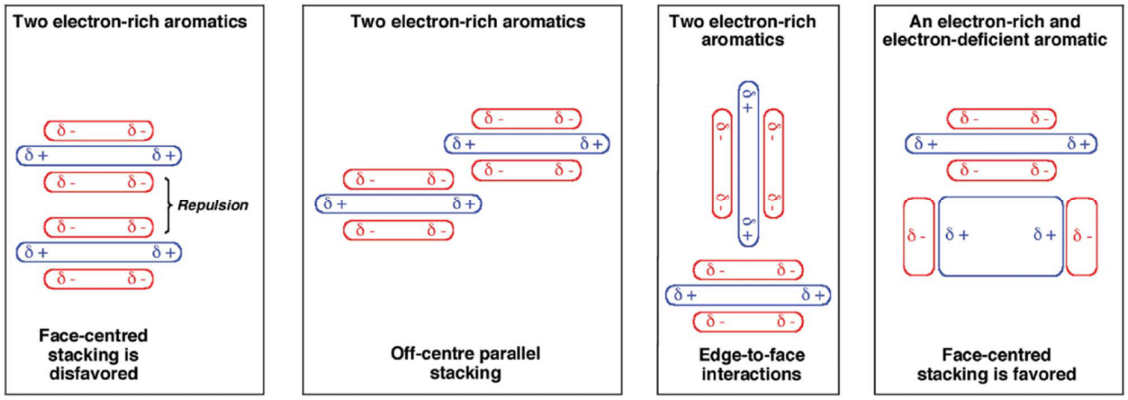


Figure 2.7: Schemes for describing the electrostatic view of aromatic interactions. The various modes of stacking are presented, emphasizing locations of electrostatic attraction or repulsion. The image is taken from [106].

The present thesis considers co-evaporated binary mixtures of small molecule OSCs. To describe the mixing behavior, a model based on nearest-neighbor interactions can be introduced [108]. Thus, the free energy of a mixture can be written as:

$$\Delta F_{mix} = k_B T[(x_A \ln x_A + x_B \ln x_B) + \chi x_A x_B], \tag{2.3}$$

where x_A and x_B are the concentrations of A and B components. The first term in the brackets is related to entropy and the second term depends on the interparticle interaction described by the parameter χ:

$$\chi = \frac{1}{k_B T}(W_{AA} + W_{BB} - 2W_{AB}), \tag{2.4}$$

where W_{AA}, W_{BB} and W_{AB} are the interaction energies between molecules A and B.

The typical mixing behaviors observed in binary thin films are sketched in Figure 2.8. In the case of all energies W being similar, there is no preferred phase in a system, which leads to formation of so-called solid solution or statistically intermixed molecules. When any of the W terms prevail, the corresponding phase tends to separate (whether it is a pure phase A or B or a mixed phase AB).

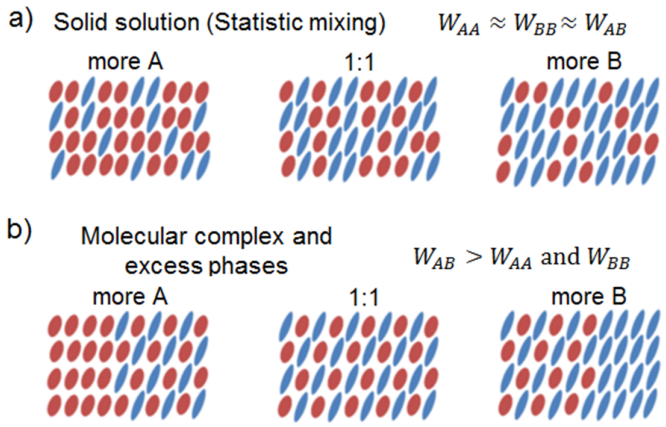


Figure 2.8: Typical mixing scenarios for binary mixtures of rod-like molecules depending on interaction energies W: (a) solid solution or statistical mixing; (b) phase separation between the mixed phase and the pure phase of an excessive component.

2.3 Intermolecular Coupling in Organic Assemblies

2.3.1 Kasha's Model

In the framework of the thesis, it is useful to reveal some general correlations between packing and optical properties taking place in molecular aggregates. Optical properties of organic materials are strongly influenced by the molecular environment. The resulting spectroscopic signatures of thin films usually deviate significantly from the monomer spectra of dissolved compounds due to intermolecular interactions [109–112]. Two mechanisms for such interactions may be considered (Figure 2.9): 1) non-resonant interactions causing a solution shift or a gas-to-crystal shift of energy levels, in case of liquid or solid systems, respectively, due to changes of the polarizability of the molecular environment; 2) the excited state resonance dipole-dipole interaction (long-range Coulomb coupling) described for two ideal cases of the so-called J- and H-aggregations by Kasha [113], where different arrangements of strongly coupled, parallel translated transition dipole moments (TDMs) μ are responsible for either a blue-shifted or red-shifted absorption due to exciton state splitting. The blue shift originates from electrostatic repulsion of the TDMs aligned in-phase in a face-to-face arrangement, whereas for an in-line arrangement the in-phase alignment leads to a lowering of the exciton state energy.

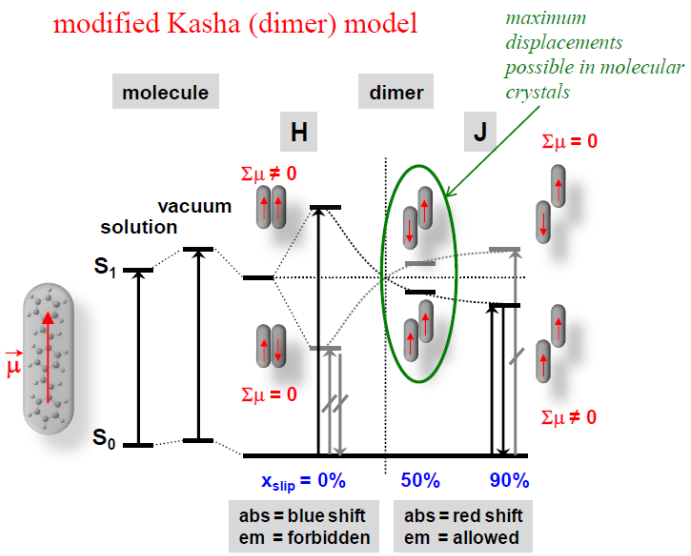


Figure 2.9: H- and J-aggregates and their impact on the absorption and emission processes in the framework of exciton models. The image is taken from [85].

In case of an oblique orientation of the TDMs, both components composed by summation and subtraction of the TDMs can be observed (Figure 2.10). This effect is anisotropic [114] and known as Davydov splitting (DS). A magnitude of the splitting DS can be defined as follows [113]:

$$\mathrm{DS} = \frac{2|\mu|^2}{r_{12}^3}(\cos\alpha + 3cos^2\theta), \tag{2.5}$$

where μ is the TDM of a monomer, r_{12} is the center-to-center distance between molecules 1 and 2, α is the angle between polarization axes for the component absorbing units and θ

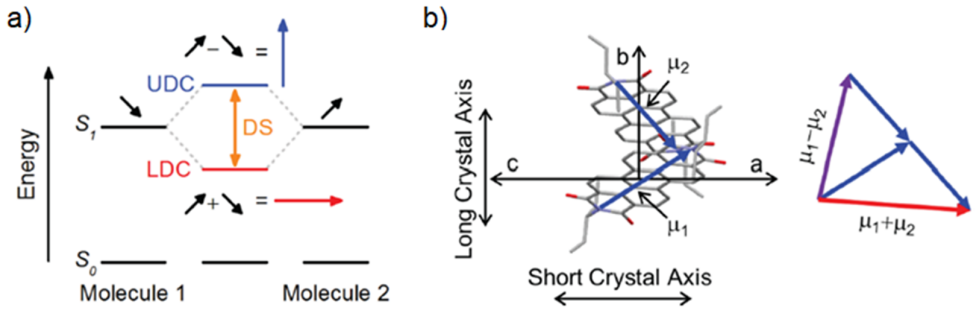


Figure 2.10: (a) Energy level diagram for a molecular dimer. When the TDMs (shown as black arrows) are not parallel, both the upper and lower states absorb light at orthogonal polarizations, giving rise to the upper (UDC) and lower (LDC) Davydov components observed spectroscopically. (b) Left: Crystal structure of nearest-neighbor π-stacked molecules. The *b* axis corresponds to the crystal's long axis, while the *a* and *c* axes project onto the crystal's short axis. The projections of the TDMs are shown as blue arrows. Right: The sum and difference of the TDMs. The sum, which corresponds to the LDC, is nearly parallel to the short crystal axis, while the difference, which corresponds to the UDC, is nearly parallel to the long crystal axis. Both the sum and difference have nearly equal lengths, indicating similar oscillator strengths for the UDC and LDC. The images are taken from [87] and modified.

is the angle between the polarization axes of the unit molecule and the line of molecular centers.

An energy shift caused by the exciton coupling interferes with a gas-to-solution or gas-to-crystal shift, which might make it difficult to distinguish the type and strength of the coupling. Therefore, one should also rely on bandshape changes due to the exciton-vibrational coupling described in the extension of Kasha's theory [115–117]. Accordingly, an increase (decrease) of the oscillator strength of the 0-0 vibronic band compared to the 0-1 vibronic band along with appearance of a low (high)-energy transition are strong signatures of enhanced J(H)-like coupling (Figure 2.11).

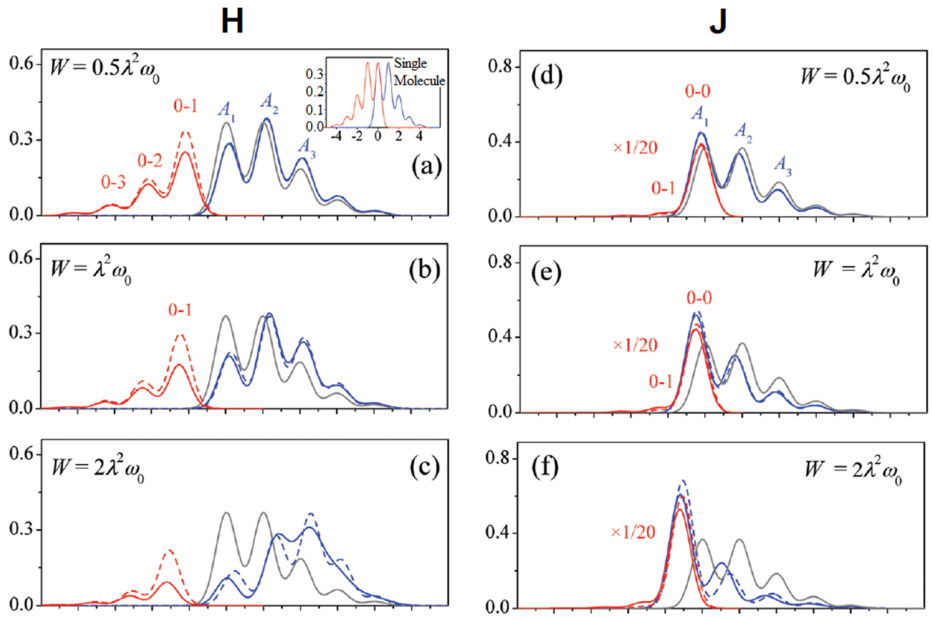


Figure 2.11: Calculated absorption (blue) and emission (red) spectra for linear H- and J-aggregates containing $N = 20$ molecules with nearest-neighbor-only coupling. Here, the exciton bandwidth W increases from top to bottom, λ^2 is the Huang-Rhys factor and ω_0 is the energy of the symmetric intramolecular vibration. Solid spectra are evaluated using one- and two-particle states, while dashed spectra use only one-particle states. The inset in panel (a) shows the isolated-molecule spectra. The grey absorption spectrum appearing in all panels pertains to the isolated molecule ($W = 0$). The images is taken from [90] and modified.

2.3.2 Charge Transfer

Two molecules with electron-donating (donor) and electron-withdrawing (acceptor) properties relative to each other can form a so-called CT complex. A donor (D) is a molecule, whose ionization energy and electron affinity is smaller than the one of an acceptor (A). The theory of donor-acceptor bonding was developed by Robert S. Mulliken in 1952 [43,44]. According to his theory, a DA-bonding occurs in a D/A system on account of quantum-mechanical mixing of two states:

- neutral or no-bond structure (D, A), in which between the D and A molecules only van der Waals interactions take place;

- polar or dative structure (D^+ - A^-), in which an electron is fully transferred from the donor to the acceptor.

In the ground electronic state, the wave function of the CT complex can be written as a linear combination of the no-bond and dative structures:

$$\psi_N = a\psi_0(D,A) + b\psi_1(D^+ - A^-), \tag{2.6}$$

and in the excited state:

$$\psi_E = a^*\psi_1(D^+ - A^-) - b^*\psi_0(D,A). \tag{2.7}$$

The coefficient $a \approx a^*$ and $b \approx b^*$ in (2.6) and (2.7) characterize a contribution of the no-bond and dative structures to the ground and excited electronic states of the CT complex. They relate as $a^{(*)2} + b^{(*)2} + 2a^{(*)}b^{(*)}S_{01} = 1$, where $S_{01} = \int\psi_0\psi_1 d\tau$ is an overlap integral between donor and acceptor molecular orbitals participating in CT (τ is time). $a^2 >> b^2$ is relevant for weak CT complexes and $b^2 > a^2$ for strong ones. It follows that if the ground state has predominantly a no-bond structure, the excited state must have predominantly a dative structure and vice versa. A mixed state, in fact, describes a dipole $D^{+\delta}A^{-\delta}$, where δ is a degree of a transferred charge.

Photogeneration of charge carriers in OSCs occurs via a Coulombically bound electron-hole pair called a CT exciton. In contrast to Frenkel excitons (FE), where both charges are localized on the same molecule, an excited electron in the case of a CT exciton is transferred to a neighbor molecule (Figure 2.12a), though mixing of FE and CT states is possible [118]. A larger coupling between D and A, i.e. a larger overlap between the HOMO of a donor and LUMO of an acceptor, enables direct electronic transitions between the ground electronic state and CT states of a D-A pair (Figure 2.12b) [119].

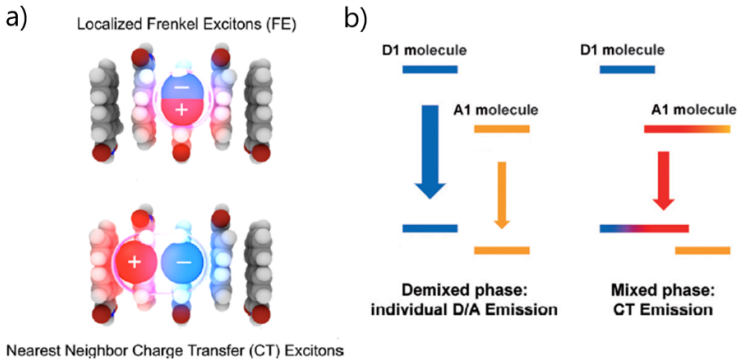


Figure 2.12. (a) Graphical illustration of Frenkel excitons and charge transfer excitons; (b) frontier molecular orbital diagrams of mixed and demixed phases. The images are taken from [92] and [93], and modified.

An energy diagram of CT states and principal steps of photogeneration is schematically presented in Figure 2.13 [120]. Excitation of an electron can occur either via formation of a singlet exciton on a donor (green solid arrow) followed by non-radiative relaxation through a so-called "hot" CT states down to the lowest CT state CT_1 (red arrow) or via a direct transition to the CT_1 from the ground state GS (blue arrow). The energy of relaxed

CT states (E_{CT1}) is smaller than the energy gap between $HOMO_D$ and $LUMO_A$ (E_{DA}) due to Coulomb bonding energy of the hole-electron pair, which has to be overcome to separate the charges (CS – charge separation states).

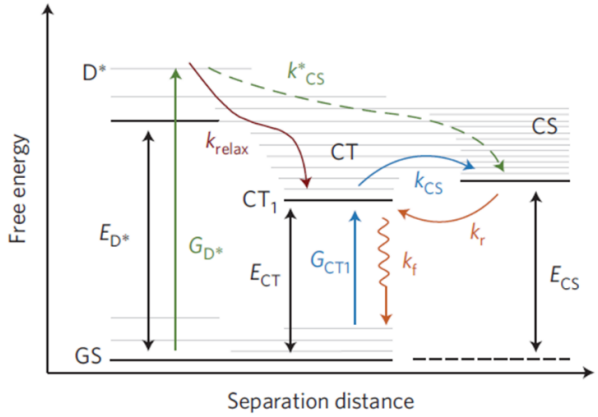


Figure 2.13. Energetics of the relevant states at a *D*/*A* interface. Absorption of a photon with energy higher than E_{D^*} generates the donor excited state *D** at a rate G_{D^*}. There are several possible pathways for the generation of a CS state. Pathways with rate constants k^*_{CS} bypass the vibrationally relaxed and lowest energy CT state (CT_1) and compete with thermal relaxation (k_{relax}). CT_1 can decay radiatively (k_f) to the GS or dissociate (k_{CS}), forming CS. The inverse of the latter process, population of CT_1 from CS, occurs at a rate k_r. The images are taken from [94] and modified.

CHAPTER 3

EXPERIMENTAL METHODS

3.1 Sample Preparation by Organic Molecular Beam Deposition (OMBD)

All thin films were prepared by organic molecular beam deposition (OMBD) [121,122] in ultra-high vacuum (UHV) chambers. UHV chambers of two types were used: a stationary chamber with a base pressure of 1×10^{-9} mbar for in-house sample production and a portable chamber with a base pressure of 1×10^{-8} mbar for real-time experiments at synchrotron facilities [123].

The principle of a UHV system is shown in Figure 3.1a. An organic powder-like material is placed inside an effusion (Knudsen) cell. The material sublimes in the cell upon heating and, when the cell shutter is open, the molecules leave the cell forming a flux towards a sample holder. The flux rate can be controlled by the cell temperature. Co-deposition is possible when more than one cell is used. Main processes happening on a substrate during deposition are sketched in Figure 3.1b. They include condensation, re-evaporation or desorption, intra- and interlayer (surface) diffusion, and nucleation. Molecule diffusion, limited by its kinetic energy and a step-edge potential barrier also known as Ehrlich–Schwöbel barrier [124,125] can be controlled by a change of the substrate temperature T_{sub}. Growth by vacuum deposition generally follows one of three regimes: layer-by-layer (Frank-van-der-Merwe) mode, island (Vollmer-Weber) mode, and combined layer-plus-island (Stranski-Krastanov) mode.

In this thesis, three types of substrate were used: silicon wafers with a native oxide layer on top ($d_{ox} \approx 2$ nm), silicon wafers with thermal oxide ($d_{ox} \approx 130$ nm) and glass cut to a size of 10×5 mm. Before introduction in the vacuum chamber, the substrates were cleaned

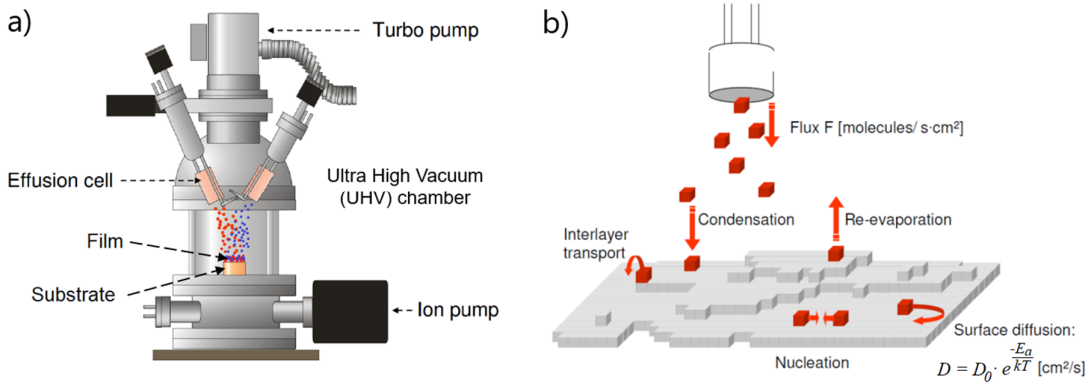


Figure 3.1. (a) Schematic illustration of a portable UHV chamber and a process of co-deposition. (b) Sketch of principal processes occurring during vacuum film deposition. The images are taken from [97] and modified.

in an ultrasonic bath with acetone and isopropanol successively. Prior to growth, the substrates were heated to 650 K in vacuum in order to eliminate residuals of water and other impurities. The deposition rates (0.2 nm/min) during growth were controlled by a water-cooled quartz crystal microbalance (QCM) calibrated by X-ray reflectivity (XRR). The majority of samples were prepared by co-evaporation of two types of materials, a donor and an acceptor, with different mixing ratios. For DIP:PDIR-CN_2 system three different architectures were chosen (Figure 3.2) [2]: a planar heterojunction (PHJ) as the simplest model, a two-component mixed bulk-heterojunction film (BHJ) with different mixing ratios and a superlattice (SL) consisting of 20 alternating monolayers (MLs) as an intermediate case. Samples characterized by XRD, AFM, and spectroscopical measurements are listed in Table 3.1.

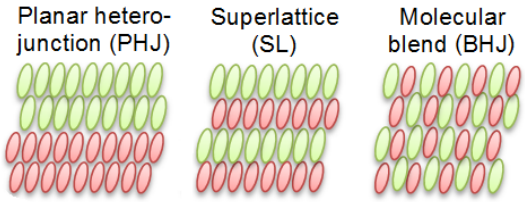


Figure 3.2. Sketch of the structural geometries (red ellipsoids – donor, green ellipsoids – acceptor).

Table 3.1. List of the investigated samples.

Component	Configuration	T_{sub}, °C	d, nm
DIP	single layer	RT	20; 100
		140	20
PEN	single layer	RT	20; 100
		70	20; 100
PDIR-CN_2	single layer	RT	20; 100
		70	20
		120	20
		130	20
		140	20
PDIF-CN_2	single layer	RT	20; 100
		70	20
		110	20
		120	20
		140	20
		160	20
DIP:PDIR-CN_2	3:1	RT	20
		140	20

	2:1	RT	100
	1:1	RT	20; 100
		140	20
	1:3	RT	20; 100
		140	20
	1:9	RT	20; 100
	bilayer DIP/PDIR-CN_2	RT	20 (each layer)
	superlattice (DIP/PDIR-CN_2)$_{10}$	RT	1.8 (each layer)
DIP:PDIF-CN_2	3:1	RT	20
		140	20
	1:1	RT	20
		140	20
	1:3	RT	20
		140	20
PEN:PDIR-CN_2	3:1	RT	20
		70	20
	1:1	RT	20; 100
		70	20; 100
	1:3	RT	20
		70	20
PEN:PDIF-CN_2	3:1	RT	20
		70	20
	1:1	RT	20; 100
		70	20; 100
	1:3	RT	20
		70	20

3.2 X-Ray Diffraction Techniques

X-Ray diffraction (XRD) methods provide uncountable opportunities for the determination of material structural properties at molecular and atomic levels. In this thesis, the following techniques were used to investigate ordering and mixing behaviors in the studied *D/A* systems: X-Ray reflectivity (XRR), grazing-incidence X-Ray diffraction (GIXD), and reciprocal space maps (mesh scans). The measurements were performed postgrowth and ex situ after sample preparation combined in particular cases with real-time in situ experiments. X-ray diffraction measurements were performed at the beamline ID10 of the European Synchrotron Radiation Facility (Grenoble, France) (Figure 3.3), at

the beamline X04SA of the Swiss Lightsource (Villigen, Switzerland), and at the beamline SixS of the Soleil Synchrotron (Paris, France) using a focused beam with a wavelength of λ = 0.9398 Å and λ = 0.8857 Å, respectively. The raw data were processed and corrected for footprint and background contributions. More details on the topic can be found in references [126–128].

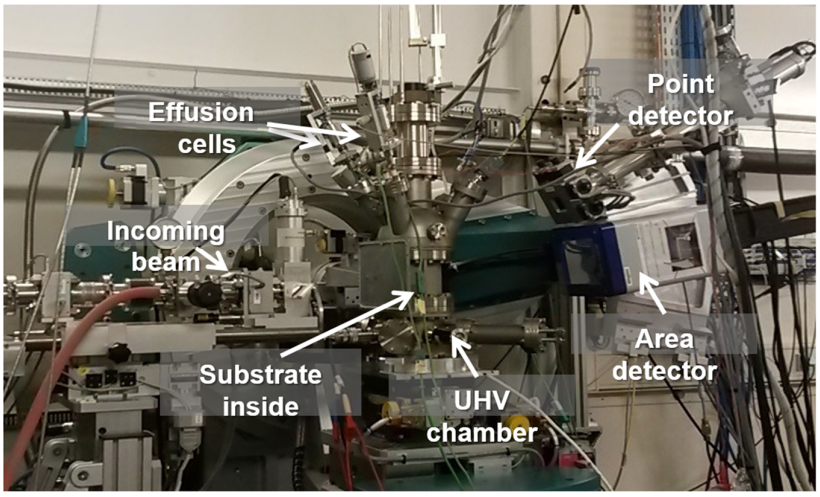


Figure 3.3. Photograph of a portable UHV chamber mounted on a diffractometer for real-time experiments at beamline ID10b, ESRF.

XRR is a precise method for the investigation of surfaces and interfaces in multilayered systems. It is applied to determine the electron density profile in the out-of-plane direction (i.e. along the surface normal), the thickness, and roughness of the layers. Figure 3.4a demonstrates the scattering geometry of an XRR scan. The incoming and outcoming beams with the wave vectors k_{in} and k_{out} satisfy the specular condition, i.e. are oriented at the same angle θ to the sample surface. They move simultaneously during a scan in one plane. The scattering vector q resulting from the difference between these two wave vectors k is oriented along the surface normal (Z-axis) and can be written as:

$$q_z = \frac{4\pi}{\lambda}\sin(2\theta), \tag{3.1}$$

where λ is the wavelength. Using the q_z of a reflection, the lattice spacing d can be derived:

$$d = \frac{2\pi}{q_z}, \tag{3.2}$$

Information about an organic layer can be evaluated from an XRR scan since it contains peculiar features (Figure 3.4b). Kiessig oscillations or fringes in the low q_z-range originate from interference of beams both reflected from the top and the bottom interfaces of the film. Hence, the film thickness and roughness can be extracted from periodicity and damping of the oscillations. If the film is ordered in the out-of-plane direction, interference between the lattice planes gives rise to Bragg peaks. The lattice constant can be determined from the position of the main maximum, while a periodicity of the Laue oscillations on both

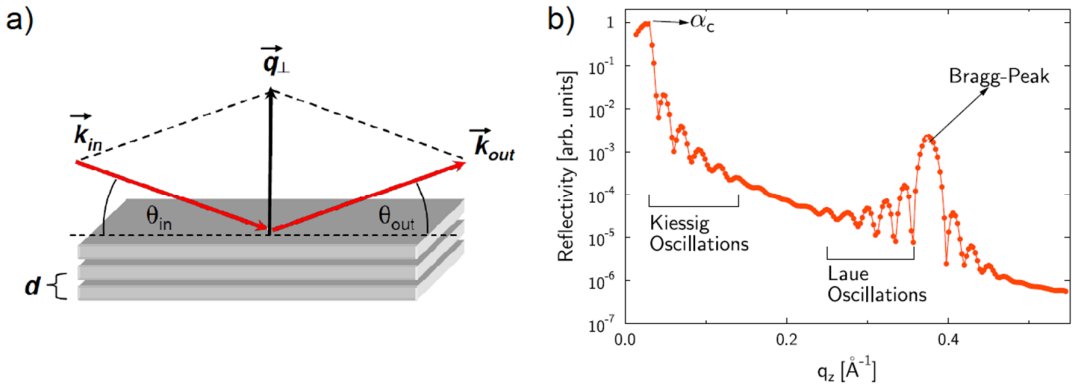


Figure 3.4. (a) Scattering geometry of an XRR measurement. (b) Simulated data of an XRR measurement of 15 completely filled and seven dilute layers of DIP on native SiO_x. The image is taken from [101] and modified.

sides gives a thickness of a crystallite formed by contributing layers. The critical angle α_c (total reflection edge) depends on the electron density of the substrate.

In this thesis, XRR data fitting was done with GenX [129] based on the Parratt formalism [130]. The corresponding scattering length density (SLD) (similar to the electron density) profile along Z-axis can be modelled, when the chemical composition is known.

In order to explore the in-plane crystal structure, GIXD is applied. The scattering geometry is shown in Figure 3.5. The incidence beam is fixed at an angle below α_c, this ensures an evanescent wave penetrating the surface, while the detector is scanning the 2Φ in-plane angular range. Thus, the resulting q-vector is almost parallel to the surface and can be associated with q_{xy}:

$$q_{xy} = \frac{4\pi}{\lambda} \sin\left(\frac{2\theta}{2}\right). \tag{3.3}$$

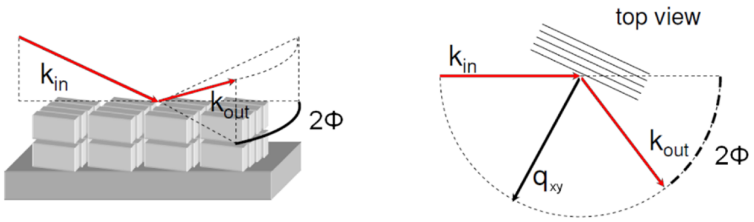


Figure 3.5. Scattering geometry of a GIXD experiment, which can be used to probe the in-plane crystal structure. The image is taken from [101].

Generally, organic crystalline thin films reveal a polycrystalline character in the in-plane (in contrast to single crystals) and a long-range order in the out-of-plane directions, therefore, they can be considered as a so called "two dimensional (2D) powder". This allows GIXD to probe in-plane lattice spacings of differently oriented crystalline domains. From the width of in-plane Bragg reflections, the calculation of the coherently scattering crystallite size l_s according to the Scherrer formula [131] is possible:

$$l_s = 2\pi K/\mathrm{FWHM}, \tag{3.4}$$

where K is Scherrer's constant close to unity and FWHM is the full width at half-maximum of a peak.

Many synchrotron beamlines provide a 2D detector (for this thesis a PILATUS 300k at the ESRF and 100k at the SLS were used), which allows to collect a scattered signal with $q_z \neq 0$. The method consists in taking a mesh scan for collecting multiple images within a q-range of interest. All images taken in this thesis were evaluated and assembled together using MATLAB. The resulting reciprocal space maps provide information about the crystal unit cell and quality of the crystal order. In Figure 3.6, three cases for polycrystalline samples with different degree of crystallite misalignment along q_z are demonstrated.

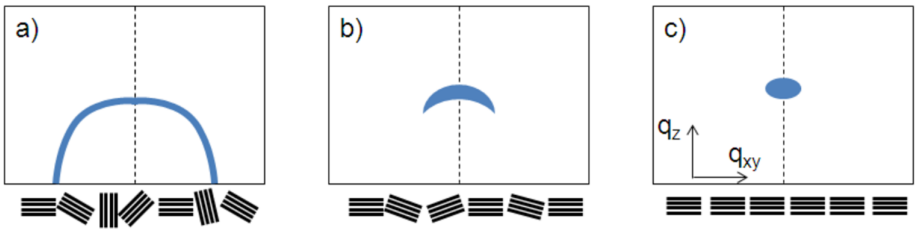


Figure 3.6. Schematic of diffraction patterns from a polycrystalline sample with (a) randomly oriented crystalline domains, (b) slightly misoriented crystalline domains along the q_z-direction, (c) highly oriented crystalline domains along the q_z-direction. The image is taken from [102].

3.3 Optical Spectroscopy

The main focus of this thesis is the observation of optical signatures of intermolecular coupling in general and a CT in particular. For these purposes, three main spectroscopic techniques were applied:

1) *Variable angle spetroscopic ellipsometry (VASE)* for the optical constants determination;
2) *Temperature-dependent photoluminescence (PL)* for studying radiative recombination pathways;
3) *Differential reflectance spectroscopy (DRS)* for real-time monitoring of changes in optical absorption spectra during the film growth.

3.3.1 Variable Angle Spetroscopic Ellipsometry (VASE)

Taking into account optical anisotropy in materials which exhibit crystalline order, it is very useful to consider optical features decoupled along different crystalline directions [1,114]. For this purpose, variable angle spectroscopic ellipsometery (VASE), which allows to probe optical anisotropy in thin films [132,133], was applied. The measurements were performed with a Woollam M2000 ellipsometer in an energy range of 0.7 – 5 eV in reflection mode. A schematic of the setup is shown in Figure 3.7. The spectrometer is controlled by the WVASE32 software from Woollam, which was also used to analyze the data [134]. The

ellipsometer is installed on a Woollam goniometer with a possibility to vary the angle of incidence (AOI) from 40° – 90° relative to the surface normal, thus, providing an additional angle dependent information about the ellipsometric angles Ψ and Δ. The rotating compensator periodically changes the polarization state of the incoming light beam. When interacting with the sample, the polarization state of the reflected beam changes with respect to the incoming beam in accordance to the optical properties of the investigated material.

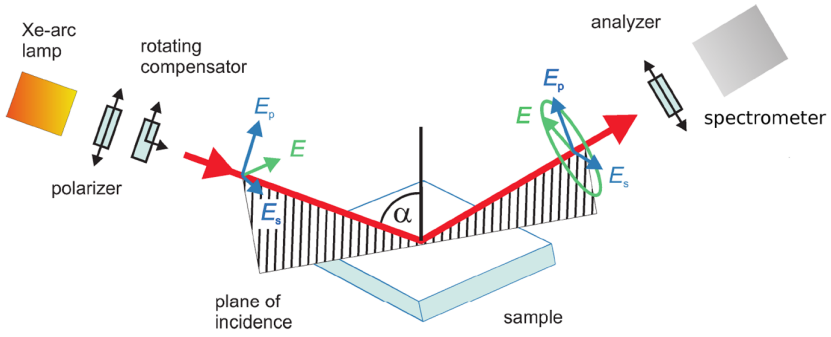


Figure 3.7. Schematic of an ellipsometric measurement. Light with a polarization state periodically changed by the rotating compensator is reflected by the sample. The new polarization state is measured by an analyzer and a spectrometer. The images is taken from [107].

The optical constants of uniaxial anisotropic thin films can be evaluated from the Ψ and Δ spectra. For this purpose, a multisample analysis is required. Therefore, two (or three) kinds of substrates, e.g. silicon with native oxide, silicon with thermal oxide or glass with a roughened backside, were used. Assuming the same optical properties on all substrates, coupled layers representing the film were applied to the model and the data sets were fitted simultaneously. Additional layers in the model describe a Si bulk substrate and a SiO_x layer (or a SiO_x bulk for glass). The coupled layer consists of two sublayers describing the in-plane and the out-of-plane components of the dielectric function. In case of a rough sample, roughness can be modelled by an 'effective medium approximation' (EMA) layer according to the Bruggeman model [135].

The fitting algorithm can be based on two approaches: the 'point-by-point fit' and the 'normal fit'. When using a 'point-by-point fit' the optical constants are getting optimized in comparison with the experimental data for all points of the energy range and angles of incidence independently. The result in this case is not necessarily Kramer-Kronig-consistent [136,137]. When performing a 'normal fit', the optical constants are modelled by sum of Gaussian oscillators representing the optical transitions in agreement with the Kramer-Kronig relation. In this case, the resulting spectra are sensitive to the given starting parameters.

3.3.2 Temperature-Dependent Photoluminescence (PL)

In photoluminescence (PL) spectroscopy, the emission of a thin film upon laser excitation is measured. It is a highly sensitive technique to probe intermolecular interactions stemming from the arrangement in solid-state organic films [1,138,139] (see Section 2.3).

PL spectra were measured with a Labram HR 800 spectrometer (Horiba Jobin Yvon, France) with a nitrogen cooled charge-coupled device (CCD) 1024×256-OPEN-3S9 detector and a monochromatic frequency-doubled Nd:YAG laser (532 nm wavelength / 2.33 eV) or a He-Ne laser (633 nm / 1.96 eV). For temperature-dependent measurements, a Linkam sample stage was used. This allows to cool down a sample using liquid N_2 to ~77 K in a protective dry N_2 atmosphere.

The optical path of the spectrometer is illustrated in Figure 3.8. A laser beam can be attenuated by the density filter. A video-camera, which allows to use the spectrometer as a microscope, is coupled to the optical path through a beam splitter between lens 2 and the objective. A changeable grating (150 or 1800 lines) defines spatial and spectral resolution of the diffracted light on a CCD detector.

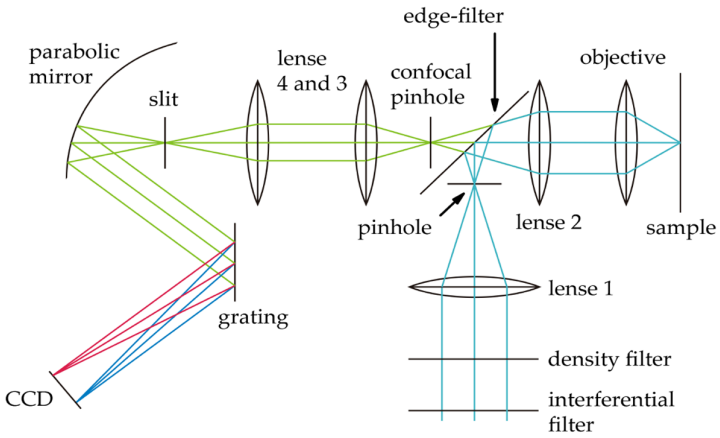


Figure 3.8. Optical path of the confocal spectrometer. The beam (blue) enters the system and is focused through the pinhole. It is reflected by the edgefilter and excites the molecules of the sample. The scattered light is returned to the edgefilter, lower-energetic light (green) passed and focused through the confocal pinhole. The light is sent by the parabolic mirror onto the grating and is there dispersed into its spectral components. A CCD captures the spectrum. The image is taken from [113].

3.3.3 Differential Reflectance Spectroscopy (DRS)

In order to correlate the optical features with the structural properties, differential reflectance spectroscopy was used, which allows monitoring the development of the in-plane component of the thin film absorption from the beginning of film formation with high time resolution [1,140–143].

The DRS setup consists of a fiber coupled USB2000+ spectrometer, working in an energy range between 1.4 – 3 eV, and a DH-2000 lamp (Ocean Optics, U.S.A.) (Figure 3.9). The optical fiber together with a focusing lens is mounted on a UV-Vis transparent window of the OMBD chamber at a position ensuring normal incidence of the light. The beam is reflected by the sample and goes back through the splitted fiber to a detector. A film growing on the substrate changes the reflected signal and the difference can be converted to a DRS signal in the following way [144]:

$$DRS = \frac{R(d)-R_0}{R_0}, \tag{3.5}$$

where R_0 is the intensity of a signal reflected by the bare substrate which is changing to $R(d)$ while a film of thickness d is growing on the substrate. Thus, the DRS signal is independent of the incoming intensity. However, the signal is extremly sensitive to any fluctuations in the surrounding light or thermal drifts of the substrate. The best compromise between the time resolution and signal-to-noise ratio is ensured by averaging 4000 – 6000 scans every two minutes. Figure 3.10 provides an example of such a measurement.

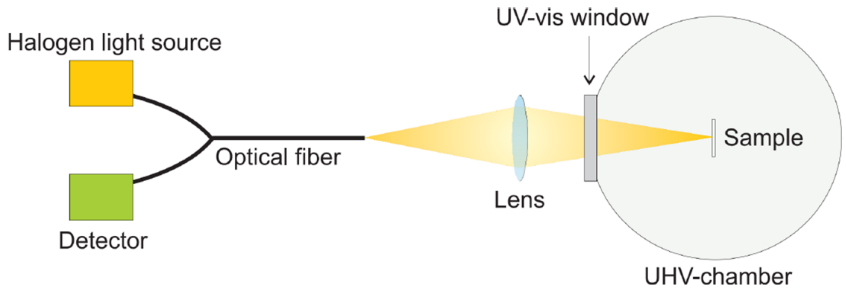


Figure 3.9. Schematic of a DRS setup: the light passing through the optical fiber from the halogen lamp to the chamber is reflected from the sample and delivered through the fiber to the detector. The images is taken from [114].

Using the DRS signal, the in-plane component of the film dielectric function $\varepsilon_{2,xy}$ can be evaluated when the real-part of the dielectric function of a transperent substrate $\varepsilon_{1,sub}$ is known (in this thesis, glass wafers with roughened backside in order to avoid doubled reflection were chosen) [145]:

$$DRS\ (E) = \frac{8\pi Ed}{hc(1-\varepsilon_1(E)_{sub})}\varepsilon_2(E), \tag{3.6}$$

Note, the approximation is only valid in case of very thin films when $d << \lambda$.

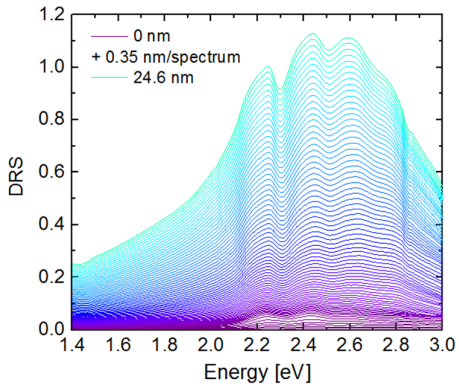


Figure 3.10. Exemplary DRS measurement of a DIP film during growth.

3.4 Further Methods

The details for this section are based on Ref. [2].

3.4.1 Morphology and IR/NIR/Vis/UV Spectroscopy

The surface morphology was measured by atomic force microscopy (AFM) using a JPK Nanowizard II instrument in tapping mode under ambient conditions. Image analysis was performed with Gwyddion [146]. Absorption and fluorescence spectra in $ClCH_3$ solution were recorded with a Varian Cary ultraviolet/visible range (UV/Vis) spectrophotometer (Varian, The Netherlands). Infrared (IR) spectra were obtained in transmission mode with a Vertex 70 (Bruker) Fourier-transform IR (FTIR) spectrometer at the Brewster's angle of silicon (74°). The theoretical IR spectra were calculated with TURBOMOLE software. UV/Vis/near-IR (NIR) absorption spectra were obtained using a Varian Cary 5000 spectro-photometer (Agilent Technologies) at normal incidence. The time-resolved PL studies were carried out with a Hamamatsu streak camera. The excitation wavelength was set to 460 nm, employing a lithium triborate crystal for second harmonic generation.

3.4.2 Ultraviolet Photoelectron Spectroscopy (UPS)

Thin films for ultraviolet photoelectron spectroscopy (UPS) measurements were grown under high vacuum conditions (base pressure below 10^{-8} mbar) onto (100)-oriented Si wafers with a native oxide layer and onto highly oriented pyrolytic graphite (HOPG) substrates by molecular beam deposition. Prior to the film deposition, the SiO_x substrates were cleaned in a ultrasonic bath with acetone, isopropanol, and deionized water for at least 15 min. Atomically smooth graphite surfaces were prepared via exfoliation of HOPG (Optigraph GmbH, ZYA quality, mosaic spread 0.4°±0.1°) in air. After careful outgassing, DIP and PDIR-CN_2 were evaporated at a constant molecular flux of ~10 Å/min, as monitored by a QCM. The nominal film thickness was determined by the QCM and further cross calibrated using subsequent AFM measurements.

The photoemission experiments were performed at the beamlines PM4 LowDosePES (end station SurICat) and UE52 (end station UE52-PGM Multicolor) at the synchrotron storage ring BESSY II at Helmholtz-Zentrum Berlin. Both end stations permit to transfer the samples between preparation (base pressure 10^{-8} mbar) and analysis chamber (base pressure 10^{-10} mbar), thus, enabling an in situ characterization. The photon excitation energies were 35 and 120 eV. Photoelectrons were detected using a Scienta SES 100 hemispherical electron spectrometer, consisting of a microchannel plate and a CCD camera. The energetic resolution of the chosen settings was 50 meV. Additional experiments used an in-house setup, equipped with a He discharge lamp (E_{EXC} = 21.2 eV) and a Scienta EA125 hemispherical analyzer.

3.4.3 Device Fabrication and Characterization

For the fabrication of the solar cells, commercially available glass substrates coated with pre-structured 140 nm indium tin oxide (ITO) (purchased from Thin Film Devices, Inc., CA; sheet resistance ≈ 20 Ω/square) were used. The substrates were cleaned with deionized water, acetone and isopropyl alcohol. Afterwards, a polymeric hole injection layer of HIL 1.3 (purchased from Heraeus Clevios GmbH, Germany) was spin-coated from an aqueous solution on ITO, resulting after annealing for 30 minutes on a hot plate at 125 °C under ambient conditions, in approximately 30 nm thickness. DIP and PDIR-CN_2 were evaporated onto the substrate by organic molecular beam deposition with the substrate at room temperature and at a base pressure lower than 2×10^{-6} mbar. As cathode material, 100 nm aluminum was thermally deposited through a shadow mask onto a previously applied 5 nm thick exciton blocking layer of bathocuproine (BCP). Each sample had four pixels with an active area of $A = 4$ mm^2.

The layer sequence for the planar heterojunction (PHJ) solar cell was: ITO / HIL 1.3 / DIP (50 nm) / PDIR-CN_2 (40 nm) / BCP / Al. To achieve the same nominal thickness of the active layer for the planar-mixed heterojunction (PM-HJ) solar cell, 20 nm DIP, 50 nm of a 1:1 mixture of DIP:PDIR-CN_2 by co-evaporation and 20 nm PDIR-CN_2 were subsequently deposited.

Current density-voltage (*j-V*) characteristics were recorded with a Keithley 236 source-measure unit and FLUKE 8845A precision multimeter. The currents were measured in the dark and under simulated one sun AM1.5G, 100mW/cm^2 illumination with a Xe-lamp. All measurements were performed in a glove box under nitrogen atmosphere and at room temperature.

Electroluminescence measurements were carried out by using a liquid-nitrogen cooled CCD camera (PyLoN:100BR eXcelon, Princeton Instruments) coupled with a spectrometer (SP2300i, Princeton Instruments) with a spectral sensitivity in the wavelength range of approximately 300-1000 nm. The measurements were performed under a dc voltage drive from a Keithley 2400 source meter.

Incident photon-to-current efficiency (IPCE) spectra were detected under monochromatic illumination (Omni-λ300 Monochromator/Spectrograph, Zolix Instruments Co., LTD.) equipped with a halogen lamp and a light-beam chopper. The setup was calibrated with a silicon photodiode. The short circuit current measurements according to the incident wavelength were carried out by using a lock-in amplifier (Stanford Research Systems SRS830 DSP).

Conductivity measurements were performed on blended films with different mixing ratios deposited on glass substrates with interdigitated ITO electrodes in the dark and under illumination with a halogen lamp using a Keithley 2612A source-meter unit.

3.4.4 Near-Edge X-ray Absorption Fine Structure (NEXAFS)

Utilizing the dichroism of X-ray absorption, NEXAFS spectroscopy allows the determination of the average molecular orientation in thin films, perfectly supplementing

the information gained from XRD. The exact intensity dependence for π^*-transitions for substrates of at least threefold-symmetry is given by Equation 3.7 [147].

All samples for the near-edge X-ray absorption fine structure (NEXAFS) measurements were deposited under high vacuum conditions (base pressure 10^{-7} mbar) and nominal growth rates of 4 nm/min for DIP and 3 nm/min for PDIR-CN_2. The NEXAFS measurements were performed at the beamline D1011 of the synchrotron storage ring MAX II at MAX IV laboratory, Lund University, Sweden. The used light is linearly polarized. Through the end station an energy resolution of about 50 meV around the carbon K-edge is achieved. All NEXAFS spectra were recorded in total electron yield mode. Contributions from the substrate, which overlap with the sample signature, were subtracted to isolate the unadulterated thin film spectra. The observed dichroisms were analysed using Equation (3.7), to obtain the average molecular orientation [147,148]:

$$I_{\pi^*}(\theta,\alpha) \propto P \cdot \cos^2(\theta) \cdot \left(\frac{3}{2}\cos^2(\alpha) - \frac{1}{2}\right) + \frac{1}{2}\sin^2(\alpha), \tag{3.7}$$

Here, θ is the angle of incidence between the incoming X-ray photons and the sample surface plane, α is the average molecular inclination angle between molecular plane and substrate surface and $P = 0.975$ is the degree of polarization, characteristic for the beamline. Additionally, an angular offset θ_{offset} was introduced during the fit routine, to account for small angular misalignment of the sample. Since Equation 3.7 is symmetric around $\theta = 90°$, the last data point ($\theta = 90° + \theta_{offset}$) was mirrored to ($\theta = 90° - \theta_{offset}$) to achieve visual uniformness, without loss of generality.

CHAPTER 4

MATERIALS

4.1 Donors: Diindenoperylene (DIP) and Pentacene (PEN)

The thesis presents a study on four different small molecule *D*/*A* systems. As donor materials, two widely used well-studied p-type small-molecule semiconductors were taken – diindenoperylene (DIP, $C_{32}H_{16}$) and pentacene (PEN). Both OSCs have proven to be successful materials in organic electronic applications, in particular, as donors in OPV devices [149–151] and p-type semiconductors in OFETs [152,153]. The chemical structures of the compounds are shown in Figure 4.1. A DIP molecule consists of a perylene core conjoined with two indeno groups along the long molecular axis. PEN energy gap is smaller and the HOMO level is by ~0.5 eV higher than those in DIP (the energy levels in Figure 4.1 are provided in accordance with Refs. [2,154,155] and relevance for thin films). A PEN molecule is composed of five linearly-fused aromatic rings and is smaller than DIP. One of the aspects of the material choice for the study is a relative orientation of the TDM of the first HOMO-LUMO transition μ (depicted by yellow arrows in Figure 4.1). Typically for rod-like molecules, the TDM of DIP is oriented along the long molecular axis. In a PEN molecule due to the asymmetrical distribution of the HOMO, μ is oriented along the short molecular axis [156] (Figure 4.2), which makes the compound a good candidate to investigate the impact of the μ relative orientation on the CT between *D* and *A* molecules.

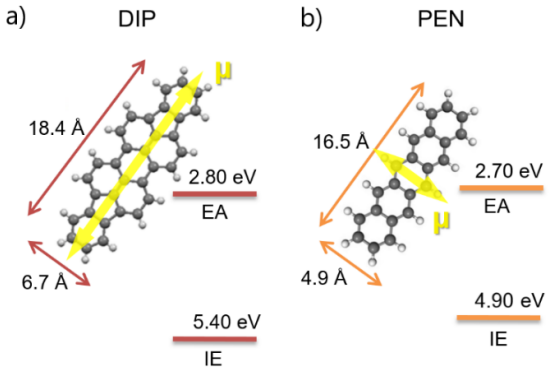


Figure 4.1. Small molecule donor OSCs used in the study: (a) DIP and (b) PEN. Atom color code: C – dark grey, H – light grey. Numbers of the molecule dimensions (including the van der Waals radius) and energy levels are relevant for the thin films in accordance with the reported crystal packings. Yellow arrows depict the orientation of the HOMO-LUMO transition dipole moment μ.

The monomer spectra in solution are shown in Figure 4.2. The DIP spectrum in acetone is taken from [109] and the spectrum of PEN diluted in 1,2-dichlorobenzene is taken from [157]. Both spectra reveal a Poisson-distributed vibronic progression with the $I_{0\text{-}1}/I_{0\text{-}0}$

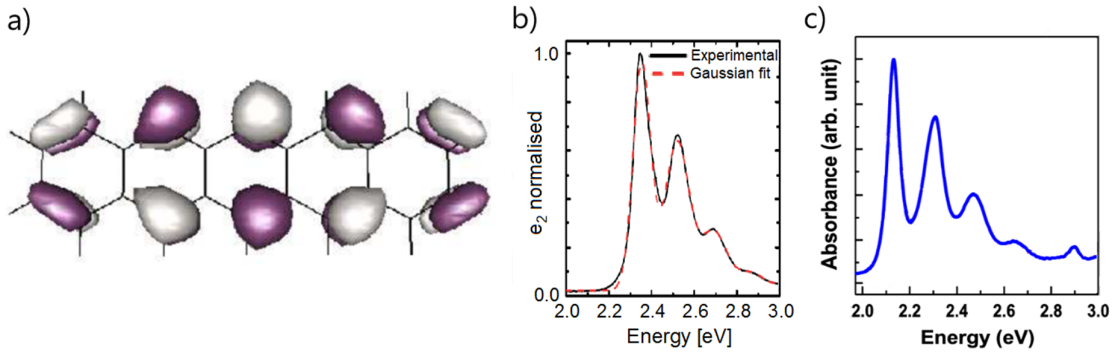


Figure 4.2. (a) Single particle HOMO wavefunction of isolated PEN molecule. The dark color represents a positive sign, the light color a negative sign; (b) and (c) UV/Vis optical absorption spectra in solution: (b) DIP in acetone and (c) PEN in 1,2-dichlorobenzene. The images are taken from [156], [109], [157] and modified.

transition intensity ratio of ~0.65-0.75, which corresponds to the Huang-Phys parameter smaller than unity [109]. Due to the smaller optical gap ΔE_{opt}, the PEN monomer spectrum is red-shifted by ~0.2 eV, which also leads to a difference in the optical properties in thin films (Section 7.2).

Both materials exhibit a herringbone packing motif predominantly in standing-upright orientation when growing thin films on an inert substrate at deposition temperatures above 300 K (SiO_x etc.) (Figure 4.3). The crystal lattice parameters of the polymorphs relevant for this thesis are listed in Table 4.1 including the bulk phase of PEN. Due to the herringbone packing, each unit cell consists of two translationally unequivalent molecules (DIP unit cell is monoclinic and PEN unit cells are triclinic).

Table 4.1 Unit cell parameters of DIP and PEN crystal phases.

Phase	a, Å	b, Å	c, Å	α, °	β, °	γ, °	V^{a}, Å^3
DIP (HT-phase) [158]	7.17	8.55	16.80	90	92.42	90	1029
PEN (thin film) [159]	5.92	7.54	15.63	81.5	87.2	89.9	689
PEN (bulk) [160]	6.06	7.90	15.01	81.6	77.2	85.8	692

[a] volume

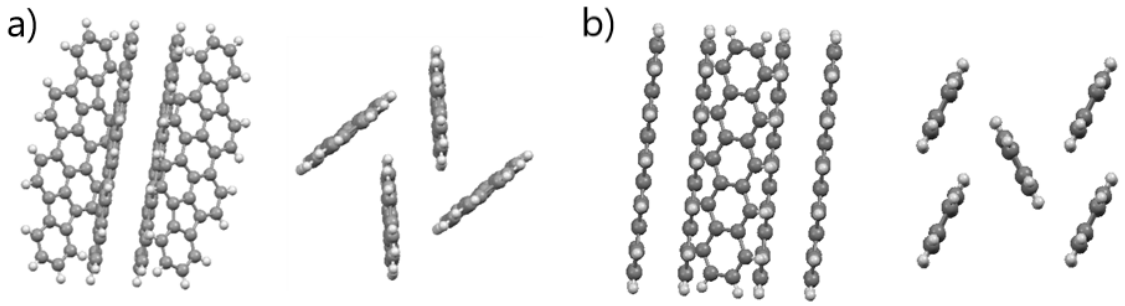


Figure 4.3. Molecular packing of (a) DIP and (b) PEN in thin films. Both materials exhibit a herringbone packing in thin films under the studied conditions.

4.2 Acceptors: Perylene Diimide Derivatives PDIR-CN_2 and PDIF-CN_2

The acceptor materials have been described in Ref. [1]. They are presented by perylene diimide derivatives (PDIs), a well-known family of electron-accepting small molecule organic semiconductors applied as active layers in OFETs [4,5,161,162] and OPVs [58,163–165]. PDIs have demonstrated outstanding chemical and thermal stability [166], processability, electron transport properties, high light absorption capability, high fluorescence quantum yields [29,164], and they hold the promise to surpass fullerenes once a proper functionality control is achieved [6,58,167]. PDIs consist of a perylene diimide core, responsible for a strong intermolecular π-π interaction driving a cofacial stacking, and thus, a high tendency to self-assembly. Due to this strong attraction forces, the molecules reveal extremely weak solubility; incorporation of different side substituents, which weaken the π-π interaction, allowed to solve the problem and made PDIs approachable for electronic application [29,163,164,168]. The side substitutions in an imide or bay position are easily changeable by synthesis and result in a variety of structures and morphologies and consequently physical properties of thin films and devices [163,167,169]. The properties of PDIs containing linear alkyl chain substituents at the imide position (such as N,N′-bis(n-octyl)-dicyanoperylene-3,4:9,10-bis(dicarboximide), PDI8-CN_2) have already been widely studied in literature [138,170,171]. Despite the evident importance of the side groups for the thin film properties, their influence on mixing behavior in BHJ with small-molecule donors and the CT properties have not been disclosed yet.

In the present thesis, the focus is on two variations of PDI compounds: N,N′-bis-(2-ethylhexyl)-dicyanoperylene-3,4:9,10-bis(dicarboxyimide) (PDIR-CN_2) with branched alkyl side chains and N,N′-1H,1H-perfluorobutyl-dicyanoperylene-3,4:9,10-bis(dicarboxyimide) (PDIF-CN_2) with linear fluorinated chains (Figure 4.4). These

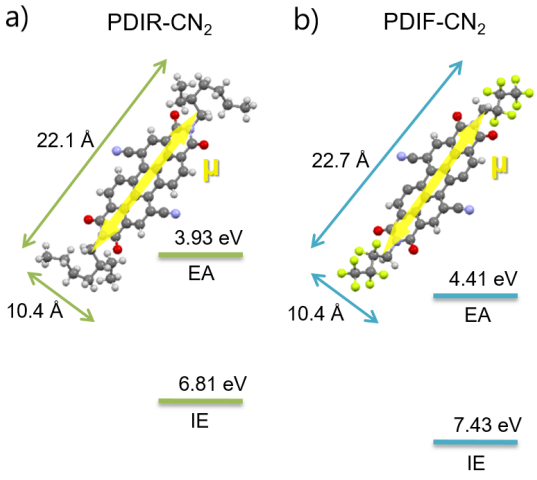


Figure 4.4. Small molecule acceptor OSCs used in this study: (a) PDIR-CN_2 and (b) PDIF-CN_2. Atom color code: C – dark grey, H – light grey, O – red, N – lilac, F - green. Numbers of the molecule dimensions and energy levels are relevant for the thin films in accordance with the reported crystal packings. Yellow arrows depict the orientation of the HOMO-LUMO transition dipole moment μ.

compounds are among the most interesting n-type small molecule OSCs due to their air stability and high field-effect electron mobilities with reported values in thin films of 0.22 and 0.53 $cm^2/V{\cdot}s$, respectively, exceeding 0.12 $cm^2/V{\cdot}s$ measured for PDI8-CN_2 [162,172,173]. As one can expect from the high electronegativity of fluorine, the main difference between the two compounds is the energy-level shift of PDIF-CN_2 compared with PDIR-CN_2. The IE of PDIR-CN_2 in thin films is 6.81 eV and the EA is 3.93 eV. PDIF-CN_2 in thin films has an increased IE of 7.43 eV and an EA of 4.41 eV. The transport gap in thin films remains nearly identical (2.88 and 3.02 eV, respectively) as well as the monomer optical gap (2.37 and 2.39 eV taken as the lowest peak of a vibronic progression of absorption spectra measured in solution, see Figure 4.5b), which contrasts with the case of full fluorination [174–176]. According to density functional theory (DFT) results obtained in several independent studies for this class of OSCs, the highest occupied and the lowest unoccupied molecular orbitals (HOMO and LUMO) of the compounds are concentrated on the perylene diimide core and, therefore, substituents in the imide positions are expected to have only a weak impact on their distribution [36,164,167] (Figure 4.5a). Hence, the strong change of electronic properties is supposed to stem from the environment in the solid state, i.e. the collective anisotropy of the quadrupole moment, while isolated molecules are less affected [177].

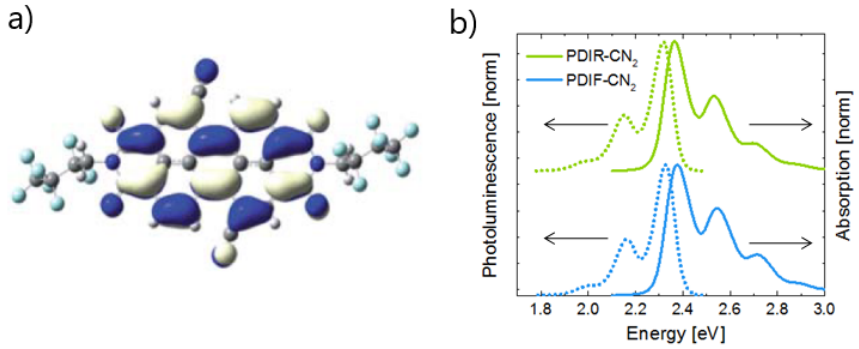


Figure 4.5. (a) LUMO distribution over PDIF-CN_2 molecule illustrating the negligible impact of the side substituents. The dark color represents a positive sign, the light color a negative sign. The image is taken from [33]; (b) Normalized absorption (solid) and photoluminescence (dotted) spectra in $CHCl_3$ solution.

In contrast to DIP and PEN, the acceptor thin films produced by vacuum deposition were not investigated with all thoroughness. A crystal structure of PDIR-CN_2 was determined for annealed spin-coated films and found to consists of highly tilted (inclination angle is ~53°) slip-stack (displaced along the long molecular axis) packed molecules [178] (Figure 4.6). PDIF-CN_2 films were found to exhibit no crystallinity when deposited at room substrate temperatures (RT). The crystal phase obtained by deposition at high substrate temperatures (HT) above 100 °C is composed of almost standing-upright (inclination angle is ~74°) slip-stacked (displaced along both long and short molecular axis) molecules [179]. The corresponding lattice parameters are provided in Table 4.2.

Table 4.2. Unit cell parameters.

Phase	*a*, Å	*b*, Å	*c*, Å	*α*, °	*β*, °	*γ*, °	*V*, Å^3
PDIR-CN_2 (spin-coated)[178]	6.30	8.81	16.56	88.32	84.6	110.63	854.55
PDIF-CN_2 (single crystal)[179]	5.23	7.64	18.8	92.51	95.25	104.73	722.52
PDIF-CN_2 (Langmuir-Blodgett ML)[180]	5.61	8.05	–	–	–	104.75	–

a and *b* are parallel to the substrate surface

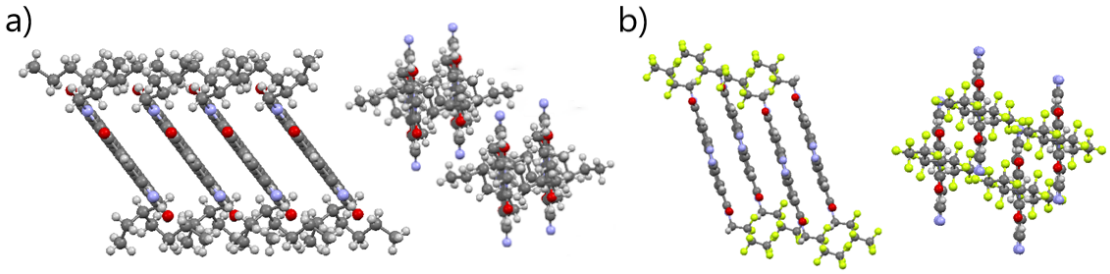


Figure 4.6. Molecular packing of (a) PDIR-CN_2 in spin-coated films and (b) PDIF-CN_2 in single crystal deposited at T_{sub} = 110 °C. In both cases a parallel stacking is observed with a displacement along the long and the short (small in PDIR-CN_2 and more prominent in PDIF-CN_2) molecular axes.

Part II

Results and Discussion

CHAPTER 5

GROWTH AND PACKING BEHAVIOR OF PDIR-CN_2 AND PDIF-CN_2 THIN FILMS

The following chapter is fully based on the published work Belova *et al.* [1]. This chapter provides a study on growth of two acceptor materials PDIR-CN_2 and PDIF-CN_2 whose chemical structures differ only in the imide substituents: branched alkyl chains $-C_8H_{16}$ and linear fluoroalkyl chains $-C_4F_7H_2$, respectively. In contrast to sterically flat and small molecules (e.g. PEN [181], DIP [123], sexithiophene (6T) [182], etc.), the bulky side chains of the studied compounds introduce some degree of steric hindrance for intermolecular interactions, affecting solid state packing during thin film formation, and thus induce specific structure-dependent optoelectronic properties in thin films. A real-time growth observation by X-ray diffraction methods allows to follow a transition from nearly uncoupled monomers to highly ordered bulk materials. The thickness-dependent crystallization processes are compared with real-time optical changes recorded by differential reflectance spectroscopy (DRS) [141]. Kinetic growth factors were explored by increasing the substrate temperature and the role of different substituents comparing growth and packing-dependent coupling behavior of the compounds.

5.1 Structural Investigation by X-Ray Diffraction

One of the main characteristics of PDIs is a strong non-covalent intermolecular interaction favoring 1D self-assembly in a face-to-face or slipped π-π stacking manner. Numerous kinds of such aggregation motifs (up to liquid crystals) have been widely studied for solution processes, [169,183,184] however the growth behavior during vacuum deposition still remains to be clarified.

Figure 5.1 shows reciprocal space maps (q_{xy} is the momentum transfer parallel to the sample surface, whereas q_z is perpendicular to the sample surface) measured post-growth on thin films of PDIR-CN_2 (Figure 5.1a-c) and PDIF-CN_2 (Figure 5.1d-h) grown by OMBD on silicon substrates at different substrate temperatures during deposition.

PDIR-CN_2 deposited at room temperature (RT) (Figure 5.1a) exhibits a diffraction pattern similar to a spin-coated, annealed film reported by Ferlauto *et al.* [178] corresponding to molecules tilted on the surface with a longitudinal displacement. The corresponding unit cell is triclinic and contains one molecule. The same unit cell is observed for films grown at substrate temperatures up to 120 °C. At this temperature, new weak features emerge in addition to the present peaks (see GIXD in Figure 5.2). These weak features, which have not been observed before, become more pronounced at higher

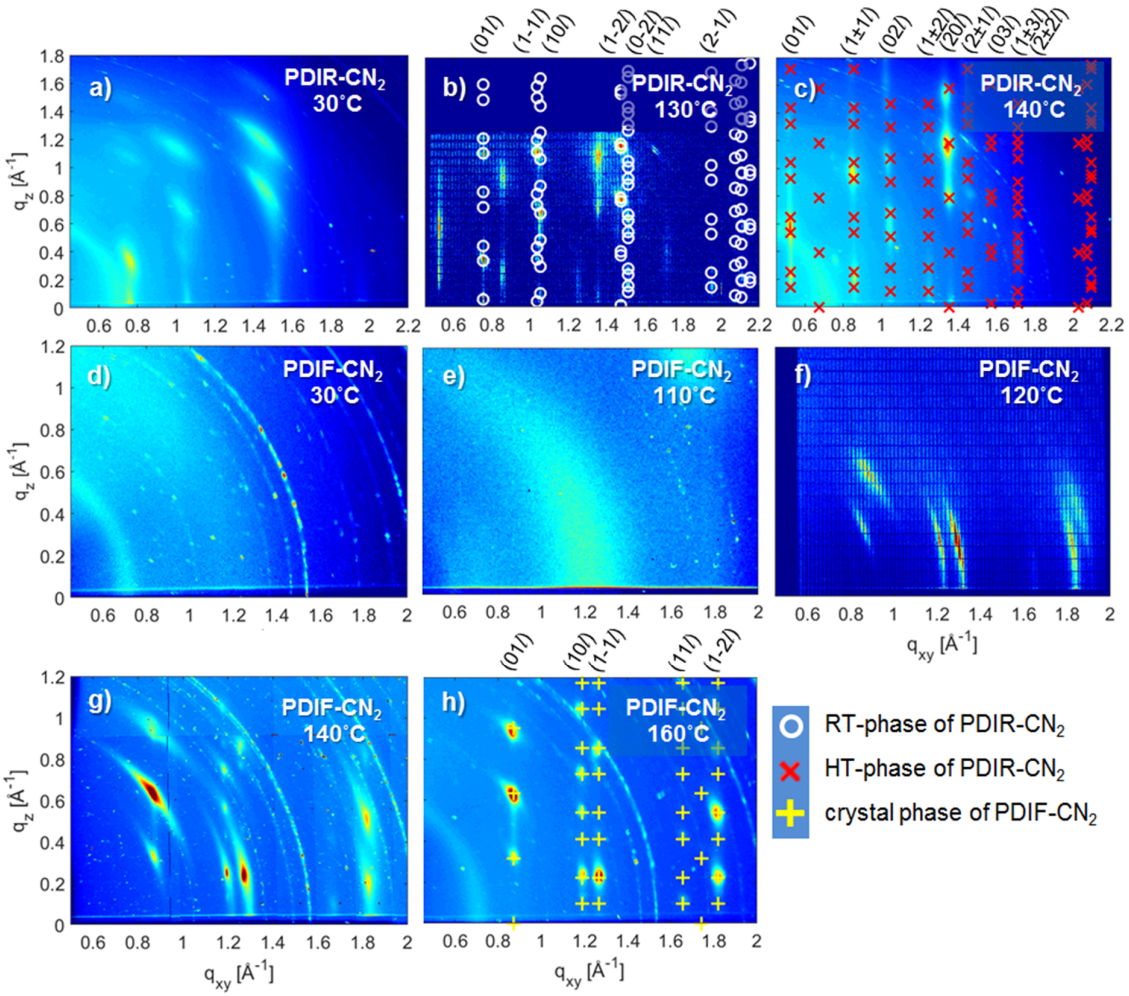


Figure 5.1. Reciprocal space maps measured post-growth: (a)-(c) PDIR-CN_2 and (d)-(h) PDIF-CN_2 grown at different T_{sub}. Calculated Bragg peak positions (white circles, red crosses, yellow stars – see legend) are provided without structure factor and taking the refractive index into account[185]. For figures (b), (c), and (h) the calculated Miller indices of the corresponding truncation rods are provided on top. The diffraction rings at q = 0.7 Å^{-1} present in (a), (c), (d) and (h) and q = 1.52 Å^{-1} present in (d), (g), and (h) are attributed to a kapton window and a Be window, respectively, and the feature in the upper-right corner of (e) is assigned to Si (111).

temperatures (T_{sub} = 130 °C, Figure 5.1b) and they are presumably associated with nucleation of a yet unreported polymorph. The improved crystallinity at 130 °C gives the opportunity to fit the unit cell parameters (see the white circles marking simulated positions of Bragg reflections in Figure 5.1b and the corresponding lattice parameters in Table 5.1) considering the film refractive index [185]. The improvement of crystallinity with increasing temperature followed by an enhancement of charge transport characteristics was reported for PDIR-CN_2 [162] as well as for a similar compound PDI8-CN_2 [5], a related compound containing a linear alkyl chain. With further increase of the substrate temperature (T_{sub} = 140 °C, Figure 5.1c) the room temperature (RT)-phase is almost vanishing and only the new high temperature (HT)-phase dominates. Red crosses show the fit (Figure 5.1c) of the HT-phase crystal structure which results in a

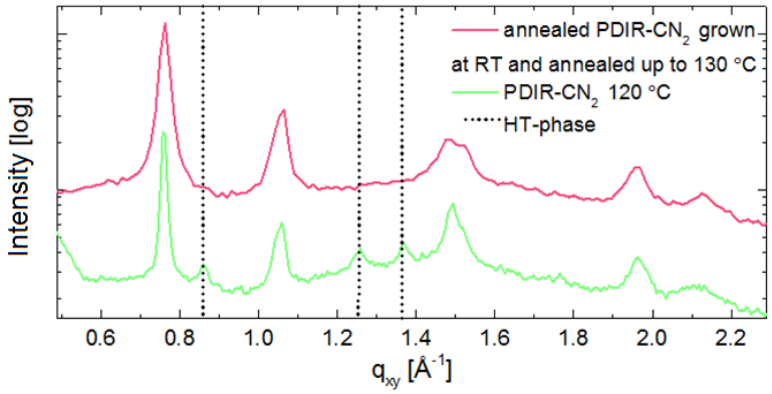


Figure 5.2. GIXD scans of PDIR-CN_2 RT films after annealing up to 130°C and PDIR-CN_2 grown at 120 °C. The Bragg peaks belonging to the HT-phase are marked with dotted lines.

monoclinic unit cell with a doubled volume (Table 5.1) and two molecules per unit cell. We note that the HT polymorph cannot be induced by annealing the RT film (kept at 130 °C for 1 hour, Figure 5.2). This observation suggests that more degrees of freedom for intralayer diffusion are required for enabling the phase transition.

In contrast to PDIR-CN_2, the second compound PDIF-CN_2 exhibits only a very weak crystallinity at RT [172]. In Figure 5.1d a weak scattering with an intensity maximum around 1.2 $Å^{-1}$ in the out-of-plane direction is observed giving a hint to a weakly-ordered lying down preferred molecule orientation (see Figure A.1 in Appendix for the full range q-map). With T_{sub} elevated up to 110 °C the diffraction feature is stronger with a maximum in the in-plane direction (Figure 5.1e). Based on the known crystal structure of PDIF-CN_2 single crystal [179], this indicates that the molecules adopt a more standing-up orientation, i.e. the tilt angle between the molecular long axis and the substrate normal is small, at higher T_{sub}.

Table 5.1. Calculated unit cell parameters.

	a, Å	b, Å	c, Å	α, °	β, °	γ, °	V, Å³
PDIR-CN_2 thin film RT phase(measured at 130°C)	6.44	8.99	16.59	87.52	86.21	112.55	882.66
PDIR-CN_2 thin film HT phase	9.33	12.07	16.93	105.24	90	90	1839.49
PDIF-CN_2 thin film(measured at 160°C)	5.53	7.52	20.4	87.12	101.45	106.31	797.99

The Bragg peaks in the q_z-range below 0.8 $Å^{-1}$ characteristic of a uniaxially ordered polycrystalline thin film occur at T_{sub} = 120 °C (Figure 5.1f). Bragg peaks at higher q_z appear at T_{sub} = 140 °C (Figure 5.1g). The reflections along the different truncation rods are clearly defined at T_{sub} = 160 °C (Figure 5.1h), the highest temperature at which PDIF-CN_2 adsorbs on the native SiO_x surface under the applied experimental conditions. The fitted unit cell parameters listed in Table 5.1 (the corresponding best fit of the Bragg reflection positions is shown in Figure 5.1h as yellow stars) differ slightly from the reported

single crystal structure [179] and the Langmuir-Blodgett monolayer (ML) [180]. Both PDIF-CN_2 and the RT-phase of PDIR-CN_2 exhibit an increase of the unit cell volume by ~10 % in comparison with the reported structures, however, this might be caused by thermal expansion due to measurements at high substrate temperature.

In order to investigate the stacking of the molecular layers in the out-of-plane direction XRR scans were performed. The data presented in Figure 5.3 and Figure 5.4 confirm the structural changes found upon increasing T_{sub} as described above. The PDIR-CN_2 films grown at high T_{sub} reveal an enhanced crystallinity, which can be seen through the increased (001) and (004) Bragg peaks intensity. The interlayer spacing d_z evaluated from the film grown at 140 °C (orange curve) does not deviate strongly from the RT-phase (Table 5.2). This might point towards a variation of the unit cell predominantly along the *a*- and *b*-axis. More dramatic changes were observed for PDIF-CN_2 following the transition from the amorphous (RT) to the highly textured film (160 °C, (003) and (004) Bragg reflections being the most pronounced).

Table 5.2. Out-of-plane thin film characteristics extracted from XRR profiles.

	d, nm	σ_{XRR}, nm	σ_{AFM}, nm	d_Z, Å	average inclination angle[a], °
PDIR-CN_2 RT	21.6	1.5	1.0	16.75	44
PDIR-CN_2 130°C	24.3	1.6	$1.1_{(120°C)}$	16.73	32
PDIR-CN_2 140°C	20.7	1.3	1.8	16.46	16
PDIF-CN_2 RT	29.4	2.0	0.8	–	
PDIF-CN_2 140°C	27.3	6.0	7.5	20.6	
PDIF-CN_2 160°C	20.4	2.5	1.9	20.4	

[a] Here, the inclination angle is the average angle between the long molecular axis and the surface. The approximate values are assumed using a single molecule model (see Figure 5.7) and given to illustrate the general temperature dependence.

An interesting effect of strong suppression of some of the Bragg reflections is observed in both cases. In order to quantify how the molecular arrangement influences the reflectivity scans, a fit of the reflectivity curves was performed using GenX [129]. Since each molecule consists of a perylene diimide core and two side chains, each ML in the model was divided into three sublayers with a void layer between MLs varying their relative electron density, thickness, and roughness. The fits reproduce the Bragg peak intensities accurately. The resulting electron density ρ_e profiles along the surface normal extracted from the best XRR are shown in Figure 5.5 and Figure 5.6 and the corresponding parameters are presented in Table 5.2. As seen from the fit, for PDIR-CN_2 the difference in electron density between the core and the side chains is pronounced and the ρ_e demonstrates a clear tendency towards increased oscillation amplitude at higher deposition temperature. One of the reasons for that behavior is the improved crystalline order in HT

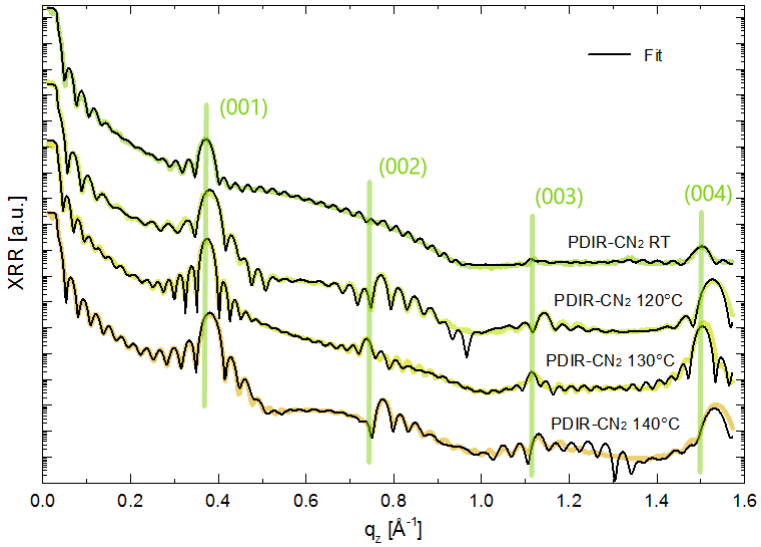


Figure 5.3. X-ray specular reflection curves of PDIR-CN_2 films deposited at different temperatures. Vertical lines indicate the Bragg peak positions for the RT scan. Black curves are fits using a multilayer model for the electron density. The curves are offset vertically for clarity.

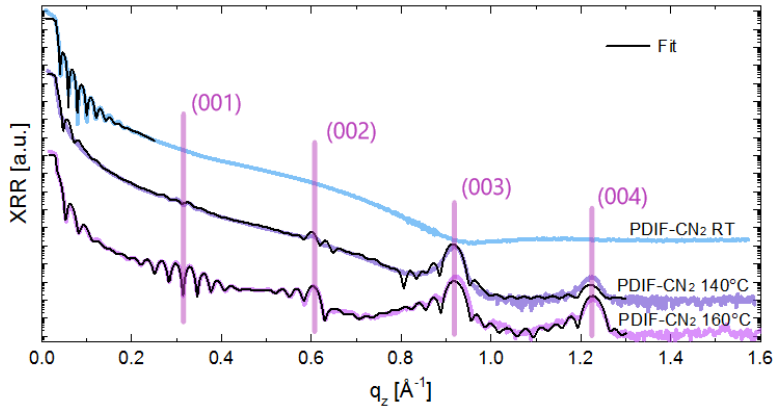


Figure 5.4. X-ray specular reflection curves of the PDIF-CN_2 films deposited at different temperatures. Vertical lines indicate the Bragg peak positions for the 160 °C scan. The black curve reproduces the fitted intensity using a multilayer model for the electron density. Vertical offset for clarity.

films that makes the contrast between layers more pronounced. Nevertheless, a more detailed view on the shape of the single oscillation is given in Figure 5.7a in comparison with the simulated electron density distribution along the vertical axis in Figure 5.7b. For the simulation three different molecular orientations relative to the substrate surface were modeled (Figure 5.7c). The sharpest distribution observed for the highest temperature (PDIR-CN_2 at 140 °C) corresponds to the smallest inclination angle (here the angle between the molecular long axis and the substrate surface) whereas the truncated shape is obtained for increased inclination angles towards more standing-upright position [186]. The smaller values of the inclination angle in PDIR-CN_2 films grown at HT are consistent with the presence of a different crystal polymorph.

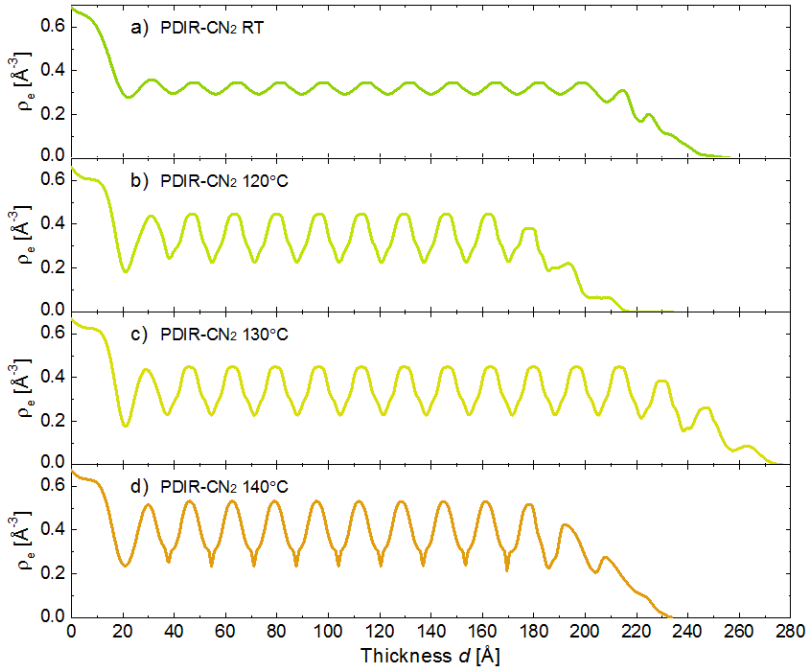


Figure 5.5. Calculated electron density profiles extracted from the fit of the XRR curves for PDIR-CN_2 films deposited at different temperatures.

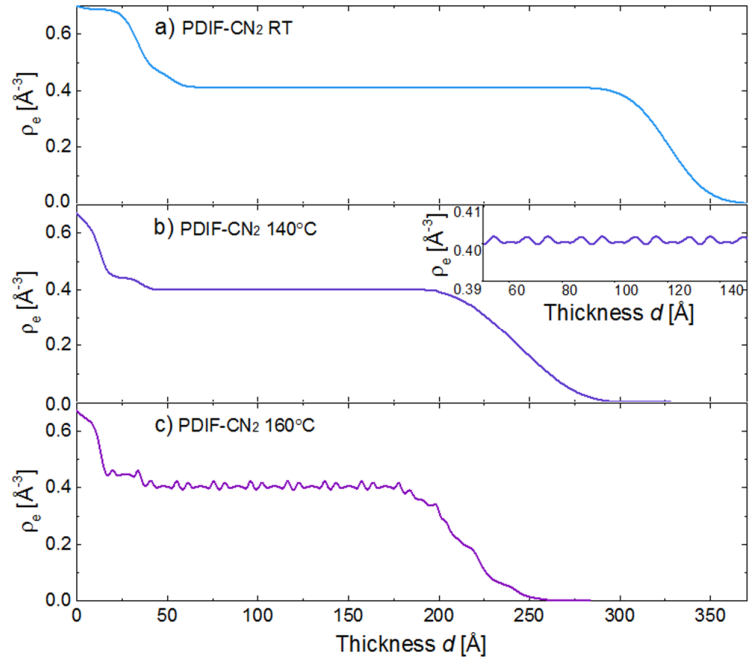


Figure 5.6. Calculated electron density profiles extracted from the fit of the XRR curves for PDIF-CN_2 films deposited at different substrate temperatures. The inset shows a zoom-in of the variation of the electron density at 140 °C.

The main difference between the fit and the model is the distribution width, which does not change in the former case. This can be explained by the simplification in the model where a single molecule with the side chains in the folded conformation is used, whereas

in real films the chains due to their flexibility may take various conformations inside a molecular array. Also, a molecule may rotate around its long axis keeping the interlayer spacing constant despite of a small decrease of the inclination angle. Nevertheless, the model demonstrates the general trend of highly tilted PDIR-CN_2 molecules in films prepared at high substrate temperatures, which is in agreement with our optical data (see Section 5.2).

For the nearly amorphous PDIF-CN_2 at RT in the absence of a Bragg peak a simple model with a single organic layer was used. Thus Figure 5.6a describes the average electron density of the film. The electron density ρ_e of 0.4 Å^{-3} is similar to the average in crystalline films. Unlike PDIR-CN_2, the standing PDIF-CN_2 molecules exhibit only weak modulations of the ρ_e (Figure 5.6b,c). The low contrast variations in ρ_e for PDIF-CN_2 at 140 ˚C are visible in the zoomed-in inset. Films deposited at 160 °C are strongly crystalline but due the high electron density of the side chains the contrast between molecular core and side chains is very small. When compare both PDIR-CN_2 and PDIF-CN_2 molecules, the ρ_e of the fluorinated chain is higher (0.420 Å^{-3}) than the ρ_e of the alkyl chain (0.312 Å Å^{-3}) and the perylene diimide backbone (0.405 Å^{-3}) due to the higher atomic number of fluorine atoms (the values are taken from the HT fits).

In addition to information on the crystal structure, XRR is a precise method to determine thickness and roughness. These parameters extracted from width and depth of

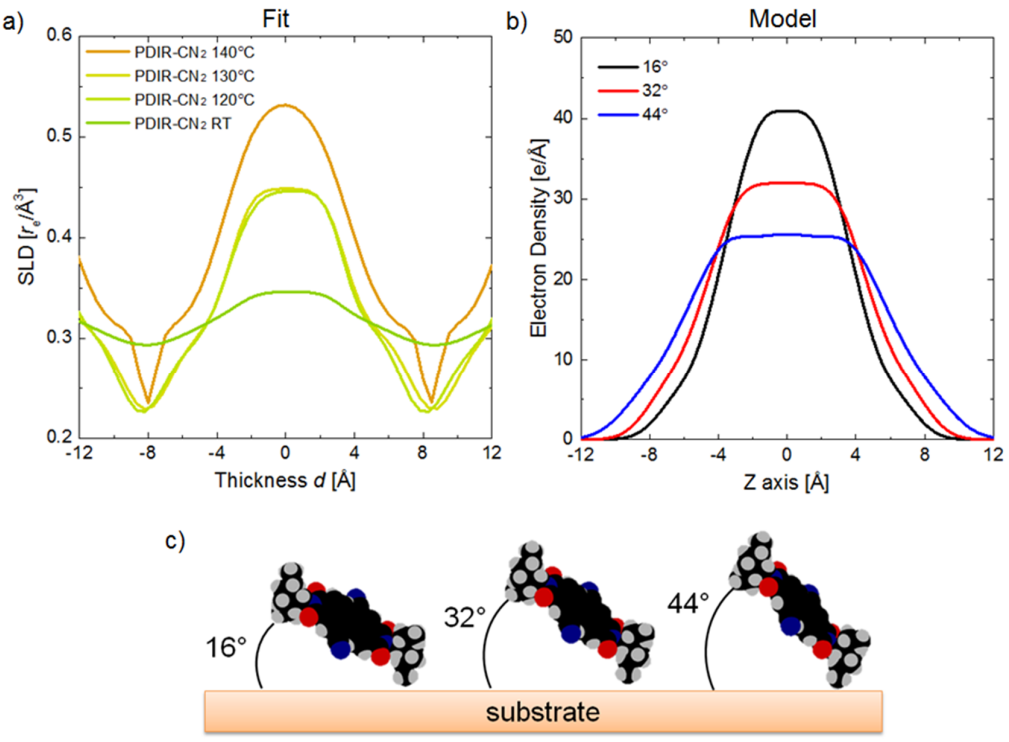


Figure 5.7. (a) Calculated electron density obtained from Figure 5.5 with a focus on a single ML. (b) Simulated electron density profile projected on the vertical axis for different PDIR-CN_2 molecule orientation varying the angle between the long molecular axis and the horizontal plane. Note, that the distribution width depends on the side alkyl chains conformation, for which folded chains are used in the model, whereas in films the chains might be straightened out (c) Sketch illustrating the orientation change used in the model.

the Kiessig oscillations (i. e. the interference oscillations at low q_z) are shown in Table 5.2. All PDIR-CN_2 films exhibit a small surface roughness (σ does not exceed 2 nm) and no strong changes upon the temperature increase are observed. However, the roughness of PDIF-CN_2 films change non-monotonously with the substrate temperature. It changes from a very smooth film with ($\sigma \approx 2.0$ nm) to a much rougher surface ($\sigma \approx 6.0$ nm) and then, with the further temperature increase, the film becomes smooth again ($\sigma \approx 2.5$ nm). For further investigations of this behavior and other surface properties the reader is referred to the discussion of the AFM images further below.

5.2 Optical Absorption Spectra

The in-plane ($\varepsilon_{2,xy}$) and out-of-plane ($\varepsilon_{2,z}$) component of the dielectric function (i. e. parallel and perpendicular to the substrate plane, respectively) of different PDIR-CN_2 and PDIF-CN_2 thin films are shown in Figure 5.8 in comparison with the absorption spectra in solution. The spectral shape of $\varepsilon_{2,xy}$ of PDIR-CN_2 films does not deviate strongly from the solution one, although a significant red-shift of about 200 meV is present. An interesting observation is that the magnitude of the lowest transition $I_{0\text{-}0}$ (at 2.18 eV) is increasing with T_{sub} as well as its ratio to the second vibronic peak (at 2.32-2.40 eV): $I_{0\text{-}0}/I_{0\text{-}1}$ for the RT film is ~1.3 and increases up to ~3.0 in the 140 °C film.

Also, a substructure of the vibronic peaks in the 140 °C film (e. g. at 2.3 and 2.5 eV) shows up giving a hint towards the presence of a second component. The out-of-plane component is much less intense, which is explained well by the highly tilted molecular orientation with a transition dipole moment μ mostly located in the xy-plane. Furthermore, the 0-0 out-of-plane transition undergoes a splitting appearing at T_{sub} = 120 °C, which becomes very pronounced at T_{sub} = 140 °C. This feature is possibly a Davydov splitting keeping in mind the HT-phase with two molecules per unit cell as shown before. Both ε_2 spectra were fitted with Gaussians to confirm the presence of two Davydov components in the optical transitions. The fit is provided in Figure A.2 in Appendix. The temperature dependent spectral changes are also consistent with the orientational changes towards more lying down molecules of the HT-phase (Table 5.2). Due to the Davydov splitting being an anisotropic effect sensitive to the intermolecular geometry [110,114] and the transition dipole moment of PDI being oriented along the long molecular axis, the decrease of the inclination angle in PDIR-CN_2 at 140 °C film results in an intensity increase of the lowest transition (0-0), which belongs to the low energy Davydov component oriented in the in-plane direction.

PDIF-CN_2 thin films reveal a qualitatively different optical behavior (Figure 5.8c,d). The RT film exhibits a small red-shift of only 40 meV compared to the solution spectrum and a similar shape for both anisotropic components with the $I_{0\text{-}0}/I_{0\text{-}1}$ ratio close to unity (whereas in solution the ratio is ~1.5). The similarity with the spectrum in solution can be explained by the low crystallinity of the thin films which leads to reduced intermolecular interaction and therefore to an optical response of the molecular aggregates similar to that of the single molecule. Nevertheless, the distortion of the Poissonian Franck-Condon vibronic progression determined in solution (Figure 4.5b and 5.8) evidences that a weak

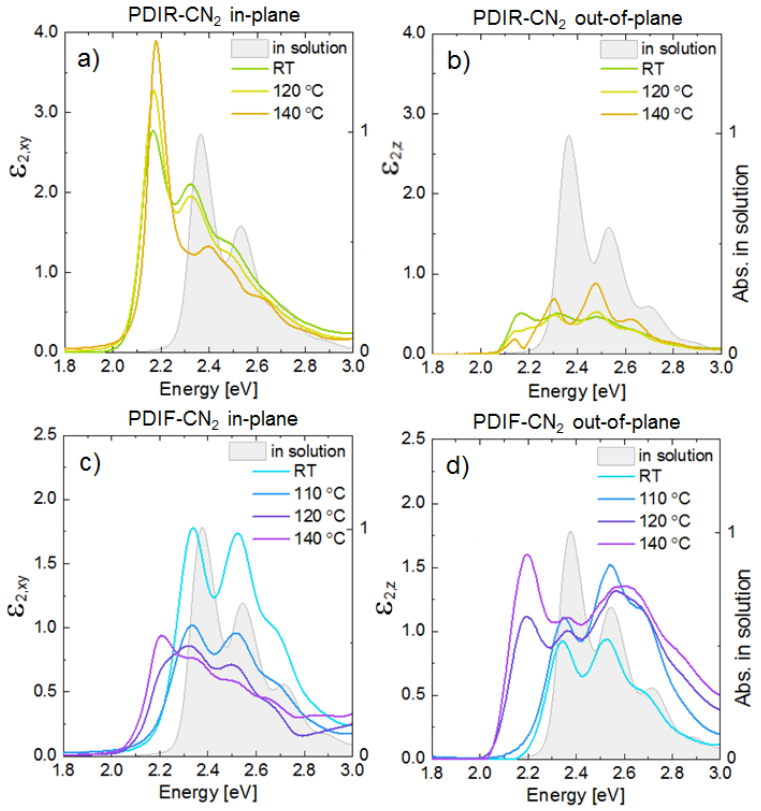


Figure 5.8. Dielectric function of the in-plane (a) and (c) and out-of-plane (b) and (d) components of thin films prepared at different T_{sub} in comparison with absorption spectra in solution. Up: PDIR-CN2, bottom: PDIF-CN2.

coupling is still present. As in the previous case of PDIR-CN2, the horizontal component is also stronger here although the difference is not as dramatic (only twofold instead of fourfold). This is consistent with the observation of a weak preferred in-plane orientation in the almost disordered film (Figure 5.1d). When growing at higher substrate temperatures, the absorption spectrum undergoes significant changes. First, the horizontal and vertical components swap their relative intensities as a consequence of the orientational change when going from a weakly ordered to a crystalline film where molecules stand up-right relative to the substrate surface. At 110 °C a blue shift of the absorption maximum for the out-of-plane direction towards 2.6 eV is observed. Moreover, a pronounced red-shifted transition around 2.2 eV similar to the one in PDIR-CN2 emerges in both the in-plane and out-of-plane direction as T_{sub} is further increased. This coincides with the long-range crystal structure formation in PDIF-CN2 thin films above 120 °C (Figure 5.1e-g).

5.3 Real-Time Study: GIXD and DRS

The next section provides a discussion on the structure formation and phase behavior at early growth stages, for which the crystalline structure evolution was monitored by GIXD scanning *in situ* and real-time during film growth. The resulting film thickness-

dependences for both compounds grown at room and high substrate temperature are plotted as 3D surfaces in Figure 5.9a-d. The elevated temperatures of 130 °C and 140 °C were chosen to show the coexistence of both polymorphs in PDIR-CN$_2$ films and the crystalline phase in PDIF-CN$_2$ films. The observable q-range corresponds to a horizontal cut through the q-maps in Figure 5.1 at q_z close to zero.

The Bragg peaks in PDIR-CN$_2$ of the RT crystal phase appear after the first 4 nm at q_{xy} of 0.76 and 1.06 Å^{-1} as the strongest features (Figure 5.9a). Taking into consideration the vertical lattice spacing d_z of 16.8 Å as deduced from XRR, this thickness corresponds to the formation of the 3rd ML. At T_{sub} = 130 °C (Figure 5.9b) structural features of both crystal phases are arising simultaneously after 3 nm i.e. earlier than in the first case – when the two first MLs are completed. Disordered PDIF-CN$_2$ at RT exhibits only a weak scattering feature at q_{xy} = 1.2 Å^{-1} (Figure 5.9c). In contrast to the relatively fast nucleation process of PDIR-CN$_2$ any signs of crystallization in PDIF-CN$_2$ at T_{sub} = 140 °C are not observed until a thickness of about 8 nm is reached (Figure 5.9d) corresponding to about 4 MLs considering d_z = 20.4 Å as deduced from XRR.

The real-time GIXD data were fitted using Gaussian functions. This allows the calculation of the coherently scattering island size l_s according to the Scherrer formula (Section 4.2). The evolution of l_s and the integrated peak intensity versus film thickness are shown in Figure 5.10a. Faint peaks at the initial stages of the growth could not be fitted and l_s is set to zero for these time points. l_s does not vary strongly during film deposition except at the beginning of growth up to 5 and 3 nm for PDIR-CN$_2$ at RT and at 130°,

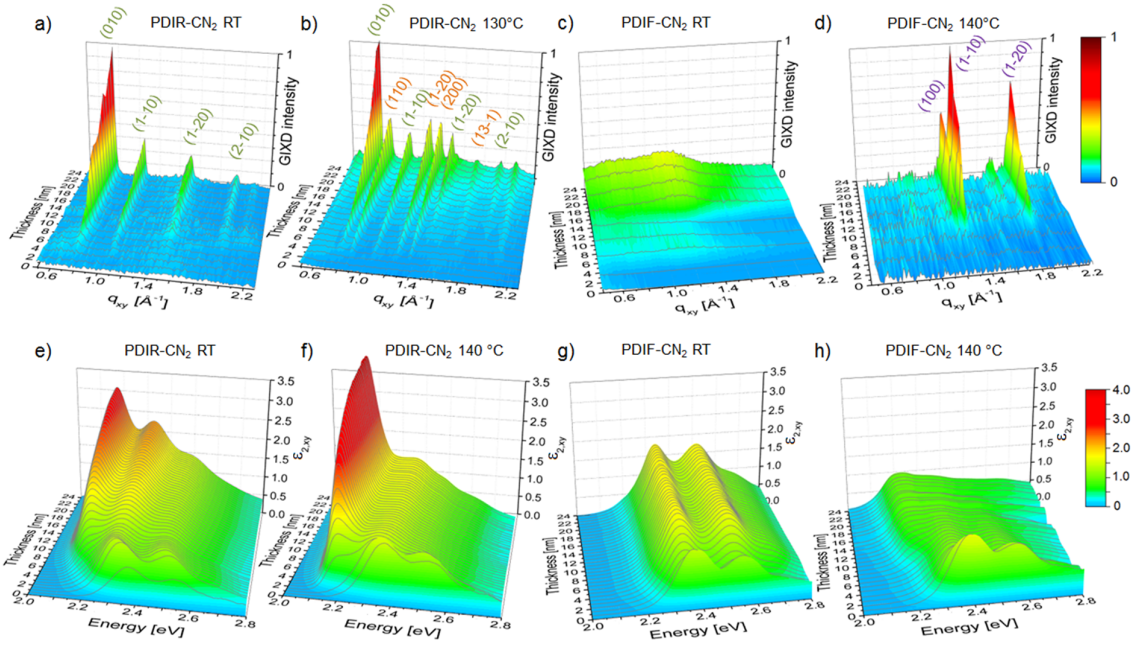


Figure 5.9. (a)-(d) Real-time GIXD plots. The vertical axis corresponds to the normalized intensity. The intensity of PDIF-CN$_2$ at RT in absence of strong peaks is scaled relatively to PDIF-CN$_2$ at 140°C. The Miller indices are shown for clarity only for the most pronounced peaks, but the intensities may include contribution of multiple reflections (see Figure 5.1), green labels stand for the RT-phase and orange labels – for the HT-phase of PDIR-CN$_2$. (e)-(h) Dielectric function spectra determined by fitting DRS data recorded during growth.

respectively. The absolute l_s values are larger at high T due to a thermally enhanced crystallinity although both phases reveal similar trends. l_s in PDIF-CN_2 at RT does not exceed 2 nm, which corresponds to few neighboring molecules. At high temperature the crystal size stays constant throughout the whole thickness (12-17 nm) as soon as the peaks are detected.

The intensity of the RT-phase in PDIR-CN_2 at RT and the HT-phase in PDIR-CN_2 at 130°C is growing linearly during film growth indicating a constant increment of the number of crystalline grains as a function of amount of material (Figure 5.10b). Although both phases are developing in parallel at an early growth stage, the intensity of the RT-phase in PDIR-CN_2 at 130°C film exhibits a non-linear growth behavior overtaking the HT-phase around 10 nm. Since the grain size stays constant this evidences an increase of the RT-phase nucleation. In contrast, with a further T_{sub} increase the HT-phase is clearly dominating in PDIR-CN_2 at 140°C as was observed (Figure 5.1c). The intensity of the PDIF-CN_2 crystalline phase grows linearly.

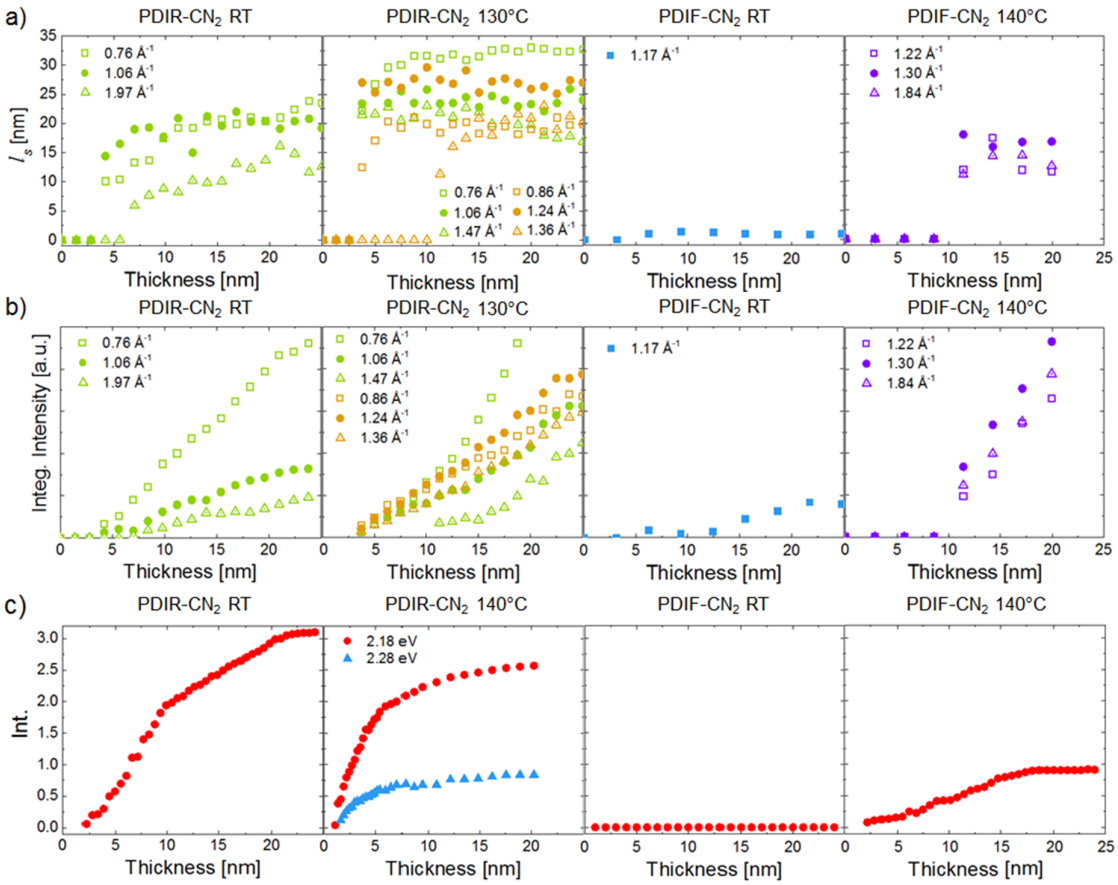


Figure 5.10. (a) Coherently scattering island size l_s extracted from real-time GIXD, (b) corresponding integrated peak intensity. Numbers in legends stand for q_{xy}-positions of the corresponding peaks used for data fitting, green and orange symbols indicate the RT-phase and the HT-phase in PDIR-CN_2 at 130 °C, respectively. (c) Intensity of the lowest electronic transition at ~2.2 eV determined from DRS, assigned to the intermolecular coupling in a crystal phase as a function of the film thickness. For PDIR-CN_2 at 140 °C two Davydov components of the lowest transition are shown.

The two compounds examined in this study have a similar chemical structure and exhibit almost identical absorption spectra in solution. However, in the condensed state their optical responses vary dramatically not only from one compound to another but also between different intermolecular arrangements. Therefore, in order to follow possible transitions in the optical properties in situ and real-time, DRS measurements were performed (Figure 5.9e-h).

It is remarkable that in all presented cases the spectral shape of the first ML (approx. 1.5-2 nm) is almost identical to the solution spectrum, i.e. a non-coupling arrangement. Here, only a small red-shift induced by the environment appears until the first ML is complete. Also a slight decrease of $\varepsilon_{2,xy}$ after this thickness is observed. A new low-lying transition shows up at 2.2 eV in all crystalline films except for PDIF-CN_2 at RT, where the shape of the in-plane dielectric function remains unchanged due to the absence of long-range order in the film. The new absorption band at 2.2 eV is appearing after the first ML in PDIR-CN_2 at 140 °C and growing earlier in comparison with the RT film. Thickness intervals over which the peak intensity is increasing – from 5 to 16 nm and from 2 to 8 nm for the RT and HT films respectively – coincide with the saturation times of the crystal grain sizes for these cases. These observations are in good agreement with the enhanced crystallinity of the high temperature film and confirm the intermolecular electronic coupling as a reason for such a behavior. This trend is delayed in PDIF-CN_2 (140 °C) as a consequence of the later structural stabilization, since the diffraction peaks are observed at thicknesses above 8-10 nm. The comparison between evolutions of the crystal phases and the lowest electronic transition is provided in Figure 5.10c. Thus, Figure 5.10c shows the evolution of the lowest electronic transition appearing during the film growth at the energy of 2.2 eV observed for PDIR-CN_2 at RT, PDIR-CN_2 at 140 °C and PDIF-CN_2 at 140 °C and assigned to the intermolecular coupling enhanced due to crystal phase formation. The DRS spectra in Figure 5.9e-h were fitted with Gaussians to obtain the peak intensities normalized to the final $\varepsilon_{2,xy}$ value afterwards. In case of PDIR-CN_2 at 140 °C the optical spectra were fitted with a doubled number of Gaussians confirming the suggested Davydov splitting of the molecular electronic states (the fit is provided in Figure A.2). The intensity of the electronic transition tends to saturate or reveal a slope change similar to with the crystal grain size saturation in the corresponding film.

In order to better illustrate the variation of the dielectric function during the film growth an approach introduced Ghanbari *et al.* [187], who used an incremental change of the DRS signal as a function of time, was implemented. Here, the difference between the individual spectra of $\varepsilon_{2,xy}$ obtained as a fit result from raw DRS data is used (2D images of the $\Delta\varepsilon_{2,xy}$ in Figure 5.11a). In a simplified view three growth steps can be distinguished in each case as sketched in Figure 5.11b. At first, material absorbs randomly on the surface and its absorption resembles the monomer spectra of almost non-interacting molecules. Then after 0.5 – 1 ML the deposited molecules start to interact with newly arriving molecules which leads to their reorientation to some extent. The reoriented layer serves as a precursor for a crystalline phase or, in case of PDIF-CN_2 at RT, a weakly ordered phase with molecules tending to lie down. The evidence for transformation between the different spectral components is a reduction of the absorption (dark blue areas in Figure 5.11a) and

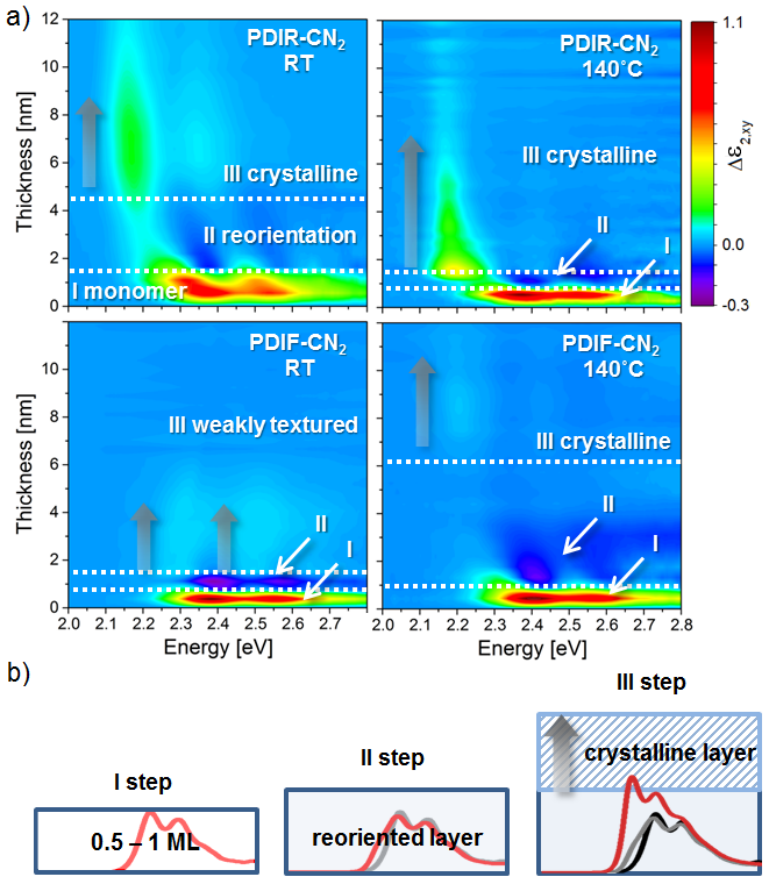


Figure 5.11. (a) $\Delta\varepsilon_{2,xy}$ spectra based on the data set from Figure 5.9e-h revealing incremental changes in absorption at early growth stages. The grey arrows are a guide to the eye. (b) Sketch associating the spectral and structural changes in the films.

the smooth red-shift in case of crystalline samples (with the exception of PDIF-CN_2 at RT) in step II. Therefore, the contribution to the resulting spectrum from the material of step I is no longer observed, whereas all spectra in step III present a combination of the reoriented and crystalline layers. The border between steps II and III is consistent with the thickness after which the crystalline peaks are observed in real-time GIXD data.

The described phenomenon is in contrast to what was observed for highly crystalline, vertically aligned materials on SiO_x substrates such as DIP, PEN, perfluoropentacene or PDI8-CN_2 where optical changes caused by the crystalline structure formation are observed within the first ML [143,171].

5.4 Photoluminescence

Figure 5.12 depicts a comparison between temperature-dependent PL spectroscopy and the in-plane absorption. The films with a crystalline structure (i.e. PDIR-CN_2 grown at both room temperature and at 140 °C and PDIF-CN_2 grown at 140 °C) measured at a temperature of 20 °C (Figure 5.12a, b and d) reveal a nearly mirror-symmetric first band (at 2.08, 2.15 and 2.05 eV respectively) caused by intermolecular coupling as discussed

above. Along with this observation, Stokes shifts appear to be smaller in the case of PDIR-CN_2, i.e. 90 and 26 meV vs. 143 meV in PDIF-CN_2. The efficiency of such radiative transitions caused by the intermolecular coupling is very sensitive to the degree of spatial separation such as a x-/y-displacement or the tilt angle between molecules [113,188]. This might explain why in cases of the highly ordered films the high-energy transitions are not distinguishable at low measurement temperatures, when contributions from breathing and shearing vibronic modes decay [189]. Then the radiative recombination of the relaxed singlet excitons results in a strong rise of the emission with a resolved vibronic progression (a relaxed exciton) taking over below -100 °C. A similar behavior of two competing temperature-dependent contributions was observed for the photoluminescence spectra of 6T films [190,191]. Also the PDIF-CN_2 (140 °C) emission spectra contain a low-energy component at 1.78 eV visible while cooling down to -100 °C. In Ref. [161] this component was assigned to the long-lived excimer-like radiation which often stands out as a characteristic feature of a cofacial overlap in π-π stacks[138].

The singlet exciton emission bandshape of the molecular crystal lattice is not observed in the PDIR-CN_2 and PDIF-CN_2 films grown at RT (Figure 5.12a and c). In PDIR-CN_2 a

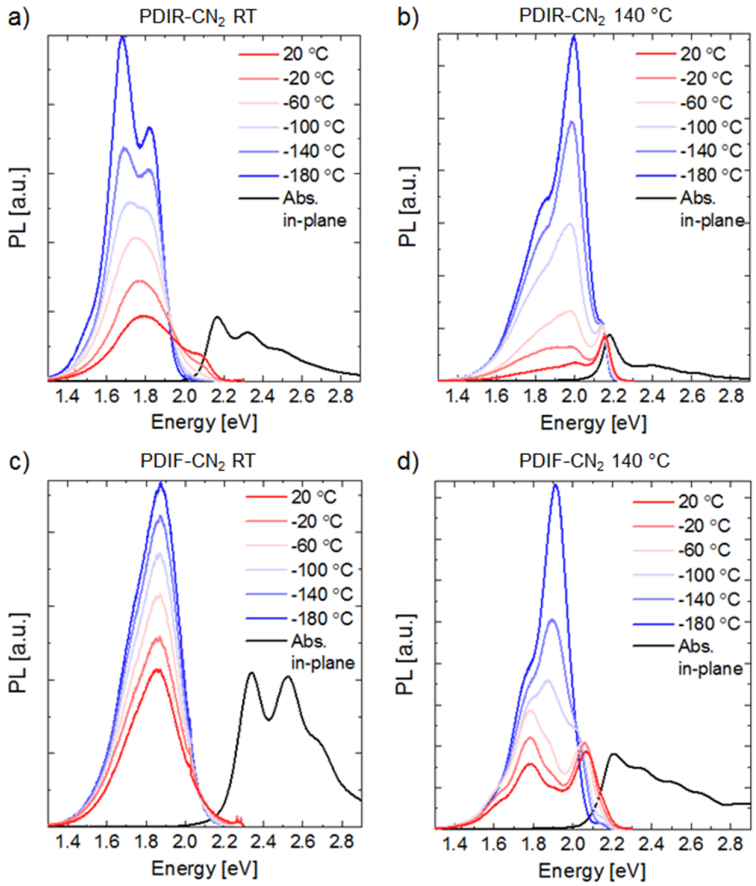


Figure 5.12. Temperature-dependent photoluminescence spectra recorded between 20 °C (red) and -180 °C (blue). Up: PDIR-CN_2 grown at room (a) and high temperature (b), bottom: PDIF-CN_2 grown at room (c) and high temperature (d). The black curves represent $\varepsilon_{2,xy}$ from Figure 5.8 rescaled to the 20 °C curves.

vibronically structured emission emerges at low temperatures as well as in HT deposited films, however, the transitions are significantly red-shifted and the spectral shape does not reveal the singlet exciton-like distributed vibronic peak intensities but a maximum around 1.69 eV. A possible explanation could be long-lived trap states [2]. The PDIF-CN$_2$ film shows a uniform featureless red-shifted broad emission band over the whole measured temperature range, which is typical for the excimer emission observed for perylene derivatives [37,138,168,192]. Although the excimer-like emission is usually ascribed to H-dimeric coupling in aggregates with an optimized face-to-face overlap, this recombination path is surprisingly effective in the only weakly ordered PDIF-CN$_2$ grown at RT. Nevertheless, as shown in numerous works on PDI dimers and trimers, the introduction of spacer groups indeed reduces the coupling strength, but does not fully suppress the excimer-like emission up to a center-to-center distance between two PDI subunits of 7-8 Å [193–195].

5.5 Morphology

When designing organic electronic devices, special attention should be paid to the active layer morphology due to a direct correlation between domain extension and device electrical performance [8,35,38]. The morphology of the samples was probed by AFM. The images together with the corresponding height distributions are shown in Figure 5.13. PDIR-CN$_2$ grown at RT exhibits a homogenous surface consisting of small grains and a high island density. The height variation around the average is ±2 nm and the root mean square roughness σ_{RMS} is on average 1 nm. The morphology of PDIR-CN$_2$ thin films changes significantly when growing them on a heated substrate. At T_{sub} = 120 °C the grain shape changes to elongated islands that exhibit distinct steps, revealing an anisotropic 2D growth inherent to other PDIs with alkyl chains [170,196]. Wide flat terraces leading to a low roughness appear at a higher substrate temperature of 140 °C, which is in good agreement with the low roughness determined by XRR. There are two explanations for the morphological differences between PDIR-CN$_2$ thin films grown at RT and at 140 °C: a) the enhanced diffusion at high substrate temperatures [197] along with low Ehrlich-Schwöbel barriers promoting a relatively uniform coverage [125] and b) the temperature dependent polymorphism. As shown above, the high temperature thin film nucleates in a different crystal structure than the low temperature film and hence, depending on the crystal structure different growth rates for lateral and vertical crystallographic directions may appear [124,196]. The step heights between the plateaus derived from the height distribution are 1.5 ± 0.5 nm, which is roughly the lattice spacing of a PDIR-CN$_2$ unit cell, which leads to the conclusion that each of the terraces consists of one layer of PDIR-CN$_2$ molecules. Generally, a Stranski-Krastanov growth mode i.e. layer-plus-islands is typical for PDIs [38,138,196,198].

The PDIF-CN$_2$ film grown at RT is the smoothest thin film of this series (σ_{RMS} derived from the AFM images is below 1.0 nm). The missing crystalline ordering in PDIF-CN$_2$ thin films grown at room temperature may account for the low roughness. The molecules spread evenly over the substrate without forming clusters. The small grain morphology of

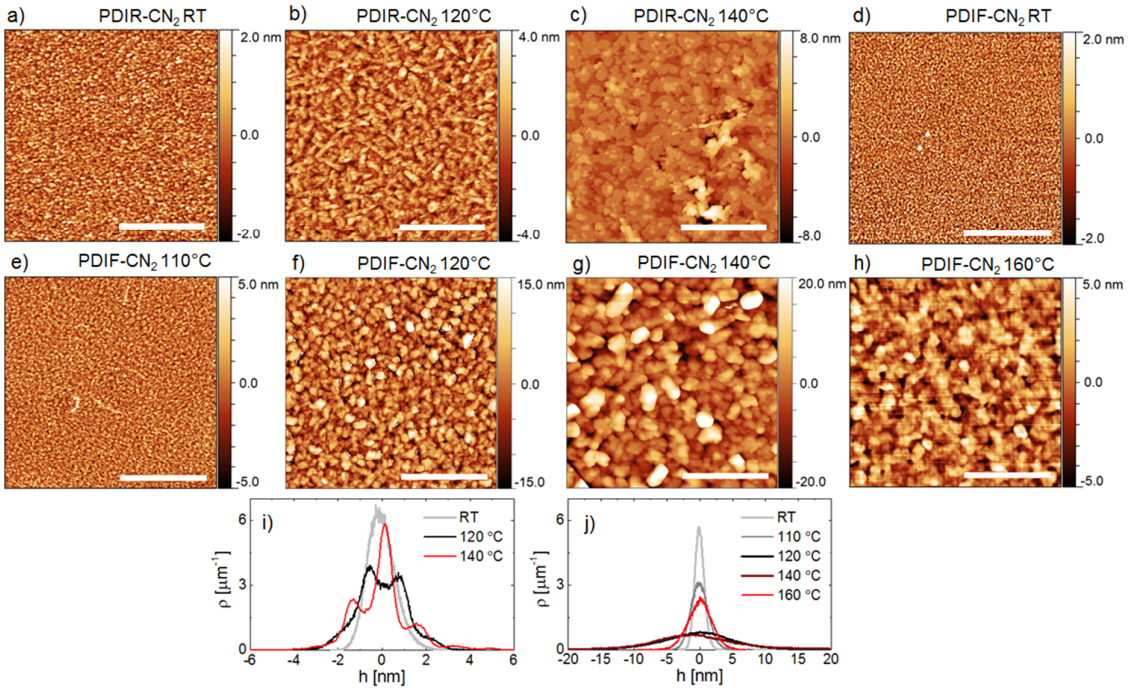


Figure 5.13. AFM images 5×5 μm of different PDIR-CN_2 films (a)-(c) and PDIF-CN_2 (d)-(h) with the corresponding height distributions (i) PDIR-CN_2 and (j) PDIF-CN_2. Length of the scale bar is 2 μm.

PDIs was suggested to be rich in inhomogeneities and structural defects [5]. A similar morphology is observed for PDIF-CN_2 at 110 °C. A strong trend to roughening can be seen when growing at 120 ˚C and 140 ˚C. Large 3D clusters with a σ_{RMS} of several nanometers form. The deviations from the average height reach up to ±15 and 20 nm in each case. The crystallization at high T_{sub} presumably drives formation of larger clusters. The growth rate along the crystallographic direction perpendicular to the substrate surface has to be increased compared to the rate of PDIR-CN_2. It was shown how the introduction of substitutions with different degrees of steric hindrance and introduction of fluorine atoms increase both surface diffusion and step-edge diffusion barriers [199–201]. However, going to the highest growth temperature of 160 °C the roughness decreases again due to formation of flatter domains, which is in good agreement with the XRR data. At this growth temperature, the enhanced diffusivity seems to efficiently balance the Ehrlich-Schwöbel barrier at the step edges of the crystalline molecular layers. Under these conditions, highly crystalline and smooth films can be obtained.

To summarize, for both compounds, a clear transition in the nucleation behavior which coincides with changes in the crystal structure can be seen. The continuous morphology with a minimized number of grain boundaries, the most beneficial situation for high charge mobility [35,172,202], can be achieved via the substrate temperature control.

5.6 Discussion

As pointed out in the introduction, the electronic structure of the perylene derivatives is considered to be not strongly affected by substituents in the imide positions in their single molecule state. However, all parameters which are crucial for device performance, i.e. charge transport properties, energy structure, photon absorption and emission, morphological organization, crystalline quality etc., are based on the growth behavior which strongly depends on interactions with the environment. The behavior of the compounds considered here contrasts to compounds with linear alkyl chains such as PTCDI-C_8 [196] and PDI8-CN_2 [138], which are growing in nearly upright standing fashion starting from the first ML fashion on SiO_x substrates. Despite the fact that partial fluorination is often considered to introduce a strong non-covalent stabilizing interaction [20,21,203,204], one can note here that PDIF-CN_2 generally reveals less tendency for crystallization than non-fluorinated compounds, such as PDIR-CN_2, PDI8-CN_2. Although the branched and fluorinated side-chains break the molecule's planarity in both cases [163], for the same deposition conditions PDIF-CN_2 requires higher thermal energy to achieve the energetically favorable orientation in the lattice. The same crystallization-obstructing effect was observed for perfluorinated cobalt phthalocyanine F_{16}CoPc [205] and in the more relevant family of DFH-*n*Ts, thiophene-based molecules with -C_6F_{13} chains, which are crystallizing upon deposition at a substrate temperature of 120-200 °C into a similar packing motif [15]. One is tempted to conclude that this is a general trend for compounds containing fluoroalkyl chains. The reason for this might be in the bulkiness and the larger van der Waals radius of fluorine atoms compared to hydrogen limiting the fluoroalkyl chain's flexibility [166,206]. A reasonable argument explaining the reduced contrast in the fitted electron density profile perpendicular to the substrate plane (Figure 5.6) is that the high electron density of the fluorinated chains can shield the perylene diimide backbones inhibiting the π-π intermolecular coupling. Interestingly, the structural transition to the long-range order occurs sharply almost in a step-like manner upon an increase of T_{sub}, which was observed by changes in the structural, morphological, and optical properties. In this context, one should bear in mind the difference between fluoroalkyl substituents and (complete/partial) fluorination of a molecular aromatic core when considering the fluorination effects.

The increase of thermal energy (substrate temperature) gives rise to structural changes in PDIR-CN_2 thin films, leading to the appearance of a HT-polymorph with two molecules per unit cell. The RT-phase consists of molecules tilted towards a substrate nested together in a 1D slipped π-π stacking with an offset along the long molecular axis (Figure 5.14a) due to shape complementarity. This is a beneficial arrangement for J-like coupling, although common PDI derivatives in the absence of spatial crowding tend to create an ideal face-to-face conformation in columnar stacks with the typical properties of H-aggregation. Indeed, a red-shifted 0-0 transition growing coherently with the crystal phase formation is observed. When the HT-phase appears in a film (starting from T_{sub} = 120 °C) the J-aggregation character enhances significantly: The intensity of 0-0 grows not only in absolute value but also relative to the next 0-1 transition. The anisotropic Davydov splitting

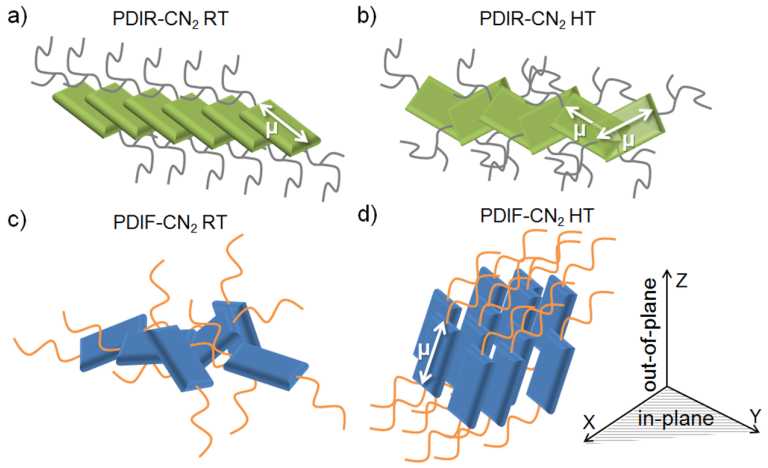


Figure 5.14. Schemes representing molecular arrangement in: (a) PDIR-CN_2 RT-phase, (b) PDIR-CN_2 HT-phase, (c) amorphous PDIF-CN_2 and (d) PDIF-CN_2 thin film crystal phase.

observed in both the in-plane and out-of-plane direction indicates twisting of the transition dipole moments of two molecules contained in the unit cell as illustrated in Figure 5.14b, similar to that described by Austin *et al.* [114]. The change from 1D elongated island growth of the RT-phase rich film to the isotropic 2D flat terrace growth of the HT-phase rich film observed with AFM could be caused by a change in crystal growth directions. A rotational offset configuration was found to be the third and deepest minimum of the binding energy in DFT calculations [167] and is widespread in PDI solution-processed supramolecular stacks [30,167] but rather rare in crystals [114,207]. Structural polymorphism upon vacuum deposition was also described for the parent perylene molecule [37], however, for the related compound PDI8-CN_2 with linear chains persistence of the same crystalline structure for a wide temperature range was observed [170].

The crystal phase of PDIF-CN_2 is arranged in a different way. As many other perylene derivatives with chains in the imide position it grows in a standing-upright manner (in contrast with the disordered RT films where a majority of molecules tend to lay down, Figure 5.14c) but with a more complicated interlayer organization. Despite the contribution of -C_7F_{14} chains, the typical π-π intermolecular perylene diimide core interaction is still dominant promoting a face-to-face configuration. Yet, the parallel stacking involves longitudinal and transverse offsets, i.e. along both the long and the short molecular axis creating a 2D chess-like pattern (Figure 5.14d). Such a 2D π-π stack packing motif has been suggested as more favorable in terms of electronic coupling and charge percolation pathways [36]. For such complicated structures the ideal classical cases of J-/H-aggregation are not straightforward to apply because the optical spectra (absorption and emission) contain characteristic features from both types. Similar cases were observed earlier, where it has been concluded that both kinds of couplings might be present at the same time. Their strength would depend then on the spatial separation in corresponding directions [208]. Also, the energies of low- and high-energy vibronic bands can be pushed down and up by coupling of Frenkel excitons with intermolecular charge transfer states and Coulombic interaction, respectively [109,110,114,209].

In summary, the growth process of two PDI derivatives during vacuum deposition was followed as a function of substrate temperature (Figure 5.15). At the first ML, almost identical non-aggregating states without long-range order were found due to a shielding effect of the side substituents, which is stronger in the case of the fluorinated chains. This is followed by a temperature-dependent transition to significantly different crystalline molecular packing motifs influenced by the geometry and chemical composition of the side chains. This results in unique optical and structural properties, in sharp contrast to both the amorphous and the monomer properties, which are not affected by the chemical modification of the side substituents as predicted by previous DFT studies.

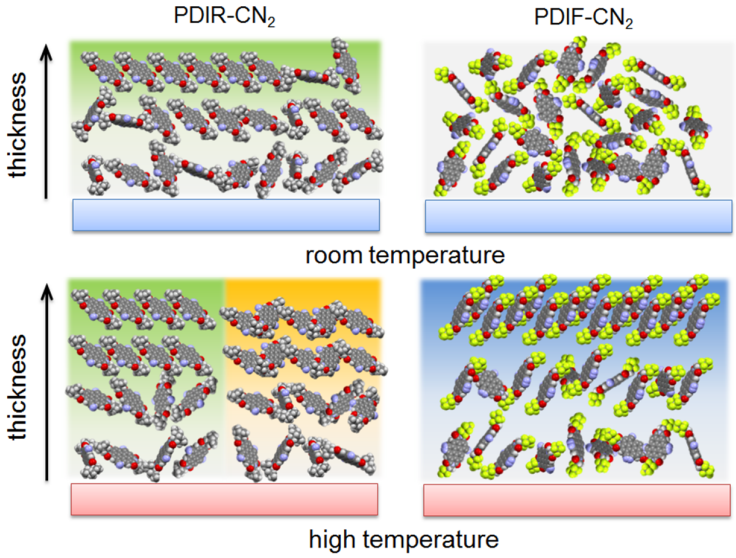


Figure 5.15. Sketch demonstrating thickness- and temperature-dependent growth of PDIR-CN_2 and PDIF-CN_2 thin films by OMBD.

CHAPTER 6

ANISOTROPIC ELECTRONIC COUPLING OF CHARGE TRANSFER STATES IN DIP:PDIR-CN_2

The following chapter presents a recently published study [2] of the CT effect in a weakly interacting OSC mixture of DIP and PDIR-CN_2 starting from morphological and structural investigations, via complementary forms of spectroscopy to the implications in device applications. Both donor and acceptor materials are structurally well defined and therefore can serve as a model system. DIP and PDIR-CN_2 have similar backbone size that enable good intermixing upon co-evaporation and, as a consequence, more interface area.

The chapter is organized as follows. In Section 6.1 morphological and structural properties studied by means of AFM, X-ray scattering, and NEXAFS are discussed. Evidence for the formation of a CT complex between DIP and PDIR-CN_2 is provided in the ground state by using Fourier transform infrared spectroscopy (FTIR) and ultraviolet photoelectron spectroscopy (UPS) and in the excited state by optical absorption and emission spectroscopies as described in the corresponding sections. In Section 6.4 the impact of CT states on charge separation and transport in photovoltaic devices is demonstrated. Finally, the findings are summarized and discussed with respect to the classification given in Introduction.

6.1 Structural Characterization

Prior to the examination of CT, the two compounds were characterized regarding the structural organization of the molecules during simultaneous or consecutive growth, since this is crucial for the formation of *D*/*A* interfaces. For this purpose, AFM, X-ray scattering, and NEXAFS measurements were applied.

AFM images of the thin films are shown in Figure 6.1 (for height profiles see Figure B.1 in Appendix B). The morphology of the pristine DIP film reveals a typical "wedding-cake-like" structure [210] with a step size 1.6-1.8 nm corresponding to one monolayer of upright standing DIP molecules and a root-mean-square surface roughness σ_{RMS} of 2.85 nm. For all mixed films, as well as pristine PDIR-CN_2 films, the grain sizes decrease significantly, which results in very smooth surfaces and roughnesses σ_{RMS} below 1 nm, and no clear molecular steps to distinguish. Therefore, based on these AFM results, no evidence of phase separation is seen.

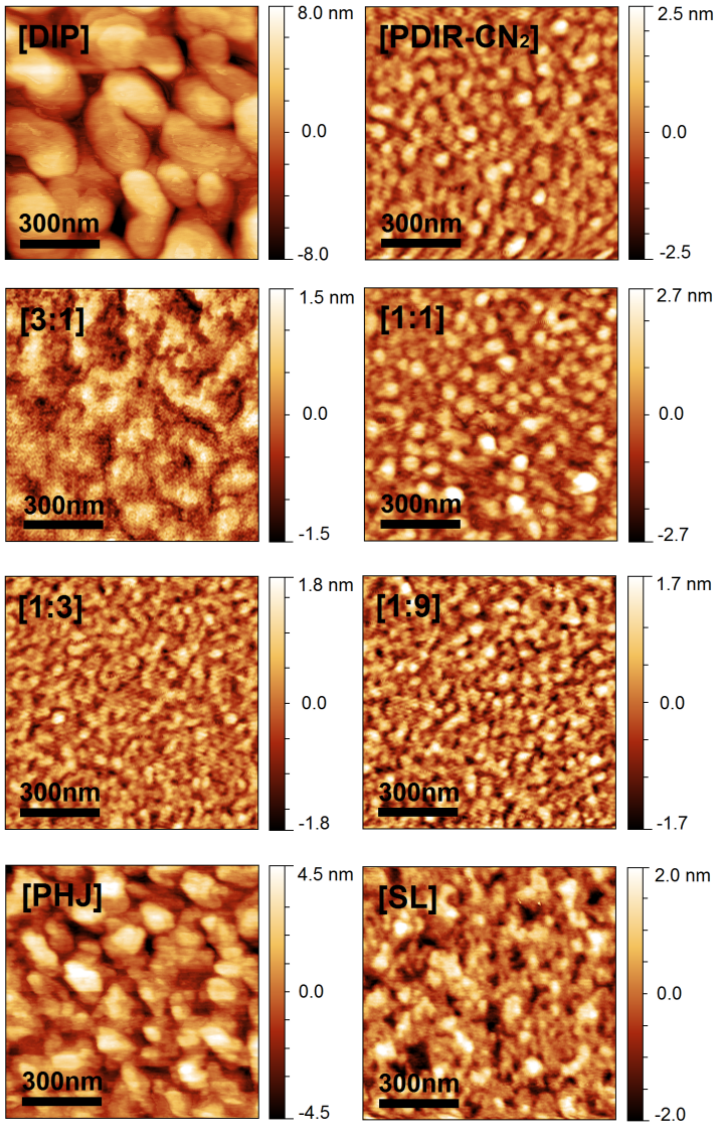


Figure 6.1. AFM images for pristine films, co-evaporated blends and heterostructures (the top layers of PHJ and SL consist of PDIR-CN$_2$ molecules). For surface profiles see Appendix.

The surface of the SL consists of similarly small grains with a roughness comparable to the molecular blends. The PHJ surface has a roughness similar to pristine DIP and also the top layer of PDIR-CN$_2$ adopts a grain size of about 115 nm comparable to the average DIP grain size underneath.

For more detailed structural information, X-ray scattering techniques, i.e. XRR and GIXD, were applied. Specular scans are shown in Figure 6.2a. The first Bragg peak of pristine DIP (red curve) is observed at q_z = 0.37 Å^{-1}, which corresponds to the standing-up or σ-orientation of DIP with an out-of-plane lattice spacing of $d_{(001)} \approx 16.9$ Å [210,211] and an inclination angle of ~83° of the molecular plane relative to the surface plane. One Bragg peak and a weak second-order reflection are observed in the XRR scan of the pristine PDIR-CN$_2$, for which the branched alkyl side chains inhibit long-range crystal formation

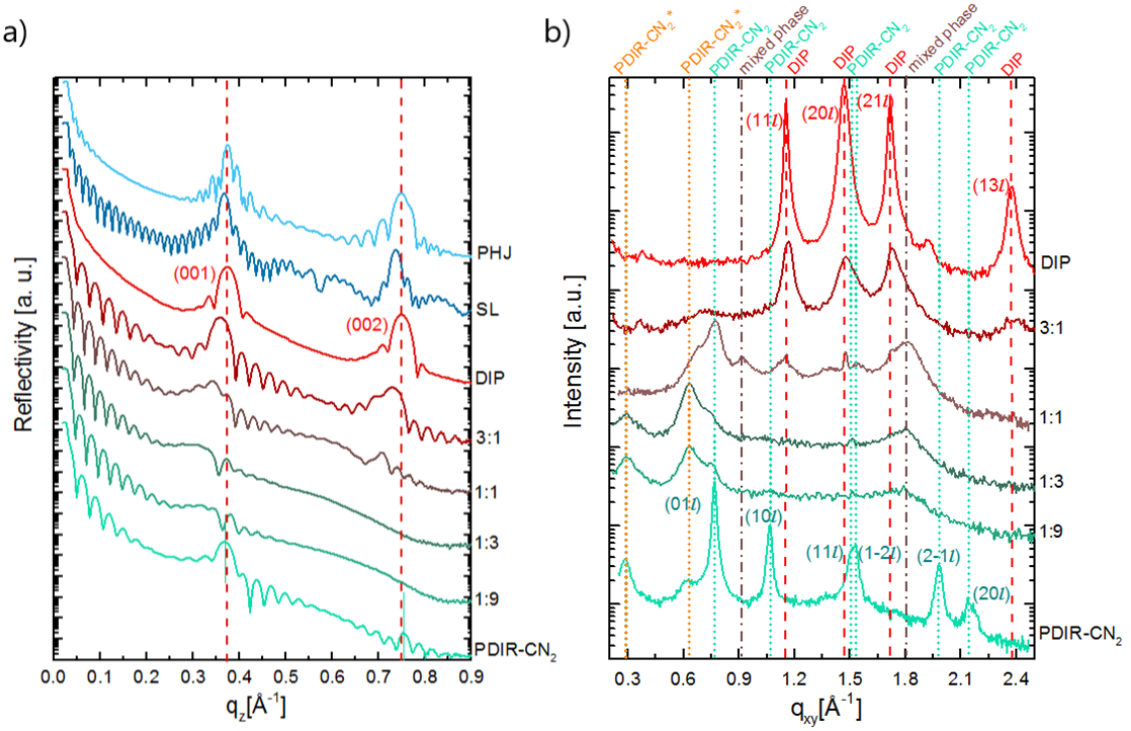


Figure 6.2. (a) XRR data for DIP:PDIR-CN_2 co-evaporated films and heterostructures. Dashed lines indicate the position of the 1st and 2nd order Bragg peak for DIP. The spectra are vertically offset for clarity. (b) GIXD data of DIP:PDIR-CN_2 films for different mixing ratios. For better peak visibility in 1:1 and pristine PDIR-CN_2 films of thickness 100 nm were used. All spectra are vertically offset for clarity.

as discussed in Chapter 5. The q_z-value of the Bragg peak from XRR scan of PDIR-CN_2 (lowermost curve) corresponds to $d_{(001)}$ = 17.1 Å, which almost coincides with pristine DIP. In the case of the blended systems the second-order Bragg reflection still persists in films with excess DIP (3:1) but disappears with further increasing PDIR-CN_2 fraction. The exact peak maxima of the co-evaporated films cannot be properly quantified through a strong interference effect [212]. Nevertheless, an apparent gradual shift towards lower q_z-points out to changes in the lattice parameter as discussed further.

A three-layer model (bulk Si-substrate – SiO_2 layer – organic film) was used to determine the film thickness d and roughness σ of the mixtures from the XRR (Table 6.1). Regarding planar heterostructures, PDIR-CN_2 molecules grown on top of a DIP layer adopt the same standing up configuration (Figure 6.2, uppermost curve) and form a layer with increased roughness, because of the rough DIP layer underneath. Roughness of the SL according to XRR is quite low, which may serve as evidence for layer-by-layer growth mode or preferential filling of gaps [212].

The results of GIXD experiments on pristine and co-evaporated films are shown in Figure 6.2b. Very strong in-plane reflections of pristine DIP are less intense and broader in non-equimolar mixtures with excess of pristine DIP molecules. In the equimolar mixture DIP reflections almost vanish, which demonstrates a high miscibility between DIP and PDIR-CN_2 molecules, forming a system wherein the two kinds of molecules are mixed

without noticeable phase separation [77]. PHJ and SL GIXD profiles present a simple superposition of pristine film patterns (Figure B.2).

Table 6.1. Summary of film parameters extracted from XRR fits and AFM roughnesses.

config.	thickness d (nm)	roughness σ (nm)	roughness AFM σ_{RMS} (nm)	$d_{(001)}$ (Å)
DIP	19.8	3.8	3.9	16.85
3:1	20.5	0.9	0.5	-
1:1	25.3	1.3	1.0	-
1:3	23.8	1.0	0.6	-
1:9	23.8	1.3	0.7	-
PDIR-CN$_2$	20.3	1.4	0.8	17.12
PHJ	42.9	3.2	1.8	16.85/17.12
SL	37.9	1.4	0.8	17.17

Since PDIR-CN$_2$ is less ordered than DIP thicker films (d = 100 nm for the pristine PDIR-CN$_2$ and 1:1) were used in order to obtain better diffraction pattern. All reflections in the PDIR-CN$_2$ spectrum at q_{xy}-values exceeding 0.76 Å^{-1} can be assigned to the reported crystal structure [178]. However, the peaks at $q_{xy} \approx 0.30$ and 0.63 Å^{-1} originate neither from the RT-phase unit cell nor from the HT-phase one and stem presumably from a different orientation as PDIR-CN$_2$*. Additional peaks are found in the equimolar mixed film at q_{xy} equal to 0.92 Å^{-1} and to 1.81 Å^{-1}. Since these two new reflections do not originate from the structures of the pure components they are assigned to a new mixed phase polymorph. This observation indicates that the mixture is not completely random in the in-plane direction, but has a preferred ordering, comparable to a co-crystal [80,213]. The corresponding coherent island size evaluated from the FWHM l_s equals 3.5 nm which is by factor of 5 smaller than l_s in pristine films (18.8 nm for DIP and 18.4 nm for PDIR-CN$_2$). In the blends with exceeding acceptor content the pure PDIR-CN$_2$* is more pronounced showing phase separation from the mixed phase, whereas in the 3:1 film weak phase separation between DIP and the mixed phase occurs.

Since PDIR-CN$_2$ molecules (~22.0 Å) are longer than DIP molecules (~18.4 Å) and because in a co-crystal the axes of the π-conjugated cores should be parallel in the unit cell, the increase of the out-of-plane lattice spacing $d_{(001)}$ in blends is explained by a change of the PDIR-CN$_2$ molecular tilt angle. The orientational changes of both compounds can be quantified by NEXAFS spectroscopy, which probes the average backbone orientation. To unambiguously identify the molecular arrangement at the interface, the XRD measurements were complimented with NEXAFS spectroscopy at the C1s edge, performed and evaluated by Paul Beyer (University of Berlin). The resulting absorption spectra are shown in Figure 6.3, Figure 6.4 and Figure 6.5. Pristine DIP on SiO$_2$, Figure 6.3a, shows clear dichroic behavior. After integration from 283.3 to 286.3 eV and angular analysis of

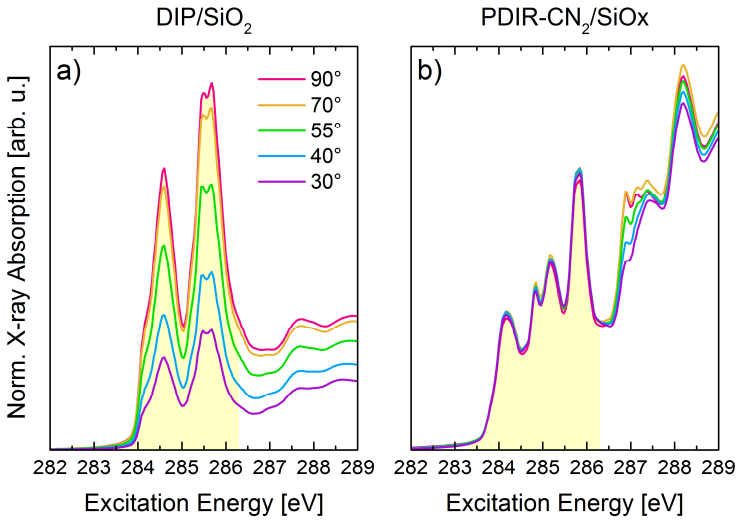


Figure 6.3. X-ray absorption spectra for varying angles of incidence θ between the photon beam and the sample surface. The shaded area depicts the region used for obtaining the integrated peak intensities. Here, the results on amorphous SiO_2 substrates are shown for DIP (a) and PDIR-CN_2 (b). All spectra are normalized to the incident photon flux and to the C1s step edge at 270 and 330 eV. The images are taken from [2].

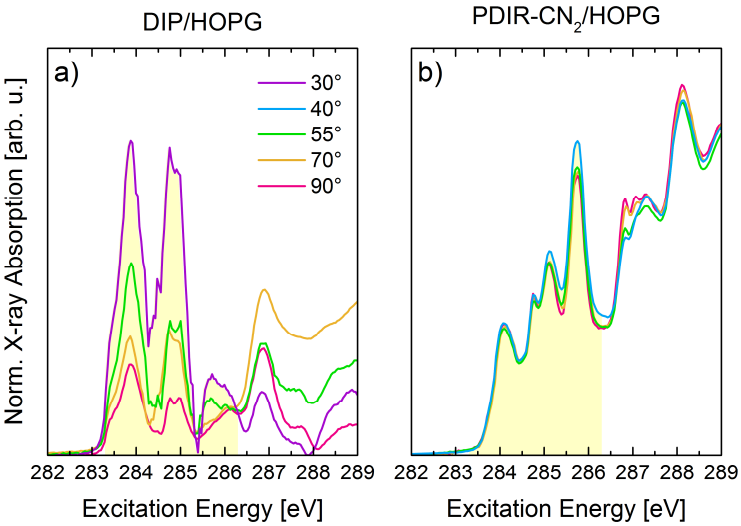


Figure 6.4. X-ray absorption spectra for varying angles of incidence between the photon beam and the sample surface. The shaded area depicts the region used for obtaining the integrated peak intensities. Here, the results of DIP (a) and PDIR-CN_2 (b) on HOPG substrates are shown. Substrate contributions from the HOPG substrate were subtracted. All spectra are normalized to the incident photon flux and to the C1s step edge at 270 and 330 eV. The images are taken from [2].

the obtained π^*-peak intensities using Equation (3.7), an average molecular inclination angle of 78±5° between molecular and substrate surface plane is obtained [214]. On HOPG, the reverse dichroism is clearly observed (Figure 6.4a). After subtraction of the C1s substrate signature [215], analysis here yields an average molecular inclination angle of 33±5°. Since the carbon frame of the DIP molecules features a perfect lattice match to the

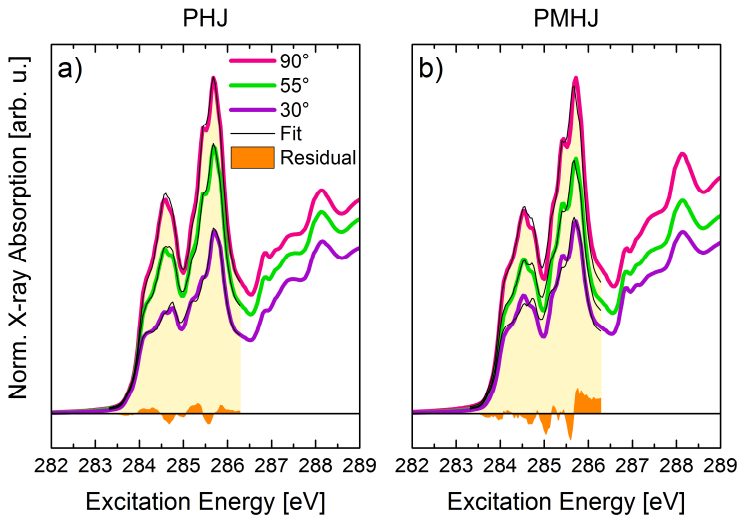


Figure 6.5. X-ray absorption spectra for device relevant architectures, PHJ (a) and PMHJ (b), of DIP and PDIR-CN$_2$ on SiO$_2$. The thin black lines show linear combinations of pristine DIP and PDIR-CN$_2$ spectra at θ = 55°, providing the best fit to the experimental data. The orange curve is the residual for the deconvolution at θ = 90°. For visual clarity, the absorption spectra for θ = 70° and 40° are not shown. The images are taken from [2].

HOPG surface, this dichroism is readily explained by the templating function of the HOPG to induce a new polymorph, consisting of lying down DIP molecules. Deviations from 0° for perfectly flat lying down molecules originate from defects on the substrate surface, as well as the averaging nature of the NEXAFS technique itself, being sensitive to both, crystalline (well-ordered) and amorphous (disordered) regions. This shows that the choice of HOPG and SiO$_2$ as substrates is ideal to control the molecular orientation of the DIP molecules, which is essential to control the orbital overlap at (organic-organic) interfaces.

Likewise, the X-ray absorption spectra of pristine PDIR-CN$_2$ on HOPG and SiO$_2$ are shown in Figure 6.3b and Figure 6.4b. In contrast to DIP, there is no clear dichroism visible, independent of the substrate choice. The results of the peak intensity evaluation are shown in Figure 6.6. On SiO$_2$ an average inclination angle of 55±5° is obtained, compared to 53±5° on HOPG. However, since different IEs on both substrates were observed (Section 6.2), the molecular arrangements appear to be different. The templating function of the HOPG is reduced by the alkyl side chains of the PDIR-CN$_2$ molecules. On weakly interacting SiO$_2$, on the other hand, the undisturbed, known crystal phase with an average inclination angle of 53° [178] is adopted almost exclusively.

Looking at the X-ray absorption spectra of device relevant architectures in Figure 6.5a (PHJ) and b (PMHJ), one can identify features from both pristine components. Deconvoluting the mixed spectra with pristine spectra obtained at θ = 55° reproduces all major features. The best fits are shown by thin black lines in Figure 6.5. Angular analysis of the individual components isolates the separate orientations for DIP and PDIR-CN$_2$ molecules (Figure 6.7). The DIP molecules at the planar interface possess an average inclination angle of 79±5°, decreasing slightly at the mixed interface to 76±5°. For the PDIR-CN$_2$ contribution, the inverse trend is observed – a slight increase from 53±5° to

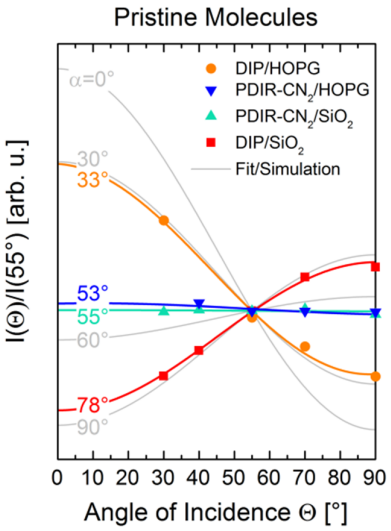


Figure 6.6. Evaluation of the dichroism (C1s-π^* transition) for pristine molecular thin films of DIP and PDIR-CN_2 on substrates SiO_2 and HOPG. The specified angles α on the left are the average inclination angle between molecular and substrate surface plane for each fitted/simulated dichroism curve. The C1s substrate signatures were subtracted prior to the analysis. All curves are normalized to an incident angle of 55° to eliminate the constant of proportionality introduced in Equation 3.7. The image is taken from [2].

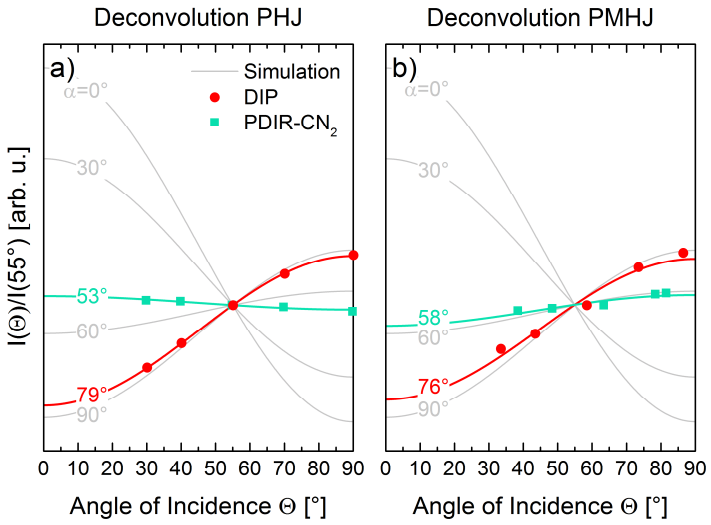


Figure 6.7. Evaluation of the π^*-dichroism for the pristine molecular contributions in the device relevant architectures – PHJ (a) and PMHJ (b). The specified angles α on the left are the average inclination angle between molecular and substrate surface plane for each fitted/simulated dichroism curve. The C1s substrate signatures were subtracted prior to the analysis. All curves are normalized to an incident angle of 55° to eliminate the constant of proportionality introduced in Equation 3.7. The image is taken from [2].

58±5°. This shows that the average orientation of both individual molecules in the planar configuration is nearly unperturbed compared to the pristine molecular films in the known crystal bulk structures. However, in the mixed film, where the interplay between donor and acceptor is much more pronounced, an angular shift towards a common alignment is

achieved. This points towards a relaxation or segregation from the individual polymorphs to a new one, which was also seen in the GIXD data. The observed shift of at most 5° here is not astoundingly large. However, since NEXAFS determines only average orientations over all probed molecules, a much larger angular shift (>15°) due to relaxation in the new polymorph is most likely, while the individual pristine crystalline phases of DIP and PDIR-CN$_2$ coexist as well to some degree.

As mentioned before, no new features due to interaction are observed. This is shown in Figure 6.5 by the small residuals. There are several explanations for this distinction, for example forbidden dipole transitions, the weak interaction character of the ground state CT complex itself or just surface effects [50,216–221]. IR spectroscopy was performed in transmission mode, being sensitive to properties of the complete bulk (Section 6.2). NEXAFS sensitivity, on the other hand, is limited by the inelastic mean free path of the excited electrons (~1 nm) and the absorption depth of the incident X-ray photons, meaning that only surface properties are measured [222]. The weak interaction strength points towards a small overlap in the ground state between both involved molecules, possibly too weak to be easily detected by the used setup. Additionally, the formed exciton upon optical or X-ray absorption involves different molecular orbitals. This results in the observed additional features for optical absorption (Section 6.4), which are absent compared to X-ray absorption.

6.2 Ground State Properties

Having shown that both compounds are well intermixed and hence the intermolecular electronic interaction is not inhibited by phase separation, spectroscopic methods for its characterization were applied. Using infrared-absorption spectroscopy, it is possible to assign a shift of intramolecular vibration frequencies to the degree of charge transfer between donor and acceptor in the absence of electronic excitation, i.e. in the electronic ground state. In particular, the stretching mode of the nitrile group ($-C \equiv N$) present in PDIR-CN$_2$ molecules is highly sensitive to CT [223].

Figure 6.8 shows a comparison between experimental IR spectra of pristine DIP and PDIR-CN$_2$, co-evaporated equimolar DIP:PDIR-CN$_2$ films, calculated spectra of neutral PDIR-CN$_2$ in the gas phase and of its radical anion. In the presented spectral range DIP does not reveal any IR active vibration modes, which makes the CN-mode ideal for comparison. The CN-stretching mode appears at ~2222 cm^{-1} (all peak positions are determined by using Gaussian fit) in IR spectra of the pristine PDIR-CN$_2$ film. Based on our calculations, the CN-stretching mode of the PDIR-CN$_2$ radical anion reveals a red-shift of 26±2 cm^{-1} towards 2196 cm^{-1}. In the measured IR spectrum of the equimolar DIP:PDIR-CN$_2$ mixture one can observe a red-shift of the CN-mode peak of 4.5±1 cm^{-1} (the instrumental resolution is 1 cm^{-1}). Assuming a linear correlation between charge transfer δ and the frequency shift of the CN-mode [224], one can estimate that in the DIP:PDIR-CN$_2$ system a partial charge transfer of about 0.17±0.04 electrons occurs. This degree of interaction should be considered as non-negligible for the ground state, since it is comparable to other values for small-molecule CT complexes, e.g. 0.3 for

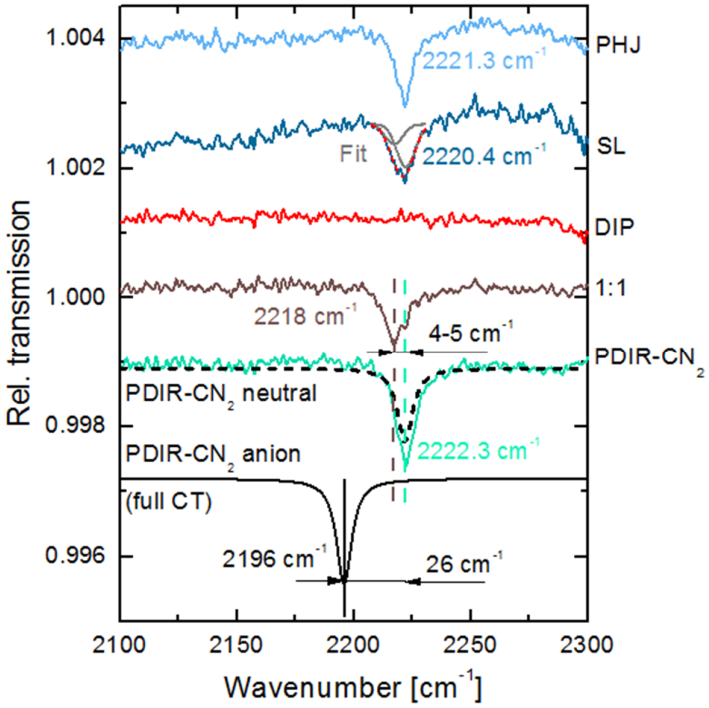


Figure 6.8. Infrared transmission of pristine DIP, PDIR-CN_2, equimolar mixture, heterostructures on silicon and calculated spectra of neutral and ionized PDIR-CN_2 in gas phase. The spectra are vertically shifted for clarity. Peak positions are taken from Gaussian fit.

TMP(tetramethoxypyrene):TCNQ with ΔE_{DA} = 1-1.5 eV [225] or 0.12 for TMP:F_4-TCNQ with ΔE_{DA} = 0.6-1.1 eV [226]. For the PHJ sample no shift is observed. In case of the superlattice the peak red-shifted by 2 cm^{-1} can be fitted with two Gaussians (Figure 6.8, dark blue curve), one unchanged and one shifted as in the blend, showing smaller amount of interacting molecules.

Ultraviolet photoelectron spectroscopy (UPS) was used to determine the HOMO level and the work function of the crystalline molecular films. Through this method, one also gain access to the ionization energies (IE) of the molecules in the layers. The data are provided by Paul Beyer and Andreas Opitz (University of Berlin). Valence band spectra for pristine DIP and PDIR-CN_2 thin films are shown in Figure 6.9. All energy values are derived from the peak onsets, calculated by linear extrapolation of the inflection point to the base line.

Due to the high degree of structural compatibility between DIP and the HOPG surface, the resulting templating effect forces the adsorbed molecules to grow in a mainly lying down fashion. On weakly interacting, amorphous surfaces, like SiO_2 or HIL 1.3 coated ITO, on the other hand, no such templating exists and the molecules grow rather upright standing. This large orientational difference conforms well to the lower IE (5.4 eV) for upright standing than for lying down (5.8 eV) DIP molecules [227]. According to the NEXAFS results (Section 6.1) PDIR-CN_2 does not experience strong interaction with the HOPG substrate since no significant orientational change was found (Figure 6.6). Nevertheless, one can observe the IE shift by 0.3 eV from 7.1 eV on SiO_2 to 6.8 eV on HOPG

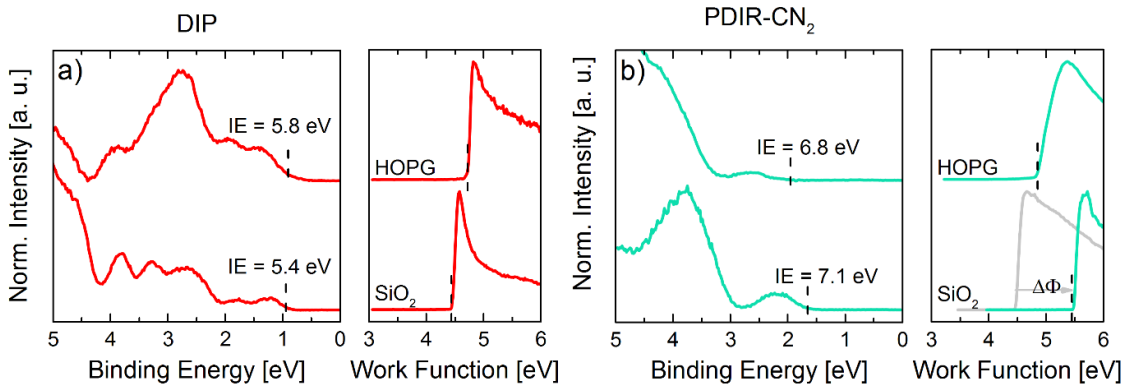


Figure 6.9. Valence region spectra and work functions of pristine (a) DIP and (b) PDIR-CN_2 thin films on amorphous SiO_2 (bottom) and HOPG substrates (top). The substrate contributions have been subtracted from the measured signal, in order to obtain the true molecular valence signatures. Dashed lines give the position of the HOMO and work function onsets, as determined by linear extrapolation of the inflection point to the baseline. The gray spectrum shows the work function of the uncovered SiO_2 substrate. $\Delta\Phi$ shows the work function shift and thus LUMO pinning of pristine PDIR-CN_2 films. All spectra are vertically scaled and shifted for clarity. The images are taken from [2].

(Figure 6.9b). LUMO level pinning is observed from the increase of work function upon deposition of PDIR-CN_2 on SiO_2 (grey arrow in Figure 6.9b) [228,229]. By assuming a position of the pinned LUMO level of about -0.4 eV, the transport gap is 2.65 eV [214,230]. This obtained transport gap is nearly identical to the one of DIP with 2.60 eV [154], which is readily explained by the similarity of the π-conjugated cores and the optical gaps of both molecules. This also matches with the measured transport gap of other perylene derivatives [231].

After the establishment of energy values of the pristine molecules, the energetic interplay at planar and mixed DIP/PDIR-CN_2 (D/A) interfaces is discussed. ITO/HIL 1.3 and HOPG substrates were used to build a base layer consisting of standing and lying DIP molecules, respectively. The results are shown in Figure 6.10.

Looking at the PHJ architecture on ITO/HIL 1.3, shown in Figure 6.10a, first one observe Fermi-level pinning of DIP on HIL 1.3, as shown before [149]. Upon subsequent deposition of PDIR-CN_2 on standing DIP molecules, vacuum level alignment between PDIR-CN_2 and DIP is observed. The IE values for PDIR-CN_2 deposited on top of SiO_2 and on standing DIP molecules differ by ~0.35 eV. Taking the HOMO-level offset of 1.35 eV and a transport gap for PDIR-CN_2 of 2.65 eV, the energy gap ΔE_{DA} is about 1.3 eV. Changing the substrate to HOPG results in a higher IE and vacuum level alignment of DIP to the substrate. The same is true for the deposition of PDIR-CN_2 on top, however, the IE changes only marginally (6.65 eV compared to 6.75 eV on standing DIP molecules), since the side groups of PDIR-CN_2 inhibit close stacking to the DIP molecules.

To look at large-area D/A interfaces evaporated blends of DIP and PDIR-CN_2 were evaporated on top of DIP pre-covered ITO/HIL 1.3 and HOPG substrates. The blended film of DIP and PDIR-CN_2 was evaporated on top of DIP pre-covered ITO/HIL 1.3 substrates (Figure 6.10c) and one observe a slight shift of the vacuum level, which is also

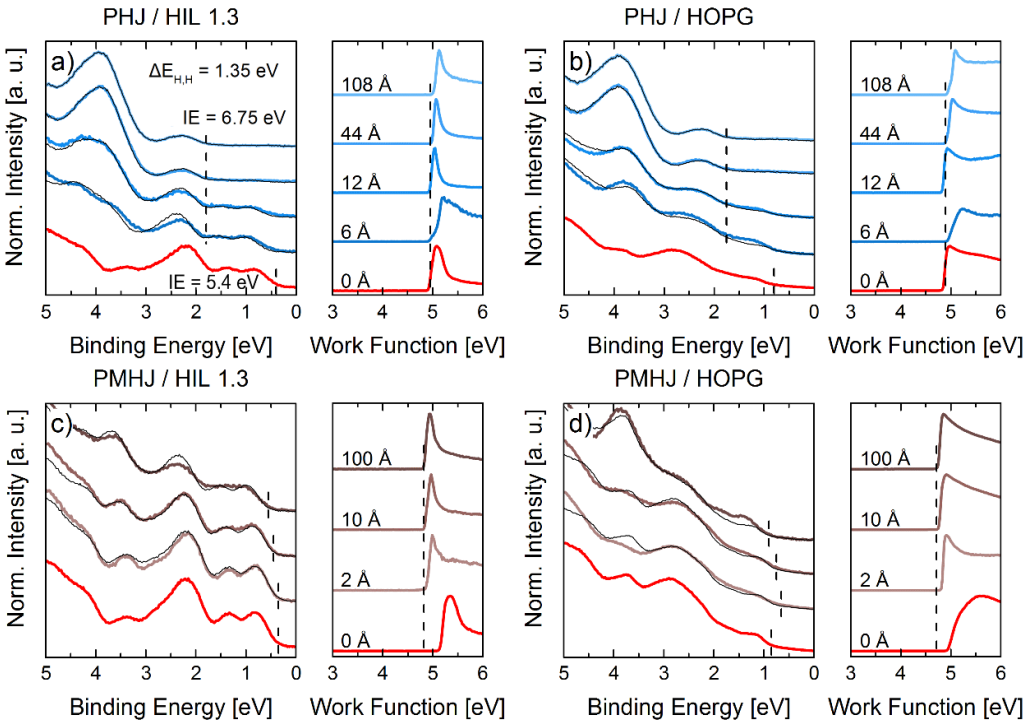


Figure 6.10. Valence region spectra and work functions (WF) of PHJ (a) on HIL 1.3 and (b) HOPG for increasing layer thicknesses, indicated by the inset values in the WF plots. The red graphs show the base line spectra of DIP covered substrates. Parts (c) and (d) show the analogous results of PMHJ architectures. All spectra are vertically scaled and shifted for clarity. Overlaid in the valence region spectra are fits with pristine valence signatures for all thicknesses in thin black curves. The images are taken from [2].

reported for several other systems[232,233]. The HOMO onsets of the components were extracted from the deconvolution of the measured signal from the 100 Å thick molecular blend (vertical dashed lines, Figure 6.11). The fit is a linear combination of two unaltered spectra from the pristine components and describes the measured spectrum well. In addition, the energetic positions of the single fit components were kept fixed (green and red vertical lines) and a convolution with a Gaussian distribution (FWHM = 0.40 eV) was applied to account for spectral broadening due to increasing disorder in the mixed films as seen by X-ray scattering and AFM measurements. The disorder, along with the low sensitivity of the UPS setup itself, would explain the absence of new features for the weak CT complex here. At the planar mixed interface ΔE_{DA} amounts to 1.65 eV, a further increase compared to the PHJ. The effect of IE shift by intermixing was shown previously, e.g., in references [234,235].

The HOMO level offset differs for the PHJ ($\Delta E_{\mathrm{H,H}}^{\mathrm{PHJ}}$ = 1.35 eV) and the PMHJ ($\Delta E_{\mathrm{H,H}}^{\mathrm{PMHJ}}$ = 1.00 eV) device architectures. This is related to differences of the energy levels in the two structures. Morphological changes, such as disorder and molecular reorientation, as well as mixing affect the electrostatic field at the thin film surface and the coupling between the molecules [177,233–236]. Additionally, one can note that a partial GS-CT shifts the HOMO levels as a whole but does not introduce a new feature in the UPS data. This finding

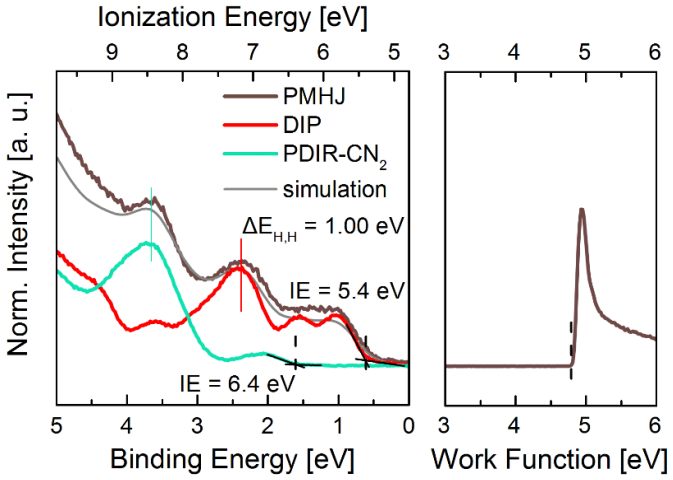


Figure 6.11. Deconvolution of the valence band with pristine valence signatures for a 100 Å thick film in PMHJ geometry. The green and red vertical lines are used to align the single fit components. The images are taken from [2].

contrasts with a HOMO level offset between DIP and PDIR-CN_2 of 1.70 eV (which would give a smaller ΔE_{DA} of only 0.95 eV), being expected from vacuum level alignment using the IEs for the pristine films.

The results on the PMHJ on HOPG show the same trend as on ITO/HIL 1.3 and are shown in Figure 6.10d. In comparison to the energy levels of the pristine molecules, this strongly indicates a mixture containing upright-standing DIP molecules, breaking the templating effect of the HOPG substrate. One can note further that a clear trend in IE of films dependent on molecular orientation as observed for other materials before [154,177,236] is absent for PDIR-CN_2.

6.3 Excited State Properties

Having confirmed the presence of CT in the electronic ground state, a way in which CT plays a role upon excitation is studied. Absorption spectra, taken by UV/Vis/NIR spectroscopy, are shown in Figure 6.12a-c. Crystalline thin films of DIP and PDIR-CN_2 reveal anisotropic optical properties due to the transition dipole moment of the lowest electronic transition being oriented along the long molecular axis [109]. Since the inclination angle of PDIR-CN_2 is smaller (~53°) compared to DIP (~83°), its absorption strength is, accordingly, higher in the in-plane direction (parallel to the substrate surface). The orientations of the transition dipole moments of individual molecules are depicted in Figure 4.1a and 4.4a. The positions of the energetically lowest peaks give the optical gap ΔE_{opt} of 2.25 eV for pristine DIP and 2.17 eV for pristine PDIR-CN_2. Compared with the transport gaps given above, 2.60 and 2.65 eV respectively, an exciton binding energy of 0.4-0.5 eV can be derived.

Considering the spectrum of an equimolar blend one can observe several features, which can only be explained by taking into account the excited state interaction between the two different compounds (see also the calculated superposition of the two pristine components,

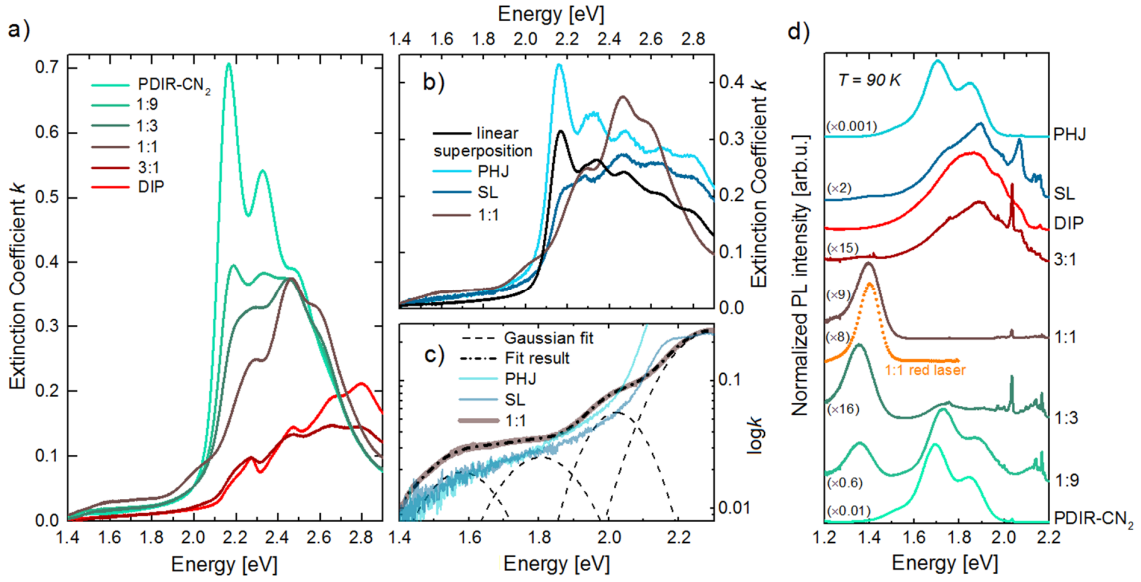


Figure 6.12. Absorption spectra for different mixing ratios (a) and heterostructures in comparison to the superposition of spectra from the pristine components (b), (c) low energy range plotted in logarithmic scale along the vertical axis with the CT absorption band decomposed into Gaussians for the results of the 1:1 film. (d) Low temperature photoluminescence spectra recorded at 90 K.

black curve in Figure 6.12b). As can be seen from Figure 6.12a, even a low concentration of DIP causes a rapid decrease in intensity of the lowest PDIR-CN_2 peak at 2.17 eV (1:9 and 1:3). The intensity decrease of this transition in PDIR-CN_2 originates probably in the disturbed structural long-range order. Similarly, the DIP spectrum is influenced by intermixing with PDIR-CN_2 (3:1) as can be observed by the decrease of the peak intensity at 2.8 eV [143].

As mentioned in the introduction the observation of CT states in optical absorption spectra often requires more sensitive techniques[237–242] due to the low cross section. However, the spectrum of the equimolar mixed film (1:1) clearly reveals a broad band at photon energies below the optical gaps of the pristine materials (1.4-2.1 eV, Figure 6.12c), which originates from direct excitation of CT states [218,243–246]. This subgap band, which is related to charge transfer interaction [44,50,52,247], was fitted using three Gaussian functions with peak positions at 1.58, 1.81 and 2.02 eV (FWHM 0.25, 0.27, 0.20 eV). Together with a fourth Gaussian for the fundamental transition across the gap, the absorption spectrum in Figure 6.12c can be fitted over the whole measured range. Reasons for the observed splitting of the CT states may be variation in the unit cell or vibronic contributions. In contrast to the intermixed films, absorption spectra of PHJ and a superlattice (Figure 6.12b) are similar to a linear superposition of the spectra of the pristine materials and a substantial contribution from CT states is absent.

Figure 6.12d shows photoluminescence spectra of single-component films and blended films with different mixing ratios recorded at low temperature (90 K) using an excitation energy of 2.33 eV. The DIP spectrum is in agreement with the literature [248,249].

PDIR-CN_2 reveals very strong emission intensities with two maxima at 1.69 and 1.84 eV at low temperature.

Upon mixing, the emission intensity sharply decreases and completely disappears in the equimolar blend within the range that of the pristine component. Moreover, one can observe a new peak emerging around 1.4 eV that reveals a slight red-shift and intensity rise with increasing PDIR-CN_2 fraction. One can assign this new emission band to radiative recombination processes from the charge-transfer state between DIP and PDIR-CN_2 molecules [64,66,245,250]. In the equimolar blend local exciton emission from the pristine compounds is almost quenched, which is consistent with a fully intermixed film. The similar effect was observed at low temperatures for other materials[213,251]. In addition, non-radiative recombination contributes much more strongly to the energy loss compared to the pristine materials since the PL intensity observed in the 1:1 film is one order of magnitude weaker than in pristine DIP and three orders weaker than in pristine PDIR-CN_2. Using a red laser with an excitation energy of 1.96 eV, which is below the bandgap of the neat materials, the CT state can be excited directly, avoiding transfer from the higher energy molecular excitons (Figure 6.12d) [245].

Regarding the layered samples, the PHJ exhibits strong emission especially at low temperatures mainly by PDIR-CN_2 excitonic recombination. As expected, emission from the SL contains features of both components and only weak emission features from the CT states can be observed at 1.4 eV.

The recombination process through the CT state is further confirmed by time-resolved photoluminescence (TRPL) studies performed by Marina Gerhard (University of Marburg). The TRPL data presented in Figure 6.13 indicate that the strong long-lived emission of the singlet population of pristine DIP and PDIR-CN_2 at 10 K is quenched due to charge transfer at donor/acceptor interfaces and thus decays on a shorter time scale of picoseconds in the mixed films. In addition, one can observe clearly defined CT emission with a rise time shorter than the instrument response time (~15 ps), indicating that most of the CT states are actually populated on this time scale. The recorded PL dynamics in blends is thus dominated by CT emission. The effective $1/e$ decay times are shown in Table 6.2. The sub-nanosecond range has been typically observed for CT emission decay [252,253]. For the blends with excess PDIR-CN_2, the CT state dynamics are not substantially altered when the temperature is varied between 10 and 290 K and show clear mono-exponential decays (Figure B.3) with no evidence for side decay processes such as singlet exciton dissociation expected to occur in the shorter time range [88,253]. In the case of the 1:1 blend, however, the PL decay becomes faster with increasing temperature, indicating the presence of a thermally activated quenching mechanism. Such quenching could be either due to thermally activated dissociation of CT states, or emerge from the presence of non-radiative recombination centers. However, thermally activated CT dissociation would require binding energies on the order of k_BT which is much smaller than a value of 0.2 eV evaluated in the following (see Section 6.5), whereas the hypothesis of non-radiative recombination centers would imply a certain mobility of CT states with a temperature-dependent diffusion coefficient [254].

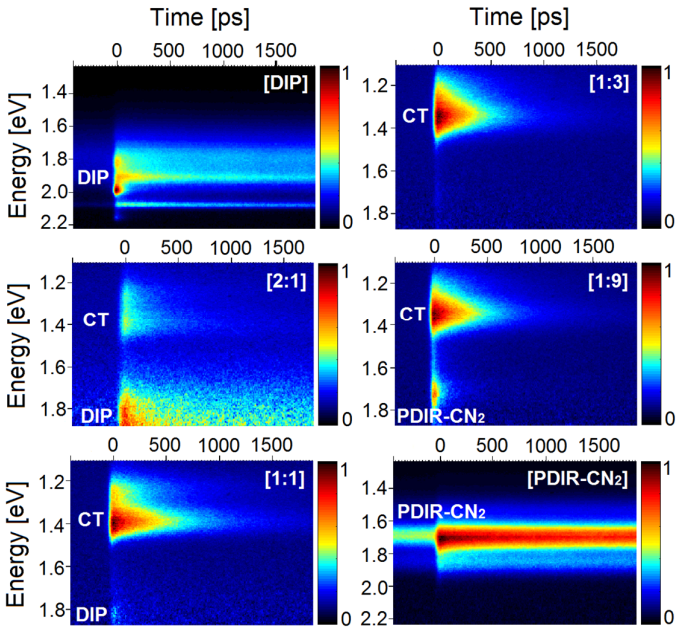


Figure 6.13. Two-dimensional plots of the spectrally and time-resolved PL signatures at 10 K for DIP:PDIR-CN2 blends with varying mixing ratios, as labelled. The PL intensity is normalized to unity for each image. Weak signatures of DIP and PDIR-CN2 are observed in the blends, beside the more dominant and long-lived CT peak. At low temperatures there is a pre-edge emission at negative delay times in the pristine films due to long life time (> 12.5 ns). The images are taken from [2].

Table 6.2. Effective decay times extracted from mono-exponential fits of PL transients recorded at low and room temperatures

Material	τ at 10 K	τ at 290 K
DIP	> 12.5 ns	257 ps
2:1	190 ps	182 ps
1:1	496 ps	342 ps
1:3	448 ps	418 ps
1:9	452 ps	433 ps
PDIR-CN2	> 12.5 ns	151 ps

From the comparison of intermixed and layered samples, where the CT signatures are only weakly present, one can assume an anisotropic character of the CT transitions polarized in the in-plane direction. In order to explore the anisotropy in detail variable angle spectroscopic ellipsometry (VASE) [255] was performed on a film with the most pronounced CT effect, i.e. 1:1 (ellipsometry data for the other mixing ratios are given in Appendix, Figure B.4). The in-plane and out-of-plane components of the extinction coefficient are presented in Figure 6.14. The CT band between 1.5 – 2.1 eV is only visible in the in-plane direction, i.e. the direction of π-π interaction. This result is consistent with the absence of the CT transition in the PHJ and the SL, where no significant π-π stacking

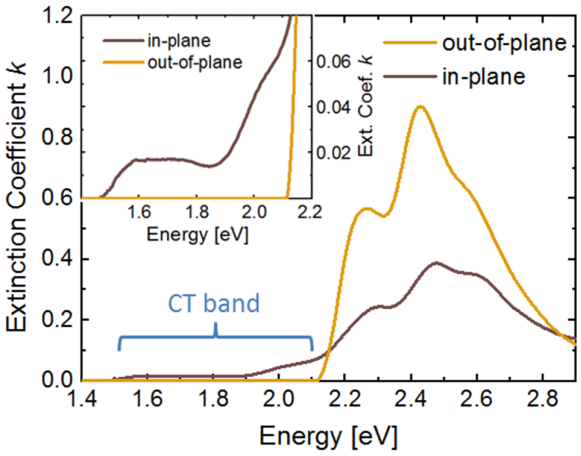


Figure 6.14. Anisotropic components of the extinction coefficient *k* of the 1:1 film. The inset shows a zoom into the range of 1.4-2.2 eV. The in-plane component corresponds to the absorption data in Figure 6.12.

of both compounds is present and it is also in agreement with CT transitions in other compounds [256].

To complete the optical characterization by absorption and photoluminescence spectra, electroluminescence (EL) and incident-photon-to-current efficiency (IPCE) spectra of solar cells were measured as well. The measurements were carried out by Eduard Meister and Theresa Linderl (University of Augsburg). Recorded IPCE spectra (see Figure 6.15) display significant differences between PHJ and PMHJ cell architectures. Note that while the IPCE data in the subgap region (<2 eV) correlate very well with the absorption spectra of the 1:1 blend and the PDIR-CN_2/DIP bilayer displayed in Figure 6.12b,c, there is a distinct difference in the spectral range above the gap (2-3 eV). In this spectral region the PHJ device exhibits a two- to threefold higher photocurrent as compared to the PMHJ device. The lower current of the latter cannot be fully explained by the lower absorptivity of the blend with respect to the bilayer structure (see Figure 6.12b), which is due to a less favorable molecular orientation for light absorption. Instead, the lower current indicates that the PMHJ suffers from a charge transport problem due to the intimate intermixing of DIP and PDIR-CN_2 in the 1:1 blend. Because of the good miscibility of both components, there are no separate percolation paths for the extraction of the generated charge carrier pairs, which are trapped and subsequently recombine in the mixed phase (see also the discussion on charge transport in Section 6.4 and Ref. [257]). However, even in the PHJ device the IPCE stays below 10%, mainly because of insufficient light absorption due to the predominantly standing orientation of both molecular species.

In the logarithmic representation, Figure 6.15 shows EL spectra of a PMHJ device that was operated as a light-emitting diode (LED) under forward bias of 3 V. The luminescence signal was normalized to the maximum at about 1.35 eV, which corresponds well to the CT emission band observed in photoluminescence spectra of blends (see Figure 6.12d). In addition, there is a much weaker band at about 1.8 eV, which could stem from luminescence of one of the pristine materials. For the PHJ device there was no detectable EL emission in

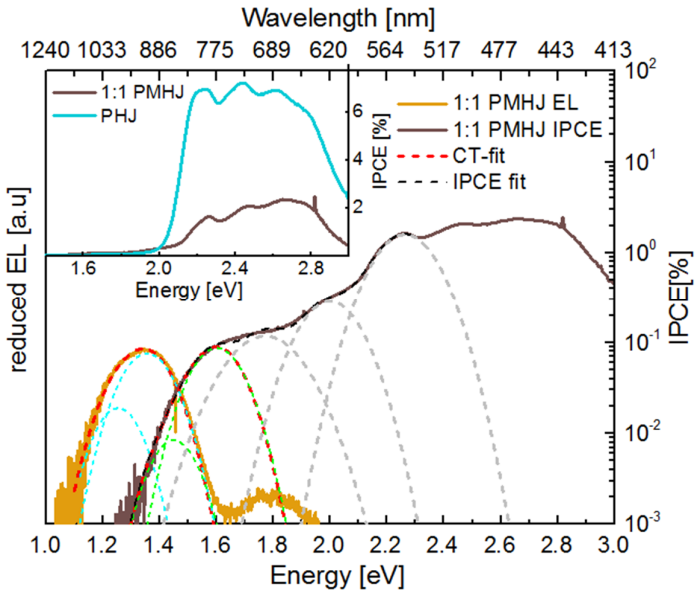


Figure 6.15. The orange curve represents the reduced EL spectrum of the 1:1 PMHJ sample measured at 3 V bias voltage. The brown line shows the IPCE spectrum of the 1:1 PMHJ solar cell. The red dashed lines show the superposition of Gaussians corresponding to the CT-fit, light-blue and light-green for EL- and IPCE-fit, respectively. The grey dashed lines complete the light-green Gaussians to the IPCE-fit over the whole CT range (black dashed line). Note that the peak at 2.25 eV belongs to the pristine material. The inset displays linear scaled IPCE measurements of PHJ and PMHJ cells. The sharp peak around 2.8 eV (IPCE of PMHJ cell) is a measurement artifact. All spectra were recorded at 297 K. The images are taken from [2].

the calibrated wavelength range (300-1000 nm), even at a voltage as high as 4.5 V, where the devices are close to failure. In contrast to the PL spectra shown in Figure 6.12d, emission from the pristine materials cannot be seen in a PHJ, which indicates that nearly all injected electron-hole pairs recombine at the *D*/*A* interface. However, the radiative efficiency of emission from CT states polarized in the out-of-plane direction seems to be extremely small.

As introduced by Tvingstedt *et al.* [240] and refined by Vandewal *et al.* [48], EL and IPCE spectra can be analyzed in the framework of Marcus theory to estimate the CT energy E_{CT}, which can then be discussed in relation to the open-circuit voltage V_{OC} of the solar cells to quantify energy losses [258,259]. As the EL data show an asymmetric peak, the CT approach was modified and fitted our data with the sum of two Gaussians (CT-fit, see Figure 6.15). Both the reduced absorption $\sum_{i=1}^{2} \sigma_i(E)E$ and the reduced emission $\sum_{i=1}^{2} I_{f,i}(E)E^{-1}$ were fitted with

$$\left.\begin{matrix}\sum_{i=1}^{2}\sigma_i(E)E \\ \sum_{i=1}^{2}I_{f,i}(E)E^{-1}\end{matrix}\right\} = \sum_{i=1}^{2}\frac{f_{\sigma_i,I_{f,i}}}{\sqrt{4\pi\lambda_{0,i}k_BT}}\,exp\left(\frac{-(E_{CT,i}\pm\lambda_{0,i}-E)^2}{4\lambda_{0,i}k_BT}\right). \quad (6.1)$$

Here, λ_0 represents the reorganization energy related to the Stokes shift in the CT manifold. f_σ and f_{I_f} are proportional to the square of the electronic coupling matrix element. The plus and the minus sign are taken for reduced absorption and reduced emission, respectively. Consequently, one obtains two different CT energies: E_{CT1} = 1.35 eV and

E_{CT2} = 1.48 eV, with the latter value stemming from the peak with the stronger spectral weight. This energy splitting may stem from structural variations or a vibronic progression.

In order to confirm the superposition of different CT states included in the absorption band, the IPCE spectra (as in Figure 6.12c) were fitted with the sum of Gaussians as shown in Figure 6.15 on the right axis. Although the absorption CT band consists of at least four distinct states, obviously only two of them lead to radiative recombination. Similar behavior has been observed in the literature for systems with a spectrally broad manifold of CT states [260,261]. However, while this can be seen as evidence for energetic relaxation in the CT density of states, there still remains the question if equilibrium is reached within the lifetime of carriers. Further investigations will have to clarify this issue.

6.4 Device Behavior

To elucidate the mechanisms of charge separation and transport, (photo)-electrical measurements were performed in the group of Prof. Wolfgang Brütting (University of Augsburg) by Eduard Meister for solar cells built in different device architectures, PHJ and PMHJ (1:1). This allows for a direct comparison of the photocurrent and the open-circuit voltage between face-to-face (in-plane) and edge-on-edge (out-of-plane) stacking.

The solar cell architecture can be seen in Figure 6.16 alongside the *j-V* characteristics of PHJ and PMHJ solar cells in dark (dashed lines) and under one sun simulated AM1.5G illumination (solid lines). The solar cell parameters extracted from *j-V* measurements are collected in Table 6.3. Note that the open circuit voltage (V_{OC}) of both architectures is equal and amounts to 0.50 V, whereas the short circuit current (j_{sc}) changes significantly from -0.65 mA/cm² for the PHJ to -0.24 mA/cm² for the PMHJ cell, which correlates very well with IPCE results. The fill factor (FF) decreases from 57 % (PHJ) to 40 % (PMHJ). As a result, the efficiency η is reduced from 0.18 % for the PHJ to 0.05 % for the PMHJ cell, which contrasts with phase separating mixtures, where PMHJ cells provide higher

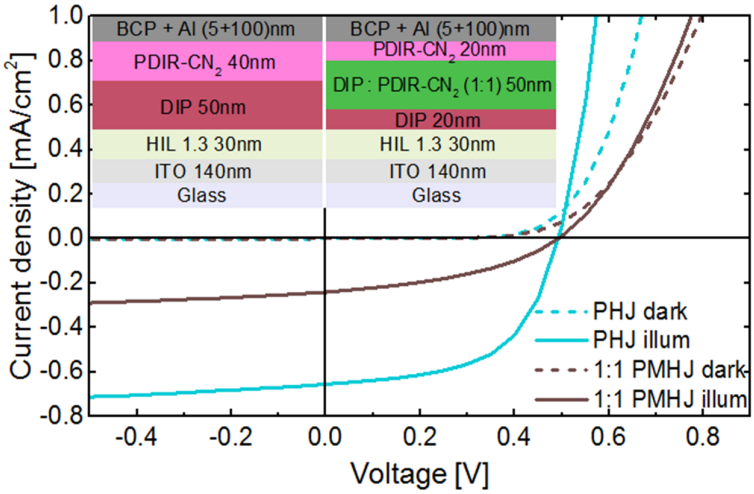


Figure 6.16. *j-V* diagram of PHJ and PMHJ DIP/PDIR-CN$_2$ based solar cells. Dashed lines represent measurements in the dark and the solid lines under illumination. The inset shows the stack architecture of the PHJ (left) and PMHJ (right) solar cells. The images are taken from [2].

efficiencies than their PHJ counterparts[149]. Thus, some degree of phase separation, as opposed to perfect intermixing, is beneficial for charge separation in order to increase the device performance.

In general, the open circuit voltage of an organic molecular D/A solar cell can be written as [258,259]

$$V_{\mathrm{OC}}(T) = \frac{E_{\mathrm{CT}}}{q} - \Delta V_{\mathrm{OC}}, \tag{6.2}$$

where q is the elementary charge and E_{CT} sets the upper limit of V_{OC}, which can be achieved only in the low temperature limit. At finite temperature there is an energy loss $q\Delta V_{\mathrm{OC}} = = \Delta V_{\mathrm{OC}}^{\mathrm{rad}} + q\Delta V_{\mathrm{OC}}^{\mathrm{nonrad}}$ composed of thermodynamically inevitable radiative losses as well as non-radiative losses. For a wide range of organic D/A systems the energy loss between E_{CT} and the V_{OC} at 300 K is in the range of 0.5 – 0.6 eV [86,257]. In our case, from E_{CT2} = 1.48 eV for the dominant optically detected CT state one obtains an energy loss of $q\Delta V_{oc}$ of about 1 eV, significantly larger than the typically observed range.

Furthermore, the photovoltaic gap ΔE_{DA} from UPS is an additional measure for the V_{oc} limit in solar cells and was used before to estimate losses in V_{oc} in PHJ solar cells [8]. For the planar heterojunction of DIP/PDIR-CN$_2$ ΔE_{DA} is 1.3 eV. Therefore, the losses for the open circuit voltage regarding the energy level offset amount to ~0.8 V, larger than for previously analyzed material combinations [8]. As discussed in the previous section, the reason for the high energy losses and the low V_{OC} (and as a consequence for the low overall efficiencies) observed for both cell architectures could lie in the broad manifold of CT states with energy relaxation towards the lowest states from where only weak radiative recombination is observed.

Table 6.3. The solar cell parameters extracted from j-V characteristics of PHJ and PMHJ solar cells recorded under illumination. Corresponding j-V curves are shown in Figure 6.16.

config.	V_{oc}, V	j_{sc}, mA/cm^2	*FF*, %	η, %
PHJ	0.50	-0.65	57	0.18
PMHJ	0.50	-0.24	40	0.05

In addition to j-V measurements on solar cells, the electrical conductivity in the dark σ_{dark} of pristine and blended films for varying molar doping ratios was also determined by Paul Beyer and Andreas Opitz (University of Berlin). The results are shown in Figure 6.17. Both pristine materials are reported to form films with high mobility, DIP for holes and electrons, PDIR-CN$_2$ only for electrons [262,263]. In the heterostructures σ_{dark} decreases by adding the other compound, which is readily explained by the altered crystal structure compared to both pristine materials and, as a consequence, lower ordering [264]. This minimum in σ_{dark} is reached around equimolar mixing ratios. Additionally, the electrical conductivity under illumination σ_{photo} was recorded to look at the photoconductivity of the blended system. The ratio of σ_{photo} to σ_{dark} is shown in Figure 6.17 (bottom panel). The strong decrease in the ratio of σ_{photo} to σ_{dark} supports the before mentioned discussion on

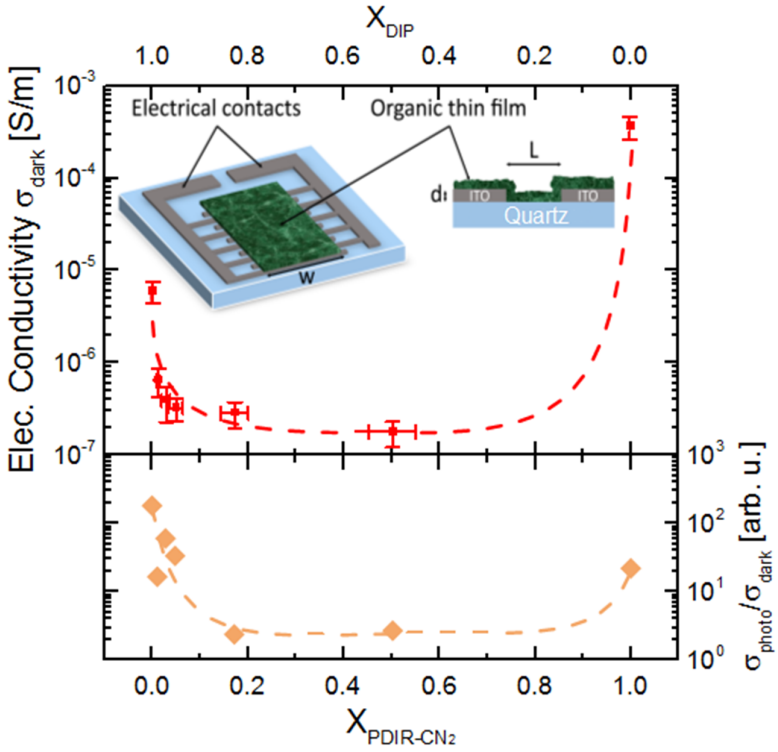


Figure 6.17. The electrical conductivity σ depending on the relative molecular concentration of PDIR-CN_2 to DIP is shown in the top panel. In the bottom panel the ratio $\sigma_{photo}/\sigma_{dark}$ between electrical conductivity under illumination and dark conditions is shown. The dashed lines serve as a guide to the eye. The images are taken from [2].

the photocurrent in solar cells. A similar conductivity decrease in molecular blends by dilution has been observed earlier [74,257,265].

Due to the intimate mixture of the molecules in the blended films, high recombination losses and charge trapping are present. This results in low conductivities of blended films together with the absence of increased conductivities under illumination in these films. These effects are limiting the overall performance of the PMHJ solar cells, as discussed before.

6.5 Discussion

The two perylene derivatives DIP and PDIR-CN_2 are an excellent model system to study CT effects in organic semiconductors. Mixtures are well ordered in the out-of-plane direction, which means each molecule has a well-defined inclination angle to the substrate. In the in-plane direction mixed films have a small coherent island size, but exhibit nevertheless preferential *D*/*A* stacking, which enables the CT state formation in this direction. Intermolecular *D*/*A* interactions are directly related to the overlap of their frontier orbitals, which is maximal in π-π stacking or face-to-face geometry. Therefore, the presented CT is stronger in mixed films (BHJ and PMHJ), where the molecule

reorientation facilitates orbital overlap, in contrast to planar interfaces (PHJ and SL) with almost exclusively edge-on-edge stacking.

A partial charge transfer in the ground state of 0.17 electrons determined from IR spectroscopy and DFT calculations was observed, which leads to a shift of the HOMO levels of both compounds towards each other. Judging from UPS data, it was find that the HOMO level offset in the mixture is only 1.00 eV in contrast to the 1.70 eV expected from vacuum level alignment. Although this relatively strong shift in the HOMO levels was found, there are no hints for new states or orbital hybridization in the ground state, since the mixed film valence region spectrum is just a superposition of the pristine film spectra taking into account the change of IE. The opposite is true for the excited state, where new states were observed via UV/Vis/NIR absorption spectroscopy and PL/EL spectroscopies. The resulting energy diagram for mixed films is presented in Figure 6.18 where the energy gap ΔE_{DA} of 1.65 eV and the dominant CT state of 1.48 eV give a CT exciton binding energy of about 0.2 eV. This is smaller than the exciton binding energy of the pristine materials (0.4-0.5 eV). The lower exciton binding energy of the CT state can be explained by the wider charge separation compared to the exciton associated with the first HOMO-LUMO transition in the pristine materials [266,267].

For many photovoltaic material combinations, highly sensitive methods are necessary to measure the weak CT transitions. However, for the case presented here, some of the strong CT absorptions are detectable with standard UV/Vis/NIR absorption spectroscopy. Furthermore, the CT absorption is present not only close to the absorption edge of the pristine materials, but it has a rather broad energy range of about 0.6 eV. One also find a corresponding feature in photoluminescence and electroluminescence at 1.4 eV with strong quenching of emission from the single components. The drastic change of molecular absorption and emission spectra provides strong evidence for the formation of a D/A complex with new electronic properties. Time-resolved PL reveals that the CT state life-time of 400-500 ps is significantly shorter compared to the individual compounds at 10 K and nearly independent from temperature. Judging from this, the CT states open the dominant recombination channel.

Importantly, our findings demonstrate the anisotropic character of the electronic transition to the excited CT state. As sketched in Figure 6.18 (bottom) it is strong in the in-plane direction, where π–π intermolecular stacking occurs (perpendicular to the molecular backbones), but absent between molecules in edge-on-edge configuration. Thus, π–π stacking is a prerequisite for the efficient intermolecular coupling, which is the main characteristic for GS-CT (Figure 1.1). If an intimately mixed structure is established, further properties of the formed complex are primarily determined by the energy level difference ΔE_{DA}, which in our case amounts to 1.65 eV, apparently too high for a substantial hybridization of the molecular orbitals. By considering the structural prerequisite of molecules to form π-π stacking and the magnitude of ΔE_{DA}, one may make a prediction for the interaction type that a D/A combination will exhibit. One can note further, that the anisotropic character of CT is not in contradiction with our observation of equal V_{OC} for PHJ and PMHJ solar cell configurations, because the rough polycrystalline DIP layer shown in Figure 6.1 offers enough surface area for π–π stacking with PDIR-CN$_2$ molecules

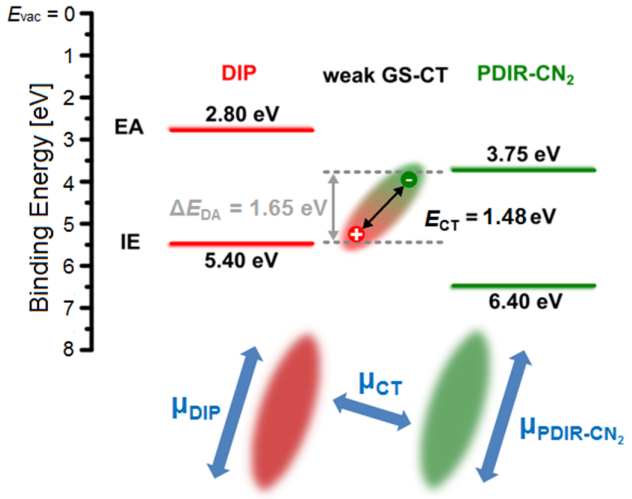


Figure 6.18. Schematic energy level diagram for mixture DIP:PDIR-CN2 (top) and orientations of transition dipole moments (bottom). IE values were determined by UPS, the EA values by subtracting the transport gaps from IE values. E_{CT} is taken from the strong CT energy calculated from the EL and IPCE data. ΔE_{DA} is the difference between the DIP IE and the PDIR-CN2 EA. The images are taken from [2].

even in a PHJ. Thus, the equality of the observed V_{OC}s underlines the dominance of the energetically favorable face-to-face CT recombination pathway.

The formation of coupled, but weakly ordered crystalline D/A complexes, where excited CT states serve as traps for excitons[74,257,265] and open pathways for radiative and non-radiative recombination, is accompanied by a decrease of charge carrier conductivity and an increase of energy losses. Nevertheless, material combinations with strong CT absorption could lead to increased short circuit current by using more photons from the infrared region. The overall efficiency could be increased by using well-ordered mixed-stack charge-transfer crystals due to improved extraction efficiency [89,268,269] and applying them as donor and/or acceptor in photovoltaic cells. Combining the higher degree of structural order, the broad CT absorption and reduced energy losses, might lead to new device architectures.

In summary, a comprehensive study of an organic *D/A* molecular system (DIP:PDIR-CN2) prepared by OMBD involving structural, optical, electronic and device characterization was performed. The formation of a CT complex characterized by a weak ground state interaction expressed in a partial CT of 0.17 electrons per molecule and a strong excited state CT, which is highly anisotropic in nature, was identified. The strong intermolecular coupling together with the intimately mixed structure without phase separation contributes to the large energy losses in solar cells from these materials.

CHAPTER 7

STRUCTURE-DEPENDENT CHARGE TRANSFER IN DIP/PEN:PDIR-CN$_2$/PDIF-CN$_2$

In this chapter the mixing behavior and intermolecular coupling of several donor and acceptor molecules in thin films prepared by organic molecular beam deposition (OMBD) are investigated. Diindenoperylene (DIP) and pentacene (PEN) were used as donor and perylene diimide derivatives (PDIR-CN$_2$ and PDIF-CN$_2$) as acceptor materials. The formation of strongly coupled charge transfer complexes vs. non-interacting phase separating components was studied using real-time and post-growth techniques for structural and optical analysis.

7.1 Structure Analysis

Reciprocal space maps of binary mixed thin films of DIP:PDIR-CN$_2$ as well as DIP:PDIF-CN$_2$ with different mixing ratios are shown in Figure 7.1. A growth temperature of 140 °C was chosen as a temperature at which both acceptor compounds reveal the

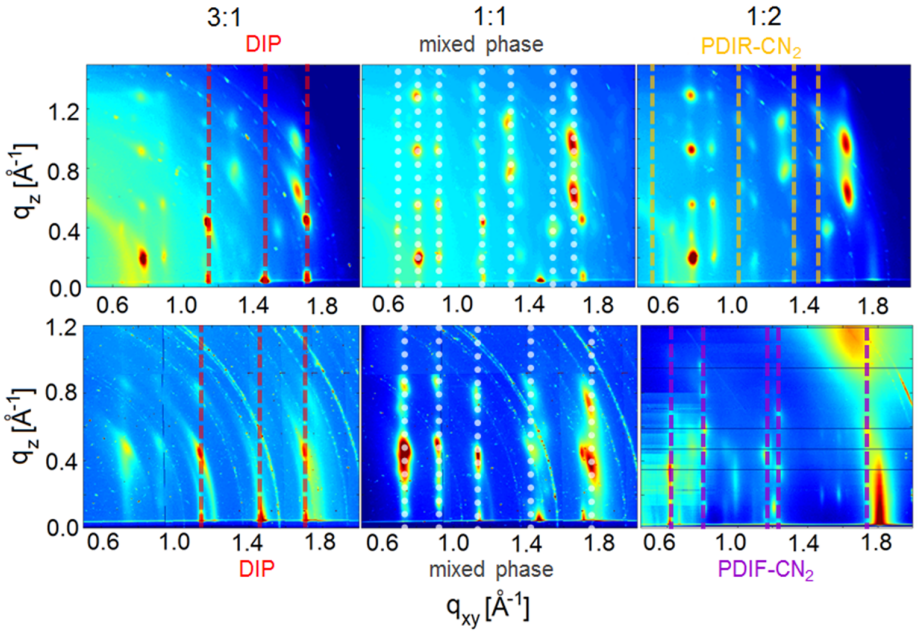


Figure 7.1. Reciprocal space maps of DIP:PDIR-CN$_2$ (top) and DIP:PDIF-CN$_2$ (bottom) deposited at 140 °C. The *Z*-axis is perpendicular to the substrate surface (*XY* plane).

highest crystallinity. In the case of PDIR-CN$_2$ coexistence of two polymorphs is observed as described in Chapter 5. In contrast, the DIP crystalline structure does not undergo significant changes when going from room substrate temperature (RT) to high substrate temperature (HT). In both equimolar mixtures (1:1) formation of mixed phases is clearly observed. The calculated lattice parameters are given in Table 7.1. The mixed phase unit cell volume is consistent with a sum of the donor and acceptor unit cells. When the amount of one component exceeds the second one, nucleation of a pure phase of the exceeding component occurs. Thus in non-equimolar blends (3:1, 1:2 in Figure 7.1) phase separation between the co-crystal and pristine phases takes place at high substrate temperature.

However, the diffraction pattern in DIP:PDIF-CN$_2$ 1:2 (bottom right corner of Figure 7.1) does not correspond to the crystal structure of PDIF-CN$_2$ observed in the pristine films (Section 5.1). Interestingly, the calculated volume of the possible unit cell is almost twice the original one (1574 Å^3 vs. 798 Å^3). This might be a hint for another polymorph similar to the HT-phase of PDIR-CN$_2$ containing two molecules per unit cell.

In addition, one can also note that at RT, where both acceptor materials exhibit a less ordered structure, only a short-range order is present in the mixed films (see Figure 7.2). One can observe the presence of the distorted pure phases in DIP:PDIR-CN$_2$ series which is not the case for DIP:PDIF-CN$_2$.

Diffraction images of mixtures with PEN deposited at 70 °C are shown in Figure 7.3. The temperature is chosen due to weak adsorption of PEN molecules on SiO$_x$. At this temperature neither PDIR-CN$_2$ nor PDIF-CN$_2$ undergo a phase transition and reveal structural properties similar to those at RT. Thus, PDIR-CN$_2$ thin films contain crystalline domains of the RT-polymorph and PDIF-CN$_2$ thin films exhibit a weak scattering from the nearly amorphous structure as discussed earlier. Both components PEN and PDIR-CN$_2$ maintain their individual diffraction patterns in the mixed film and no further diffraction peaks are observed. This evidences a strong phase separation between the species with their unit cell remaining unperturbed. However, formation of a pronounced co-crystal is

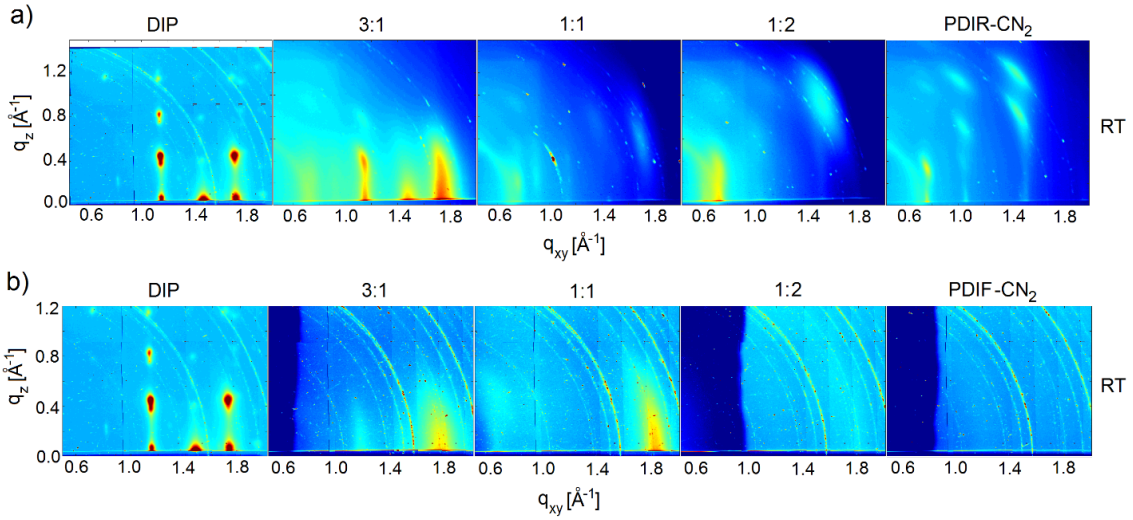


Figure 7.2. Reciprocal space maps of DIP:PDIR-CN$_2$ (a) and DIP:PDIF-CN$_2$ (b) deposited at room substrate temperature. The *Z*-axis is perpendicular to the substrate surface (*XY* plane).

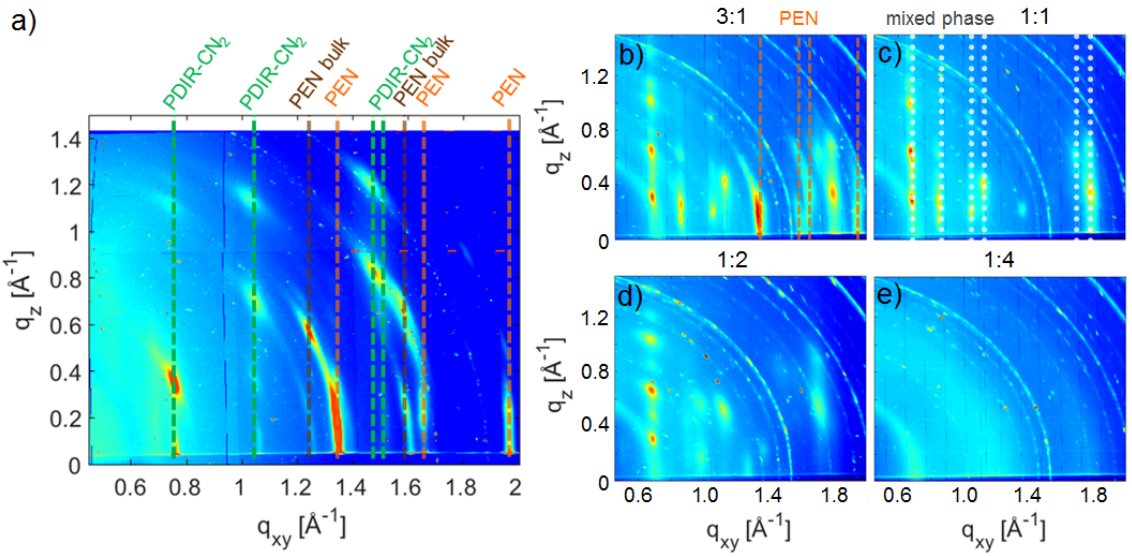


Figure 7.3. Reciprocal space maps of PEN:PDIR-CN_2 1:1 100 nm film (a) and PEN:PDIF-CN_2 mixed films (b)-(e) deposited at 70 °C.

observed for PEN:PDIF-CN_2 mixed films (Figure 7.3b-e), wherein the excess of PEN molecules nucleates separately (Figure 7.3b) and the excess of the amorphous PDIF-CN_2 phase leads to a "dilution" of the mixed phase: the crystalline order decreases in the amorphous matrix (Figure 7.3d,e).

Table 7.1. Co-crystals unit cell parameters.

D/A system	*a*, Å	*b*, Å	*c*, Å	*α*,	*β*,	*γ*,	*V*, Å³
DIP:PDIR-CN_2 1:1	8.45	10.07	17.41	86.09	103.85	103.64	1396.37
DIP:PDIF-CN_2 1:1	8.72	8.97	17.25	85.83	97.93	101.91	1307.06
DIP:PDIF-CN_2 1:2	8.49	11.01	18.08	86.72	97.86	109.88	1573.56
PEN:PDIF-CN_2 1:1	7.44	9.30	17.95	96.55	81.74	94.25	1218.54

7.2 FTIR Measurements

In order to find out whether a ground-state CT is present in the studied systems FTIR measurements were performed. The recorded transmission spectra are presented in Figure 7.4. A characteristic shift of the $-CN_2$ vibrational mode is present in DIP:PDIF-CN_2, PEN:PDIF-CN_2 similar to that in DIP:PDIR-CN_2 discussed in Section 6.2. At the same time, no distinct shift in the PEN:PDIR-CN_2 spectrum is observed. A similar correlation between vibrational-mode shifts and *D/A* mixing/demixing has been observed for polymer:fullerene systems [247].

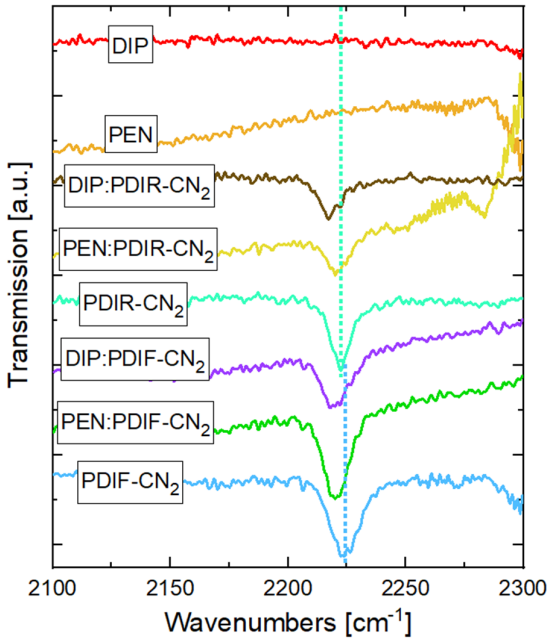


Figure 7.4. FTIR transmission spectra of neat DIP, PEN, PDIR-CN_2, PDIF-CN_2 and mixed films (1:1). A shift of the characteristic –CN_2 stretching mode at 2222.3 cm^{-1} for PDIR-CN_2 (light green) and 2224.1 cm^{-1} for PDIF-CN_2 (blue) serves as an indication of a partial ground state CT.

7.3 Optical Absorption and Emission Spectra

All changes experienced by organic molecules due to a modification of the environment are reflected in the molecular electronic structure through new features (e.g. energy shifts, band shape modification, appearance/disappearance of new transitions) into the optical absorption and emission spectra. Thus, in the optical absorption spectra (Figures 7.5a and b) the first fundamental transitions around 2.2 eV of pristine PDIR-CN_2 and PDIF-CN_2 grown at high substrate temperature originate from J-like coupling due to a longitudinal displacement between molecules in the crystal phases. The absorption spectrum of DIP also undergoes changes in comparison with the solution spectrum due to the long-range intermolecular interactions upon crystallization in thin films[109]. It is worth mentioning that in solution both DIP and PDI molecules show a similar spectrum with the first transition around 2.35 eV. For PEN, the optical energy gap is narrower – about 2.1 eV [175]. Upon formation of a *D*/*A* co-crystal the resulting absorption spectrum of thin films with a mixing ratio close to equimolar resembles neither spectra of the individual molecules nor spectra of the pristine thin films, as it is the case for DIP:PDIR-CN_2, DIP:PDIF-CN_2, and PEN:PDIF-CN_2 (Figures 7.5a,b,d). Intermolecular coupling favored by the closely packed *D*/*A* molecules in the mixed phases causes the changes in the band shape and appearance of new absorption bands in the subgap energy regions (see insets in Figure 7.5). Such subgap absorption bands are generally attributed to a direct CT transition from the HOMO of a donor molecule to the LUMO of an acceptor molecule upon excitation as discussed in Section 6.3. The spectra of the equimolar blends in both DIP systems look

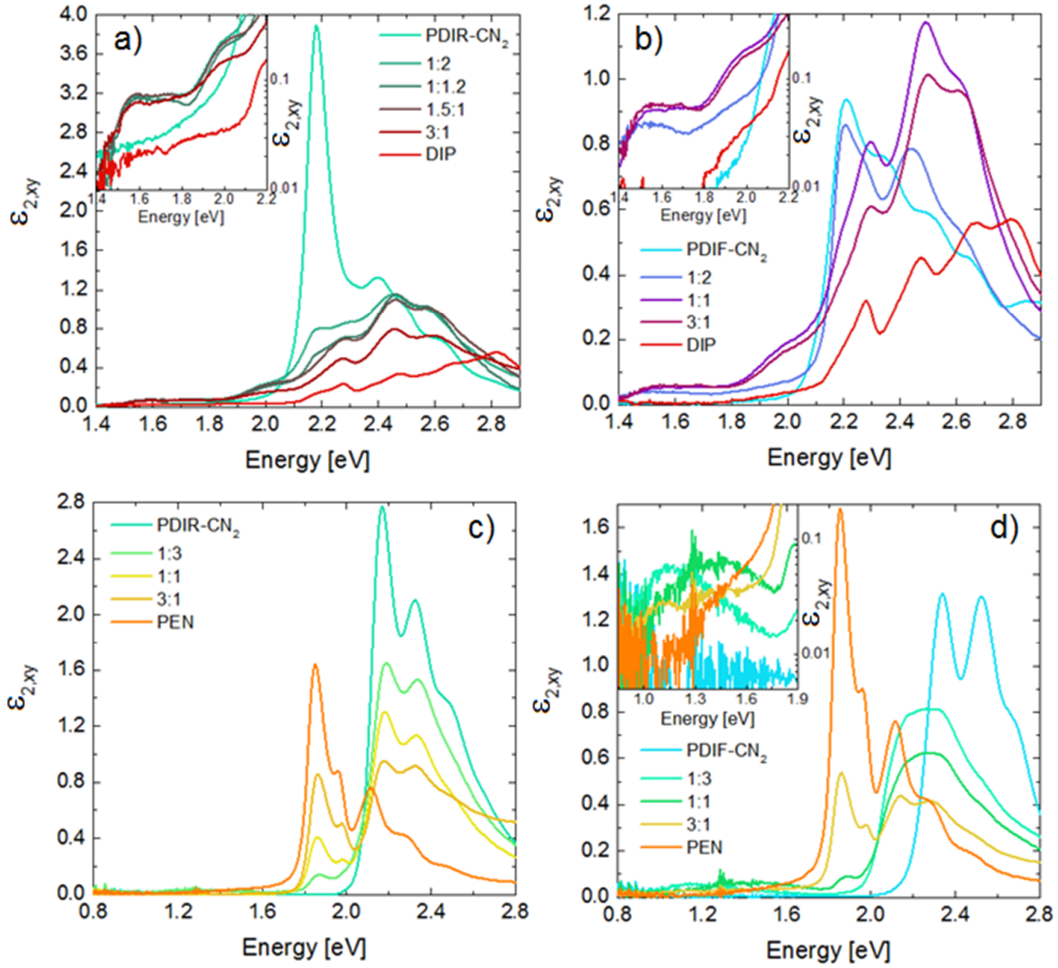


Figure 7.5. Optical absorption spectra in the in-plane direction evaluated from ellipsometry data: (a) DIP:PDIR-CN_2 at 140 °C; (b) DIP:PDIF-CN_2 at 140 °C; (c) PEN:PDIR-CN_2 at 70 °C; (d) PEN:PDIF-CN_2 at 70 °C. The insets show zooms into subgap regions containing the CT bands.

similar with a relatively strong complex CT band between 1.4 – 2.1 eV and the intensity center of mass shifted towards higher energy (2.5 eV). The similarity can be explained by the fact that the DIP molecules interact directly with the perylene diimide backbones, which are identical for both PDIR-CN_2 and PDIF-CN_2, whereas the acceptors' optical properties in thin films are affected by the environment via the different side chains. When the mixing ratio deviates from 1:1, optical traits inherent to the pure donor or acceptor crystalline phases become more pronounced making the resulting spectrum a superposition of the pure materials and the mixed phase spectra. This observation supports the conclusions on the structure made in the previous section.

In the PEN:PDIR-CN_2 system, where strong phase separation is observed, the optical behavior is different (Figure 7.5c). Spectra of the mixed films resemble a simple superposition of both original components with a gradual change in accordance to the mixing ratios. In this, the optical features attributed to the pristine crystal phases, such as a Davydov splitting of the red-shifted 0-0 transition between 1.8 – 2.0 eV in PEN and the

red-shifted 0-0 transition in PDIR-CN$_2$ around 2.2 eV, persist in the blends. Note that the oscillation strength of the excitation transitions in PDIR-CN$_2$ along the in-plane direction is higher than that in PEN, and therefore a contribution of PDIR-CN$_2$ dominates in the resulting spectra of the blends. In contrast, when mixing with PDIF-CN$_2$ (Figure 7.5d) modification of the optical response is observed again. Excitons generated in PEN:PDIF-CN$_2$ system seem to be more delocalized compared to those in DIP systems, because single transitions are not distinguishable between 2.0 – 2.4 eV (energy range corresponds to the first transitions of PEN and PDIF-CN$_2$ in solution) in 1:1 and 1:3 mixtures. The spectrum broadening may stem from vibronic coupling which can induce hybrid states between the lowest local-excitation and CT states [270]. Emergence of a subgap absorption band, although weaker in comparison with DIP mixtures, is also found. The CT absorption band starts at around 1.0 eV. The difference with the DIP:PDIR-CN$_2$ and DIP:PDIF-CN$_2$ systems of ~0.4-0.5 eV is consistent with the lower-lying HOMO level of DIP (Figure 4.1).

The PL spectra measured at RT (solid) and 77 K (dotted) are shown in Figure 7.6. In DIP mixtures (Figure 7.6a,b) strong quenching of the singlet exciton emission and an appearance of a typical CT peak around 1.4 eV are observed. Remarkably, when the molecules are evenly distributed within a film without pure phases, which is the case for equimolar blends in both systems (see also Figure 6.12d) and 3:1 and 1:3 DIP:PDIF-CN$_2$ films at RT (Figure C.1 in Appendix C) only the CT emission is observed. In other cases, when segregation of a pure phase is observed, the emission between 1.6-2.2 eV indicates crystallites of the excess component. An emission quenching often is a characteristic of face-to-face arrangement and beneficial for solar cell application because of reduced recombination rates [271,272]. However, the ultrafast relaxation within the CT band competes with the dissociation process into charge carriers [273] contributing into the energy loss enhancement unless the lowest CT state is weakly bound [46]. The latter is rarely the case with face-to-face orientation. In contrast, highly emissive PDIR-CN$_2$ fully dominates a spectrum when mixed with PEN (Figure 7.6c). PEN features are distinguishable only in the 3:1 film since the photolumiscence intensity from PEN is originally a few orders of magnitude weaker. In agreement with the results described above, no evidences for intermolecular coupling in PEN:PDIR-CN$_2$ is found. Although PDIF-CN$_2$ on par with PDIR-CN$_2$ exhibits strong emission, upon intermixing with PEN a decrease of the intensity by 2 orders of magnitude is seen in Figure 7.6d. Besides, in the mixtures a band shape of the residual emission resembles the PDIF-CN$_2$ monomer spectrum and not that of the thin film. Due to the instrument limit the energy range below 1.2 eV, where a possible CT peak is expected judging from the absorption data, cannot be explored. However, the available data along with FTIR measurements (Figure 7.4) provide sufficient evidence of CT in PEN:PDIF-CN$_2$ mixed films.

7.4 AFM Images of 1:1 Mixtures

Having described general interaction processes in DIP and PEN binary mixtures with PDI acceptors, now formation of the *D*/*A* co-crystals with the properties of a CT complex can be

considered in more detail. For this purpose, one can first address the thin films morphology investigation. AFM images of the purely films and equimolar blends are provided in Figure 7.7. Both pure DIP and PDIR-CN$_2$ at HT follow the layer-plus-island growth (Stranski-

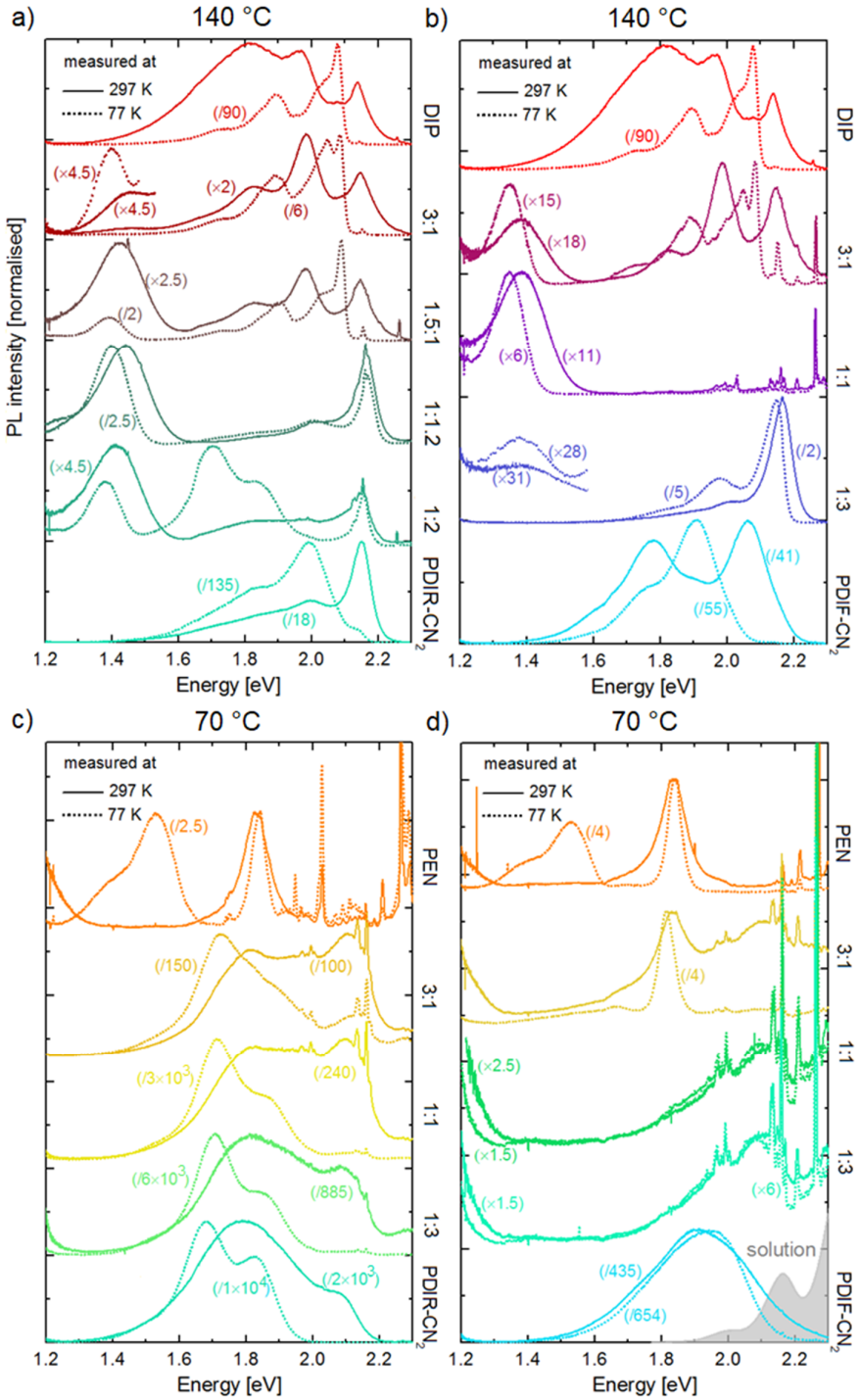


Figure 7.6. Photoluminescence spectra recorded at 297 K (solid) and 77 K (dotted): (a) DIP:PDIR-CN$_2$ at 140 °C; (b) DIP:PDIF-CN$_2$ at 140 °C; (c) PEN:PDIR-CN$_2$ at 70 °C; (d) PEN:PDIF-CN$_2$ at 70 °C. All intensities are normalized to the donors´ intensities. An intensity increase at 1.2 eV is a background due to the instrument limit.

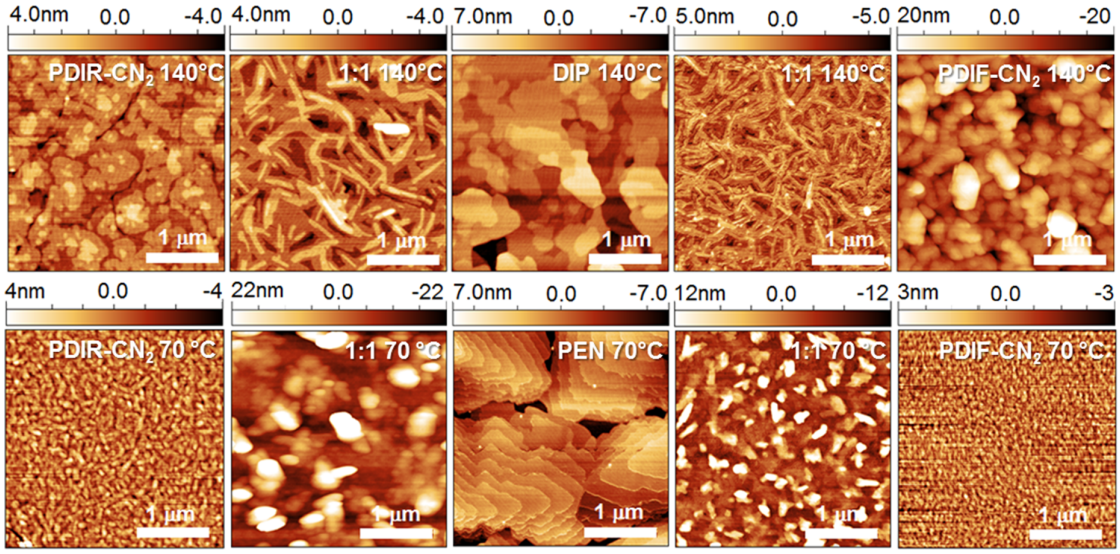


Figure 7.7. AFM images 3 × 3 μm of neat and 1:1 films: upper row - DIP systems; bottom row – PEN systems.

Krastanov) mode forming flat terraces on top of the previous layer. As can be seen from the round shape of the terraces, there is no favored growth direction within the surface plane. PDIF-CN_2 at HT reveals growth along all three axes. Thus round islands dominate on the surface. Yet, upon intermixing of PDIs with DIP at HT pronounced needle-like features emerge. The islands are longer in DIP:PDIR-CN_2: 0.5 – 0.8 μm as opposed to 0.2 – 0.5 μm in DIP:PDIF-CN_2. This evidences a preferred 1D growth which most probably occurs along a direction of the $\pi - \pi$ stacking between the *D* and *A* moieties [213,274]. PEN molecules are arranged into so called "wedding-cake" islands, a morphology typical of rod-like organic molecules. The equimolar blend with PDIR-CN_2 features a surface consisting of round domains with a diameter of 0.1 – 0.5 μm which cannot be assigned to a certain compound. The mixture with PDIF-CN_2 is full of small elongated grains with a lateral size of 0.05 – 0.3 μm which might be related to the 1:1 co-crystal.

7.5 DRS on 1:1 Mixtures

The formation of a CT complex can be followed in situ and in real time by DRS during film deposition (Figure 7.8) allowing to monitor instant changes in the optical absorption spectra. As can be seen from Figure 7.8a,b, in DIP mixtures already the first monolayer (ML) is different from the spectra of the pure *D* and *A* materials and the co-crystal is formed. Due to the relatively high oscillation strength the CT bands can be detected with DRS. The band develops over the first few MLs and saturates after 15 nm in DIP:PDIR-CN_2 and 10 nm in DIP:PDIF-CN_2. In contrary, in PEN films one can clearly see in the beginning of growth the monomer spectrum of the PDIs and a shoulder at 2.1 eV originating from the PEN monomers. Then, both parts of the spectrum belonging to crystalline PEN and PDIR-CN_2 develop independently during PEN:PDIR-CN_2 film growth (Figure 7.8c). The signature of crystalline PEN is also present in the PEN:PDIF-CN_2 equimolar blend

(between 1.8 – 2.0 eV in Figure 7.8d), whereas the PDIF-CN_2 part undergoes significant changes towards formation of the delocalized absorption band with the maximum between 2.1 – 2.3 eV.

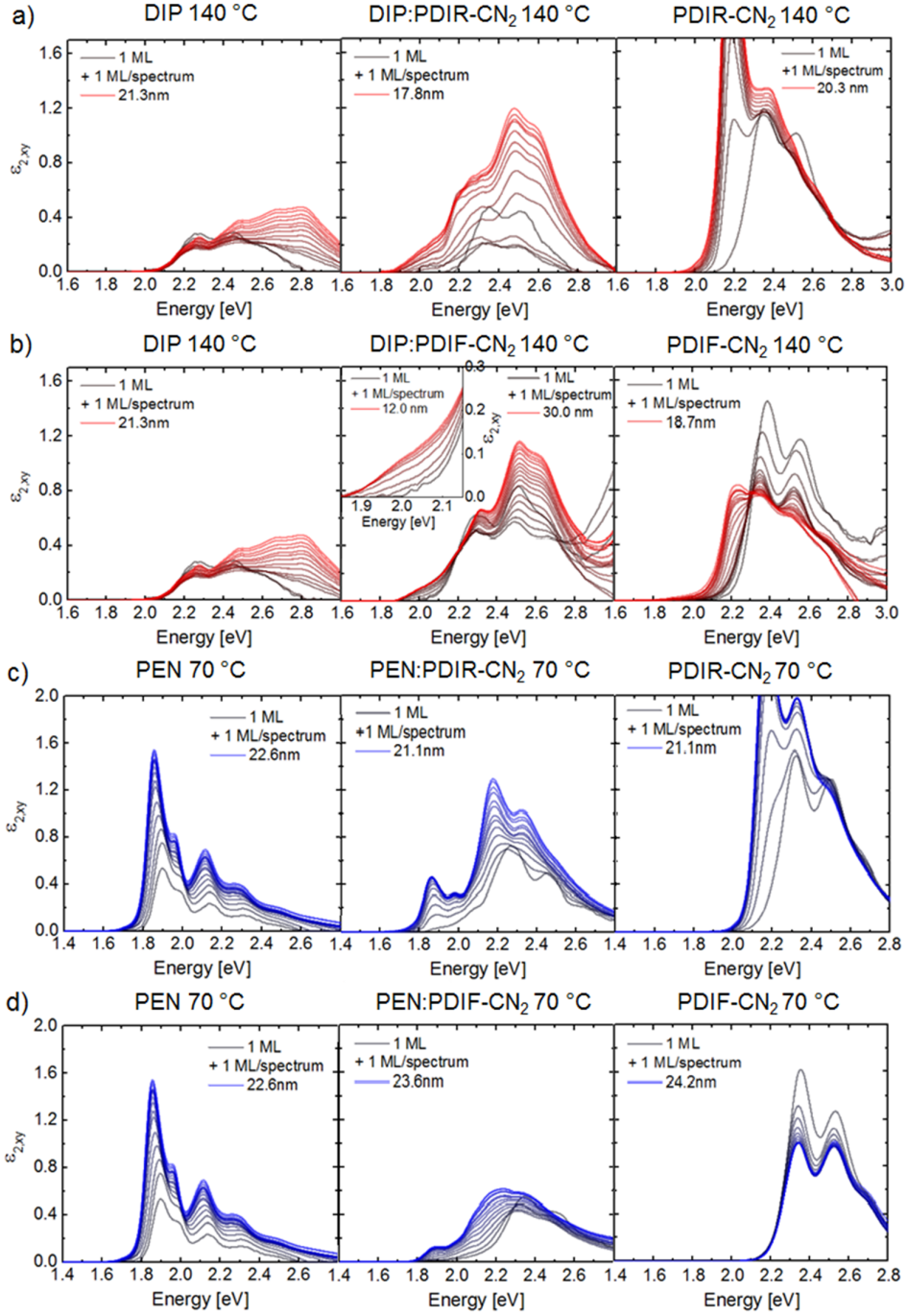


Figure 7.8. DRS spectra of pristine and 1:1 films: (a) DIP:PDIR-CN_2 at 140 °C; (b) DIP:PDIF-CN_2 at 140 °C; (c) PEN:PDIR-CN_2 at 70 °C; (d) PEN:PDIF-CN_2 at 70 °C. The inset shows a zoom into subgap regions containing the CT bands. Note, the detector sensitivity and energy range are not sufficient to distinguish the weak CT band in PEN:PDIF-CN_2.

7.6 Structure - CT Properties in DIP:PDIF-CN$_2$

In order to correlate CT optical features with structural parameters the DIP:PDIF-CN$_2$ system can be examined in detail (Figures 7.9 and 7.10). Real-time GIXD of a film with a small DIP excess (Figure 7.9a) shows that the diffraction peak around 1.8 Å^{-1} associated with the π-π stacking distance of about 3.5 Å typical for co-crystals appears from the 2nd ML. From the real-time data one can see that the mixed phase starts to nucleate earlier than the DIP phase, supporting the idea of the preferred *D*/*A* bonding interaction. In this case ripening and growth of the DIP phase is rather induced by supersaturation of the excessive material [79,275]. In Figure 7.9b a comparison of the coherent crystal grain sizes (evaluated using the formula 3.4) is plotted. The evolution of the mixed phase can be directly compared with the DRS signal of the CT absorption band in the inset in Figure 7.8b. An interesting finding is that the CT band saturates after ~6-7 monolayers which coincides with the mixed phase crystals formation.

In Figure 7.10 structural (a) and optical (b) changes caused by different T_{sub} are provided. In Figure 7.10a one can see how the structural order increases with the temperature from the increasing contrast of the mixed phase diffraction features. The width of the Bragg peak at q_{xy} = 0.75 Å^{-1} was fitted for all four temperatures. Using the Scherrer formula (Equation 3.4) the corresponding coherent scattering length l_s was determined. The corresponding rise of the oscillator strength of the absorption and emission CT bands in Figure 7.10b allows to relate these two effects: the CT absorption is plotted in Figure 7.11 as a function of l_s.

The structural dependence can be rationalized in a way that the enhanced crystallinity of the co-crystal can be unambiguously attributed to the increased number of the *D*/*A*

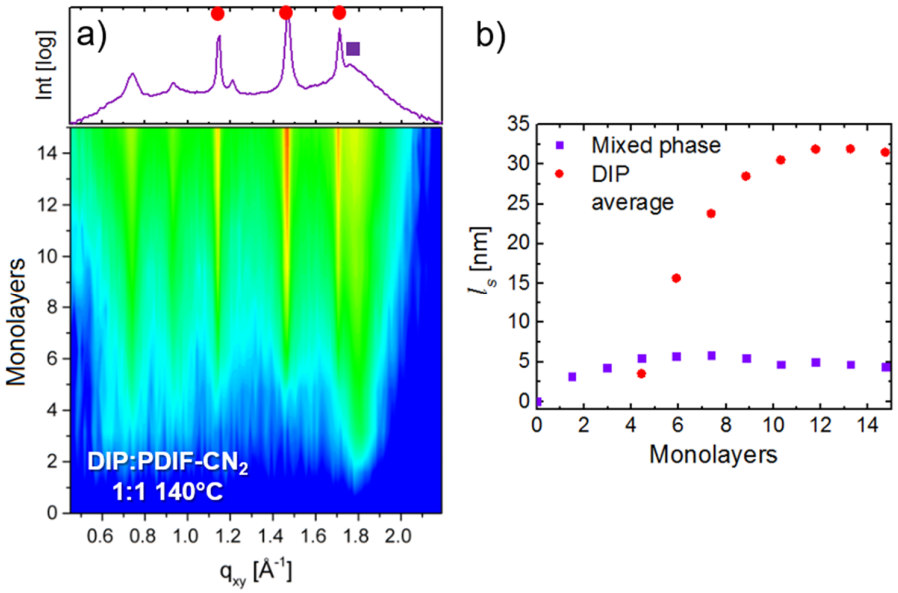


Figure 7.9. (a) Real-time GIXD on the nearly 1:1 DIP:PDIF-CN$_2$ film with a small DIP excess grown at 140 °C; red dots mark DIP diffraction peaks, the violet square marks the most characteristic peak of the mixed phase. (b) A plot of the scattering length versus number of monolayers shows a competition of the mixed and pure DIP crystal phases.

complexes which is in a direct correlation to the strength of the CT absorption band [276–278]. If the structure factor is excluded by comparison of systems of similar crystallinity a degree of the electronic coupling between the ground and excited CT state can be estimated as well.

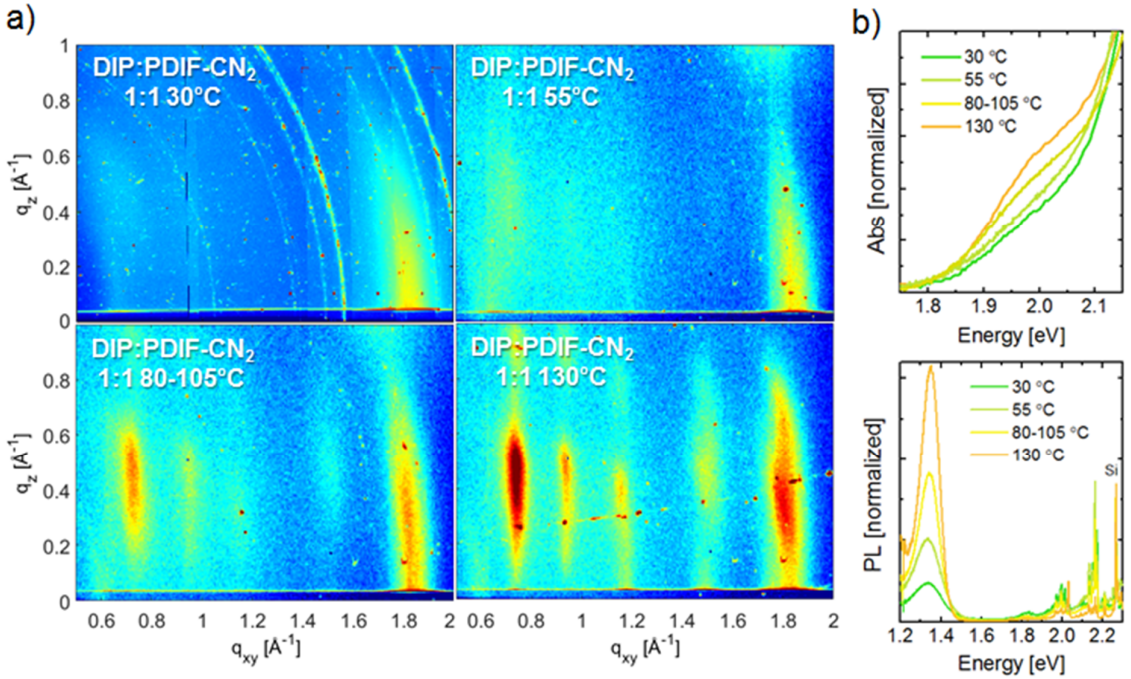


Figure 7.10. Temperature-dependent study of structural and optical properties of the mixed phase. (a) Reciprocal space maps of DIP:PDIF-CN_2 deposited at different substrate temperatures. (b) Characteristic optical absorption (top) and emission (bottom) CT features of DIP:PDIF-CN_2 films grown at different substrate temperatures.

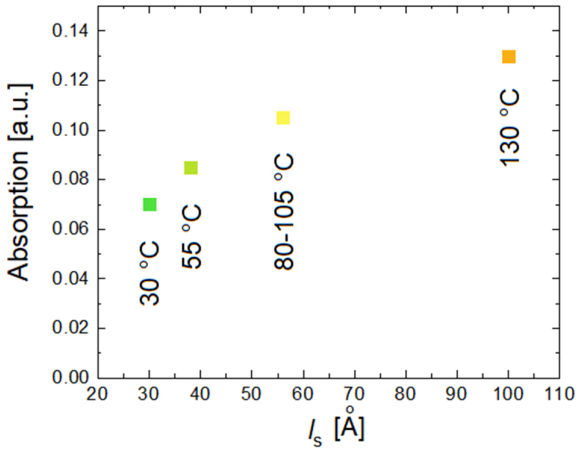


Figure 7.11. CT absorption at 2.0 eV from Figure 7.10b (top) as a function of the scattering length.

7.7 Discussion

In the present thesis co-evaporated binary mixtures of small molecule OSC are considered. The capabilities of the donor and acceptor molecules with different sterical and energetic properties to interact and form a CT complex are compared. Thus, two main parameters are examined: structural compatibility due to the molecular geometry and energy gap E_{DA}.

In all three *D*/*A* systems the CT complex formation correlates with intermixing of the components accompanied by a mixed phase formation during film deposition, whereas the strongly segregating system preserves the structural and optical characteristics of both moieties. However, the mixing vs. demixing scenario is apparently determined by the molecule tendency to intermolecular coupling. The intermolecular interactions between *D* and *A* moieties are not necessarily based on CT in the ground electronic state, although it is apparently present in the studied systems (FTIR in Figure 7.6) and can have a van der Waals nature as well[247].

Here, we suggest to consider the mixing scenarios between the studied small molecule materials in terms of a nearest-neighbor interaction model introduced by Kitaigorodsky, where the main driving force of a phase nucleation is a difference between host-host, guest-guest and host-guest intermolecular interactions *W* (see Section 2.2).

Based on the results, the proposed morphologies are visually summarized in Figure 7.12. The first row shows the mixing behavior in DIP systems at RT. At RT, PDIF-CN$_2$ the films are nearly amorphous (up to ~110-120 °C). The PDIR-CN$_2$ films are weakly crystalline due to the shielding effect of the side chains, as opposed to DIP and PEN. Thus, $W_{\text{PDIF-PDIF}}$ is considered to be the smallest one in comparison with $W_{\text{PDIR-PDIR}}$, $W_{\text{DIP-DIP}}$, and $W_{\text{PEN-PEN}}$. This allows PDIF-CN$_2$ molecules to easily intermix with sterically compatible DIP molecules. Due to the disruptive influence of PDIF-CN$_2$ molecules an excess of DIP does not maintain the long-range order (Figure 7.2b). This leads to the formation of a solid solution (in the absence of the preferred crystal packing) with the properties of the CT complex even for non-equimolar films (Appendix C). Nucleation of the PDIF-CN$_2$ crystalline phase occurs at HT when the higher kinetic energies enable a stabilizing π–π interaction between the perylene diimide backbones. This results in coexistence of the neat and mixed crystal phases. The strength of the CT complex optical features such as the absorption and emission bands correlates directly with the co-crystal grain size which increases with the T_{sub} (Figures 7.10 and 7.11).

Amongst the given material combinations, the intermolecular interactions between DIP and PDIR-CN$_2$ seem to be the strongest. The alkyl side chains have the weaker hindering effect on PDIR-CN$_2$ intermolecular coupling in comparison with the fluorinated chains and therefore crystallinity is present at RT. Consequently, phase separation is observed at RT in contrasts to DIP:PDIF-CN$_2$. HT promotes formation of the highly-crystalline extended one-dimensional *D*/*A* packing. In general, for small aromatic molecules, in particular for rod-like molecules, a face-centered parallel stacking is disfavored, in contrast to T-shaped or offset-stacked geometries (herringbone structure as a compromise) due to electrostatic repulsion. This is the case unless electrostatic interaction of donor (electron-donating) and

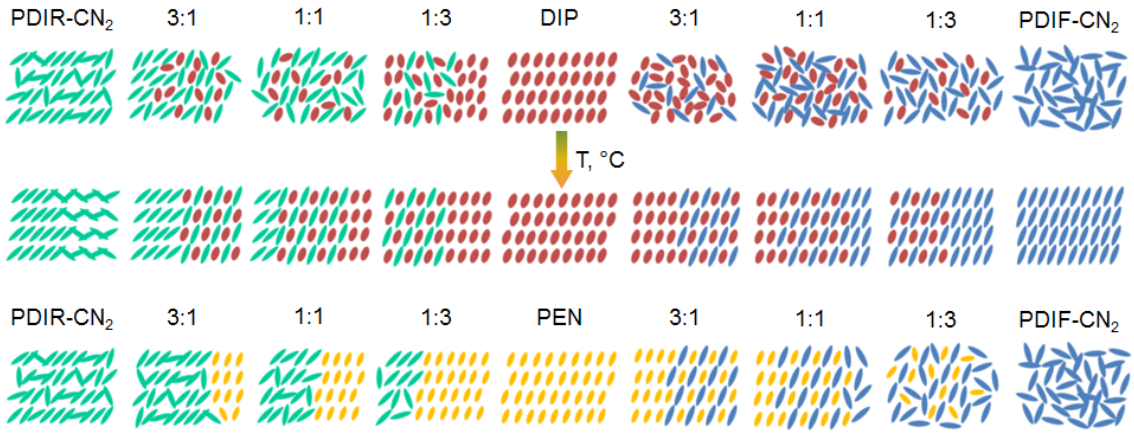


Figure 7.12. Sketches illustrating mixing behaviors of DIP (upper row) and PEN (bottom row) mixtures. The side chains in the PDIs are omitted for clarity.

acceptor (electron-withdrawing) species contributes to the force balance [103,106]. This is a reason for the most-observed *D*/*A* co-crystal geometry [213,272,274].

Whereas the mixing scenario can be rationalized using the nearest-neighbor approach, the further phase evolution is a result of a complex impact of kinetic parameters such as diffusion, mobility, deposition rate, and temperature [275,279,280]. It has been observed that elevated processing temperatures facilitate demixing of chemically or sterically incompatible molecules[281]. At HT even a slight deviation from the 1:1 stoichiometry induces nucleation of the pure phase, which nevertheless do not compete with the mixed phase. The results provide an option to maintain both mixed and neat phases when the increased crystallinity is achieved, while at RT all studied mixed phases are weakly-ordered and resemble a statistic mixture, which seems to strongly limit the charge carrier mobility [2,70,257].

PEN molecules are apparently less sterically compatible with the larger PDI molecules or/and the area of the aromatic system is too small[78]. As a consequence, PEN:PDIR-CN_2 is the only system where neither CT nor intermolecular coupling is observed. Intermixing of PEN with PDIF-CN_2 is possible owing to the weak $W_{PDIF\text{-}PDIF}$ coupling which is suppressed by the shielding effect of the fluorinated side chains. However, the pure PEN phase persists in 3:1 and likely even in 1:1 mixtures. With the further increase of PDIF-CN_2 content the mixed phase experiences dilution within the amorphous matrix.

The competition between donor-donor, acceptor-acceptor, and donor-acceptor binding energies is sketched as an energy diagram in Figure 7.13. The latter term is favored for highly compatible DIP:PDIs and less compatible PEN:PDIF-CN_2. Therefore, the minima in the diagram refer to the most energetically stable structure. $W_{PEN:PDIF}$ is sufficient to overcome weak $W_{PDIF:PDIF}$, and therefore the free energy gain is achieved by formation of the co-crystal. An increase in the binding energy in mixed binary films was also measured earlier for PEN:PFP by thermal desorption spectroscopy [282]. However, the PDIR-CN_2 phase is energetically more stable than the PDIF-CN_2 phase and does not follow this scenario.

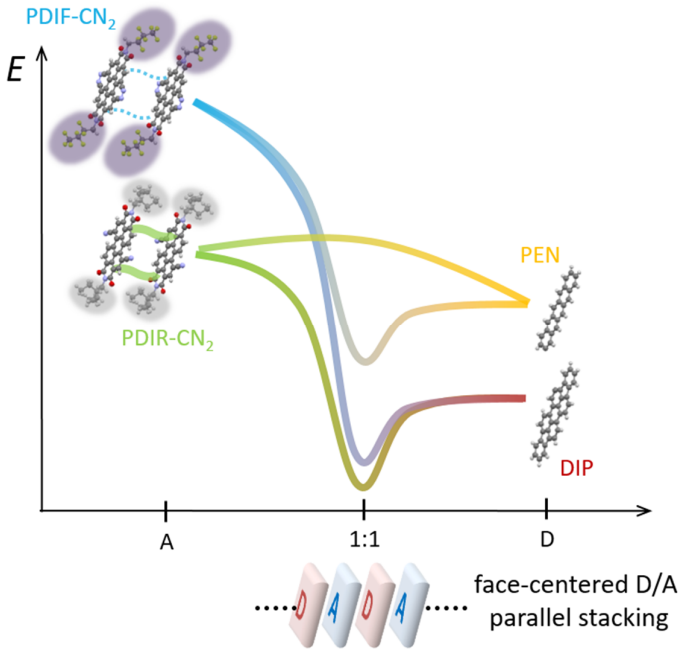


Figure 7.13. Diagram sketching the energetically beneficial co-crystal formation in case of DIP:PDIR-CN_2, DIP:PDIF-CN_2, and PEN:PDIF-CN_2. The interaction between PEN and PDIR-CN_2 is not sufficient to compete with PDIR-CN_2 – PDIR-CN_2 bonding forces whereas weakly bound PDIF-CN_2 molecules dissociate more easily.

Further, for the intermixing *D*/*A* systems where the CT complex formation is observed, the role of a relative position of the HOMO-LUMO energy levels can be considered. The energy levels measured in the pristine films are summarized in Figure 7.14 (left). Note that all values are provided for thin films grown at RT [1,2,154,155]. The widest E_{DA} seems to be between DIP and PDIR-CN_2, followed by DIP and PDIF-CN_2, and the narrowest one is supposed to be between PEN and PDIF-CN_2. However, as discussed in Chapter 5, the energy shift between PDIR-CN_2 and PDIF-CN_2 thin films originates from the polarization effect of the fluorinated side chains exhibiting higher electron density in comparison with the perylene diimide backbone, whereas the electronic structure of the monomers in absence of the environmental effects stays similar. The sketch in Figure 7.15a illustrates how the photoelectron kinetic energy measured by UPS is affected by the surface dipole moment *P* created by the difference in the electron density of the fluorinated side chains and the aromatic core [235,236,283].

This can be an explanation why, despite the fact that the different side substituents heavily affect the thin film structural and optical properties, the resulting *D*/*A* complexes exhibit almost identical energetic landscapes (Figure 7.4a,b) in DIP:PDIR-CN_2 and DIP:PDIF-CN_2. Thus the CT state energies differ by about 0.05 eV for DIP:PDIF-CN_2 as shown in Figure 7.14 (right), which is approximately one order of magnitude smaller than the measured difference in the EA for the pristine acceptor thin films. Furthermore, the oscillator strength of the CT optical features seems correlate directly with the co-crystal quality, which is the best in case of DIP:PDIR-CN_2 grown at 140 °C. Thus the main idea is

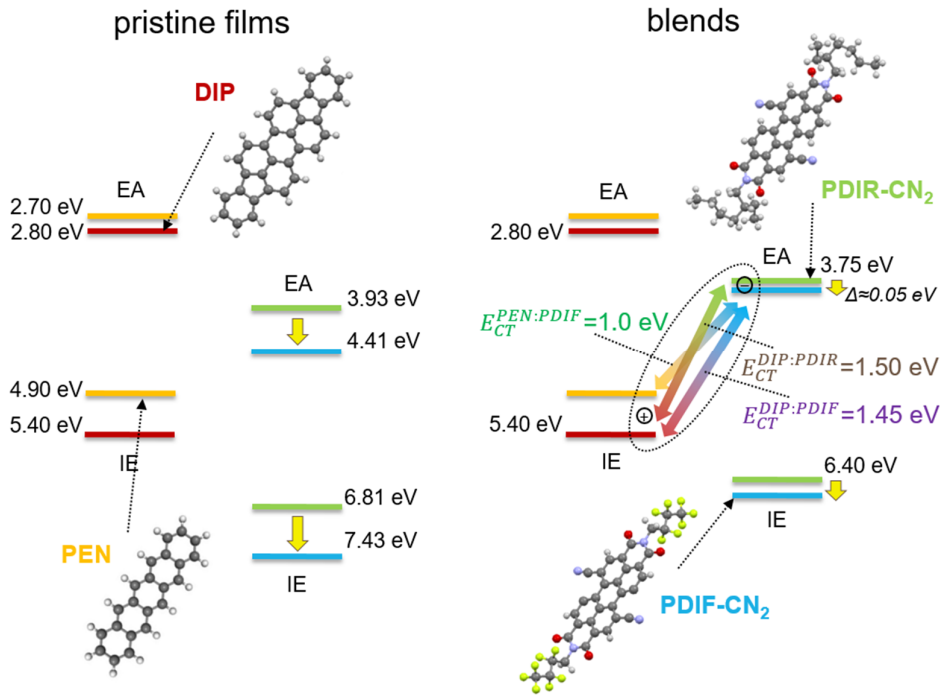


Figure 7.14. Energy level diagrams for the pristine films (left) and the *D*/*A* blends (right). The yellow arrows are guides to the eye for the energy shift between PDIR-CN_2 and PDIF-CN_2. The CT energies (except for DIP:PDIR-CN_2) are based on the optical data.

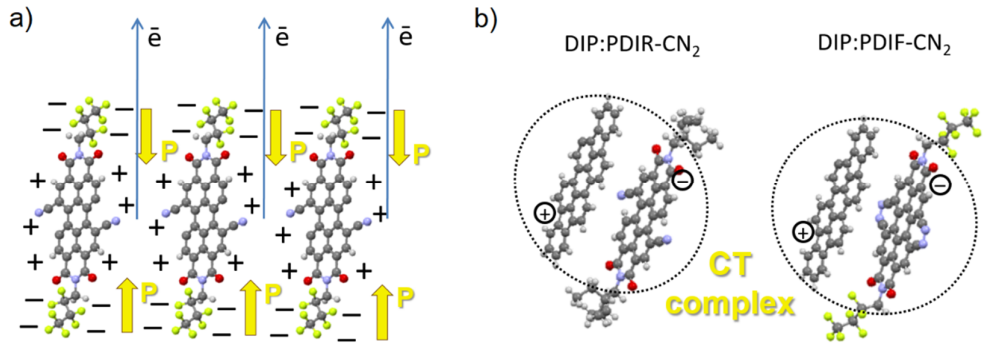


Figure 7.15. (a) Illustration on how the surface dipole moment *P* can affect the photoelectron kinetic energy in a PDIF-CN_2 layer; (b) The CT complex formed between the aromatic backbones is not strongly influenced by the acceptor side chains.

that the CT complex is formed between a DIP molecule and a perylene diimide backbone, and since the CT transition is anisotropic and oriented parallel to the π-π stacking, the replacement of the acceptor has no strong impact on its properties in the particular case (Figure 7.15b). Therefore, one may conclude that environment effects, such as polarization etc., have no strong impact on the strength of a *D*/*A* couple as soon as their molecular orbitals are structurally accessible for a close interaction.

The replacement of DIP by PEN causes strong alterations in the intermolecular coupling behavior, which is present in PEN:PDIF-CN_2 including formation of a CT

complex and absent in PEN:PDIR-CN_2. The CT features in PEN:PDIF-CN_2 are less prominent compared to the DIP systems. The higher PEN HOMO level results in the corresponding red-shift of the CT states ($E_{CT} \approx 1$ eV in Figure 7.13, right). However, this does not ensure formation of a "stronger" CT complex with predominantly hybridized molecular orbitals as can be evidenced from both UV/Vis and FTIR data, at least until the structure factor is excluded.

To conclude, the results show a direct correlation between small molecule compatibility and the CT properties of the corresponding *D*/*A* complex. The morphology of a small molecule *D*/*A* mixture can be controlled by tailoring the intermolecular interactions via change of molecule geometry and/or substrate temperature. The formation of a CT complex is a function of the film structure and the energy gap E_{DA} but apparently does not depend on the relative orientation of the *D* and *A* transition dipole moments.

Part III

Summary and Outlook

CHAPTER 8

SUMMARY AND CONCLUSION

In the present thesis the interplay between the steric properties, defined by the chemical composition and configuration, of rod-like small molecules, the thin film growth and ordering behavior, and the thin film optical properties has been thoroughly investigated. The CT properties of the resulting *D*/*A* blended system are found to be in a direct correlation with the *D*/*A* backbone intermolecular coupling that induces specific morphologies.

8.1 Results on Acceptor Materials

The two PDI semiconductors have a similar chemical structure with their bulky side chains limiting molecule kinetics on a substrate during film deposition. However, the perfluorination of the side-chain substituents strongly enhances the shielding effect of the perylene diimide backbones. The side chains influence the growth in the following aspects (illustrated in Figure 8.1):

- Both PDIR-CN_2 and PDIF-CN_2 films are less ordered when deposited at RT in comparison with DIP or PEN. However, PDIR-CN_2 maintains weak crystallinity (RT-phase) whereas PDIF-CN_2 is nearly amorphous.
- With increasing substrate temperature, the molecular diffusion is enhanced allowing molecules to access the more energetically favored but kinetically limited packings. Thus, PDIR-CN_2 nucleates in a new HT-phase with two molecules per unit cell at T_{sub} above 120 °C. Crystallization of PDIF-CN_2 is observed at T_{sub} above 110 °C.
- The change of the optical properties upon dimerization is prominent enough so that one can associate it with different growth stages.
- Formation of the crystal phases is not instantaneous and occurs within a molecular aggregate. The structural transition is thickness- and temperature-dependent.
- A good long-range order along the vertical axis in the HT films allows one to quantify the difference in the electron density between the molecules.
- The dramatic difference in the optical properties between both materials in crystalline thin films, weakly ordered thin films, and solutions originates from environmental effects such as dipole-dipole or solvent-monomer interaction.

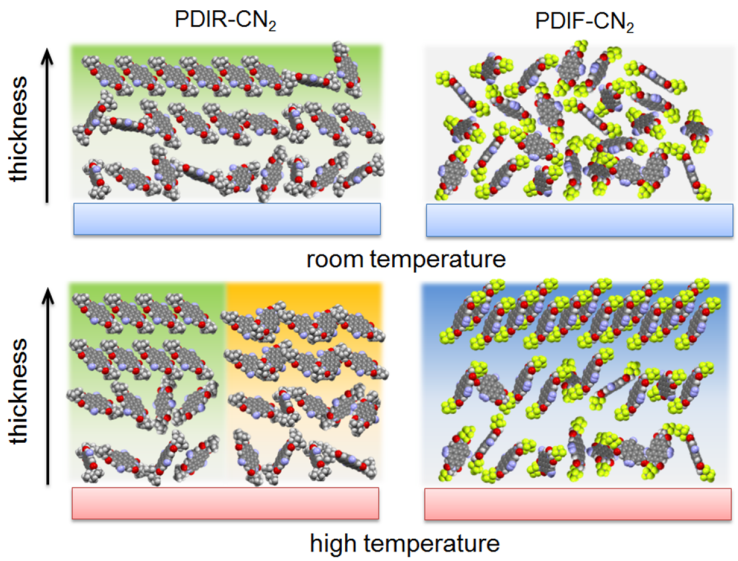


Figure 8.1. Sketch demonstrating thickness- and temperature-dependent growth of PDIR-CN_2 and PDIF-CN_2 thin films by OMBD.

- Environmental effects such as polarization lead to the energy levels shift downwards in thin films of the partially fluorinated compound but are irrelevant when the monomers are considered.

The conclusions on the acceptor materials are important for the interpretation of the results on *D*/*A* mixed films, although they are also valuable as an independent study of n-type small molecule OSCs.

8.2 Results on CT Complex Formation in DIP:PDIR-CN_2

Both donor and acceptor components are sterically compatible and therefore intermix well during co-evaporation. The system showcases the formation of a weak CT complex. The term "weak" is used to distinguish it from the case of a "strong" CT complex with hybridized (shared) orbitals usually observed for *D*/*A* couples where the LUMO level of an acceptor is at least not higher than the HOMO level of a donor. The following key points can be used to sum up the results of Chapter 6:

- Due to *D*/*A* bonding intermolecular interaction a tendency of PDIR-CN_2 molecules for a reorientation towards more standing up-right DIP molecules is found.
- The mixed *D*/*A* films do not exhibit a long-range structural in-plane order. However, a preferred face-to-face stacking is observed.
- In the ground electronic state, a moderate (less than 0.2 electron) ground state CT is observed by changes in the FTIR spectrum. The ground state interactions also lead to the HOMO level alignment between DIP and PDIR-CN_2.

- Under excitation a pronounced complex CT absorption band appears in the NIR energy range. The resulting spectrum in the UV/Vis does not resemble the spectra of the single components.
- The singlet exciton emission is fully quenched in the equimolar blends radiative recombination passes through the two lowest CT states.
- All CT characteristic features are observed predominantly along the in-plane direction i.e. perpendicular to the molecular π-systems (Figure 8.2) demonstrating that the sufficient molecular orbital overlap is required for the CT.
- The intimate intermixting with low crystallinity and bound CT states causes high exciton self-trapping suppressing the charge carrier mobility and decreasing overall device performance.

The bottom line is that the CT mechanism and properties have to be considered in close conjunction with the thin film morphology and structure.

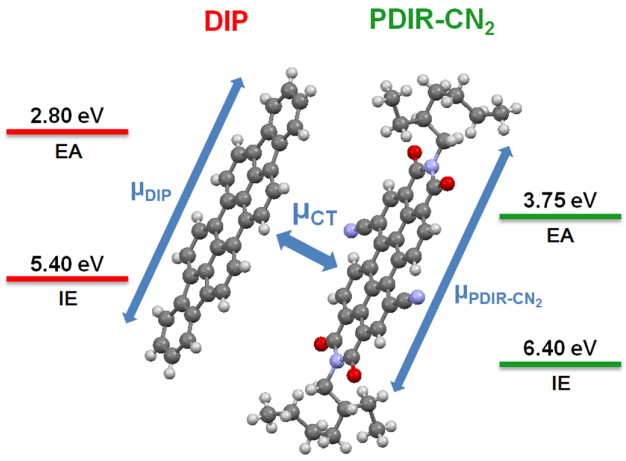


Figure 8.2. Schematic of the CT complex between DIP and PDIR-CN_2 molecules. The energy levels of PDIR-CN_2 are shifted towards those of DIP. The blue arrow in the center depicts the orientation of the CT transition perpendicular to the stacking direction.

8.3 Overview of Four *D*/*A* Systems

In Chapter 7 the compatibility and the ability to form a CT complex of different donors (DIP, PEN) and acceptors (PDIR-CN_2, PDIF-CN_2) are investigated. The sterical, structural, and energetical factors are analyzed. The main outcoming ideas can be summarized as following:

- PDI acceptors reveal better structural compatibility with perylene-based DIP than with PEN.
- The binding energy in the context of intermolecular interactions is a crucial parameter determining the possible mixing scenarios.

- The side chains of the PDI acceptors strongly influence their intermolecular binding interaction within the films and, as a consequence, their miscibility with the donor molecules.
- In the phase-separating system (PEN:PDIR-CN_2) no evidences of intermolecular coupling between *D* and *A* species are observed (Figure 8.3).
- The electrostatic component between *D* and *A* molecules plays an important role in the energy balance. Therefore, the 1D *D*/*A* face-centered stacking is preferred. This is hardly achievable between molecules of the same type.
- The oscillation strength of the optical CT features strongly correlates with the co-crystal quality, which can be controlled by the deposition temperature and the degree of the intermolecular attractive interaction.
- Fluorination of the side chains in the PDIs leads to a shift of the measured IE and EA due to molecule polarization, however their frontier orbitals are not necessarily affected. Due to the fact that the CT transition is anisotropic its energy does not change significantly when replacing the acceptor, since the aromatic core stays the same (Figure 8.3).
- However, replacement of the DIP donor with PEN leads to the corresponding change in the CT energy.

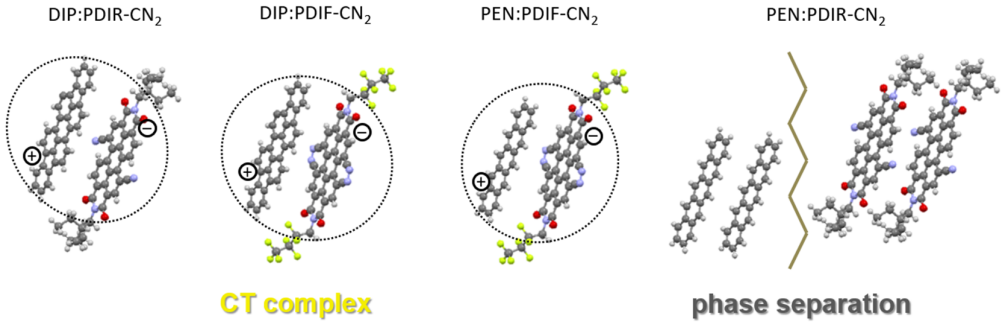


Figure 8.3. CT complex formation is observed for DIP:PDIR-CN_2, DIP:PDIF-CN_2, and PEN:PDIF-CN_2, whereas PEN and PDIR-CN_2 phase separate.

8.4 Outlook

The results are not only helpful for future engineering of well-performing organic n-type active layers and *D*/*A* heterojunctions with desirable characteristics, but also contribute to a fundamental understanding of condensed state properties of organic small molecule semiconductor materials. The following directions for future projects can be considered:

- For a better understanding of the electronic structure of the CT complexes, DFT can be used to calculate the 1:1 spectra of DIP:PDIR-CN_2, DIP:PDIF-CN_2, and PEN:PDIF-CN_2 [189].

- A FTIR setup can be combined with a UV/Vis light source which will allow recording of changes in the IR spectra of molecules in their excited states.
- The exciton diffusion length within domains of the mixed and pure phases can be determined by means of TRPL [284].
- The difference in the binding energies in the pristine and blended films can be quantified by thermal desorption spectroscopy [282].
- Based on the obtained structural data the corresponding solar cells can be produced in order to correlate the performance with the film morphology and composition.
- PEN is known for singlet fission effect and its ability to generate two triplet excitons instead of one singlet exciton using a photon of the same energy [285,286]. Using an acceptor material with a properly matching energy gap one can study CT via triplet states.
- Different aspects of nucleation and phase separation processes in two-component (*D*/*A*) systems and their influence on the resulting device performance have been analyzed theoretically [280]. One could experimentally compare the simulated results for real polymer/polymer, polymer/small molecule, small molecule/small molecule systems. The project will benefit from real-time synchrotron experiments.

APPENDIX A

Additional Information for Chapter 5

Figure A.1 shows the full range *q*-map of the PDIF-CN_2 at RT exhibiting a weak and broad scattering feature in the out-of-plane direction around 1.2 Å.

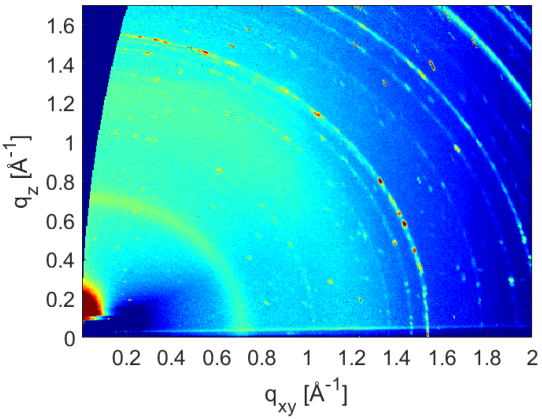


Figure A.1. Reciprocal space map of PDIF-CN_2 at RT. The diffraction ring at 0.7 Å^{-1} is attributed to a kapton window.

The optical absorption spectra of PDIR-CN_2 at 140 °C were fitted with a doubled number of Gaussians that confirms the suggested Davydov splitting of the molecular electronic states (Figure A.2).

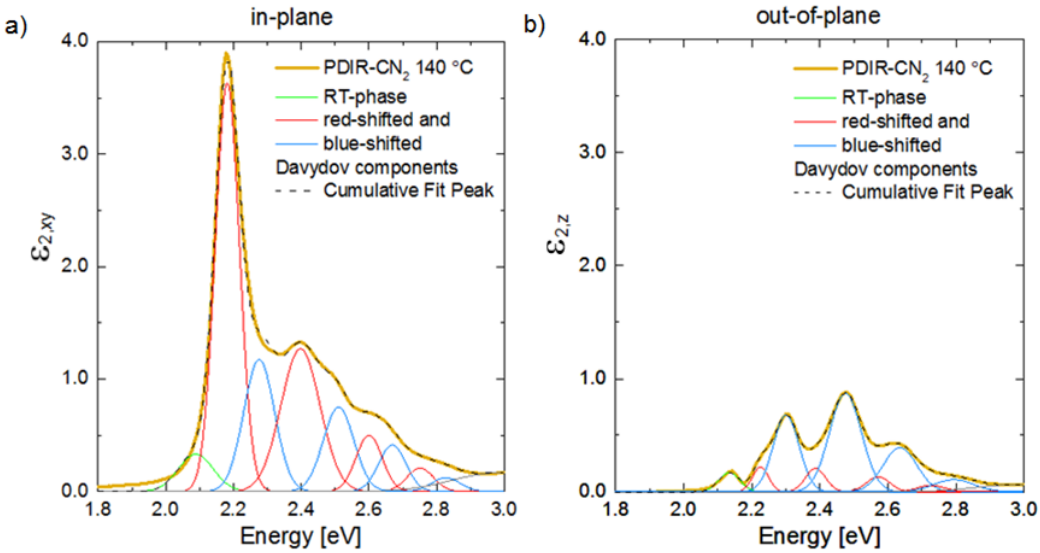


Figure A.2. Exemplary fit with Gaussians of the in-plane and out-of-plane components of the dielectric function of PDIR-CN_2 at 140 °C in Figure 5.8a. Red and blue colors are used for the low and high energy Davydov components.

APPENDIX B

Additional Information for Chapter 6

AFM images (1×1 μm) of the studied samples are shown in Figure B.1 with corresponding surface profiles. Clear molecular terraces are visible only for DIP. All mixtures reveal very smooth surfaces, although 1:1 is rougher than non-equimolar samples.

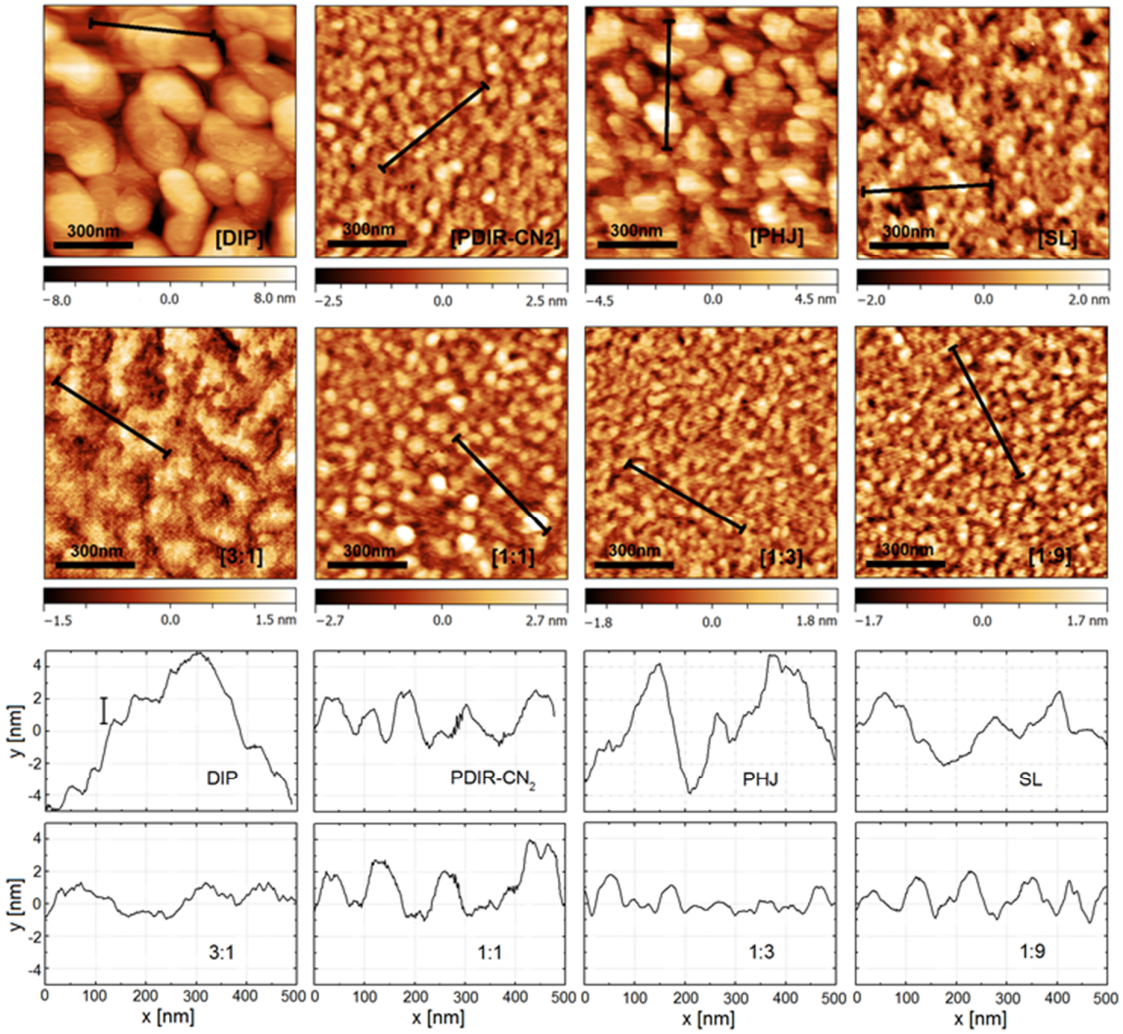


Figure B.1. AFM images from Figure 6.1 with surface profiles.

GIXD spectra of heterostructures (Figure B.2) reveal only features of pristine materials.

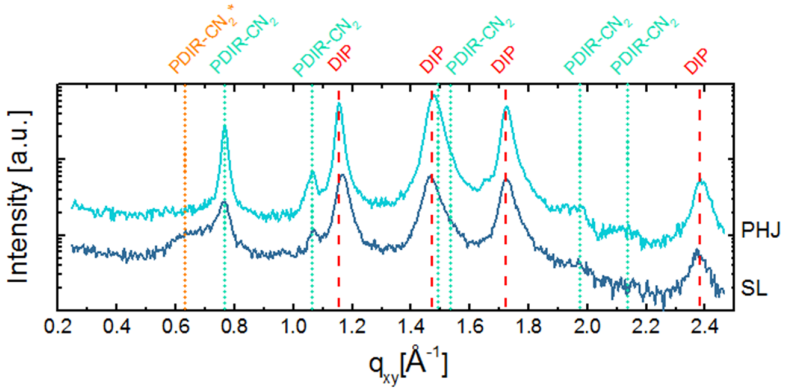


Figure B.2. GIXD scans of PHJ and SL.

Figure B.3 shows photoluminescence transients recorded for pristine films of DIP and PDIR-CN_2 and their blends at 2 temperatures. The corresponding $1/e$-decay times were extracted by monoexponential fits and are plotted as a function of temperature in the insets.

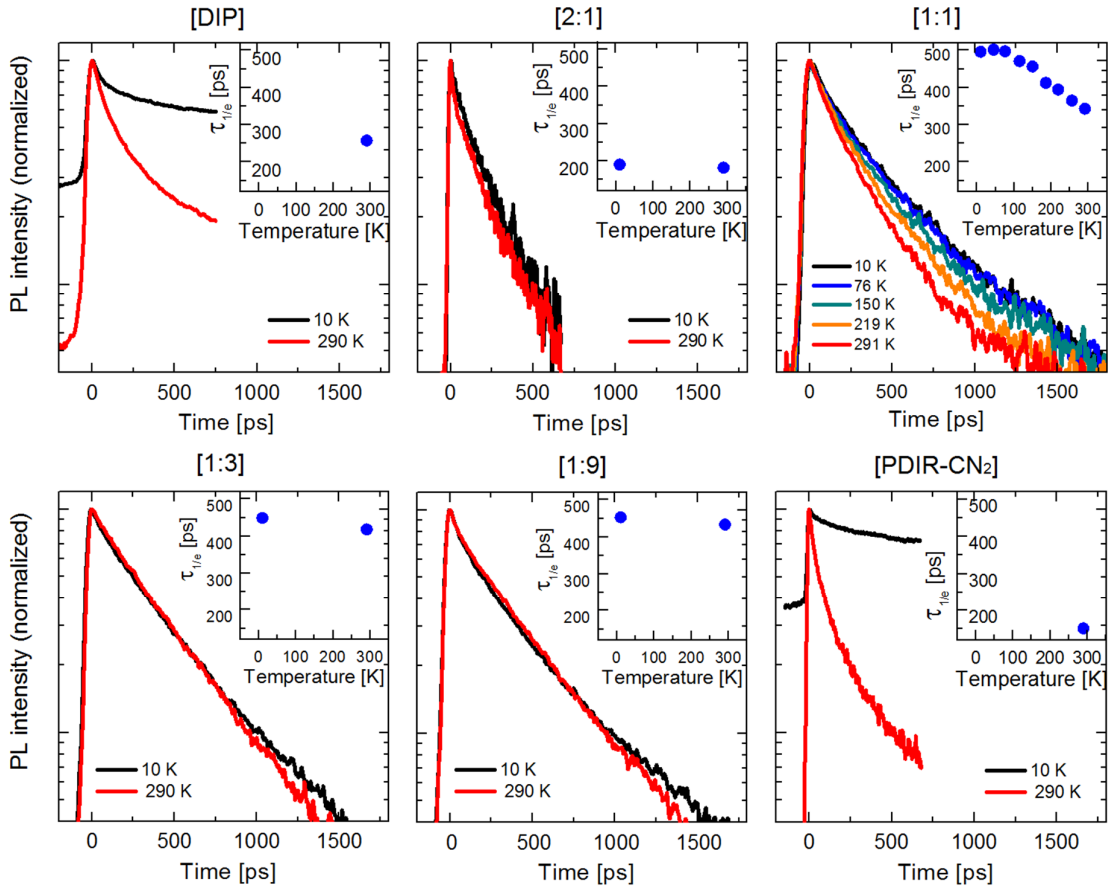


Figure B.3. Temperature dependent PL transients. Insets show lifetimes τ versus measurement temperature, τ of pristine DIP and PDIR-CN_2 measured at 10 K Å exceed 12.5 ns and therefore are not shown in the plots.

At low temperatures, the average decay time of the pristine films is very long (> 12.5 ns). Therefore, there is a signal contribution at negative delay times. CT-decay of 1:1 blend is faster at RT and slower at 10 K in comparison to PDIR-CN_2-rich blends. No temperature dependence of the PL dynamics in the non-stoichiometric blends is observed.

Ellipsometry fit result for mixed films is presented in Figure B.4. Both in-plane (Figure B.4a, similar to the optical absorption result) and out-of-plane (Figure B.4b) components of the extinction coefficient are consistent with the gradual structural transition from standing up-right DIP molecules to tilted PDIR-CN_2 molecules through composition changes. CT bands at 1.4-2.0 eV are visible only for the in-plane component.

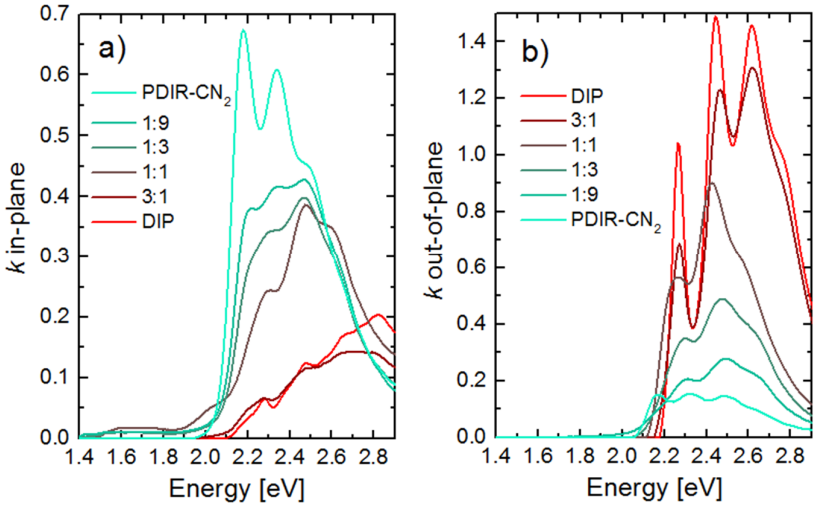


Figure B.4. Extinction coefficient *k* evaluated from ellipsometry: (a) in-plane component (parallel to the sample surface) and (b) out-of-plane component (normal to the sample surface).

APPENDIX C

Additional Information for Chapter 7

Figure C.1 contains PL spectra of DIP:PDIF-CN_2 mixed films deposited at RT. Full quenching of the singlet exciton emission from the neat donor and acceptor moieties is observed not only for the 1:1 film but also for the non-equimolar mixing ratios. The finding together with the weakly ordered thin film structure with no visible phase separation (Figure 7.2b) demonstrates a high degree of intermixing supporting the corresponding sketch in Figure 8.3 (upper row). Even in the DIP-dominating film no pure crystalline DIP domains are preserved.

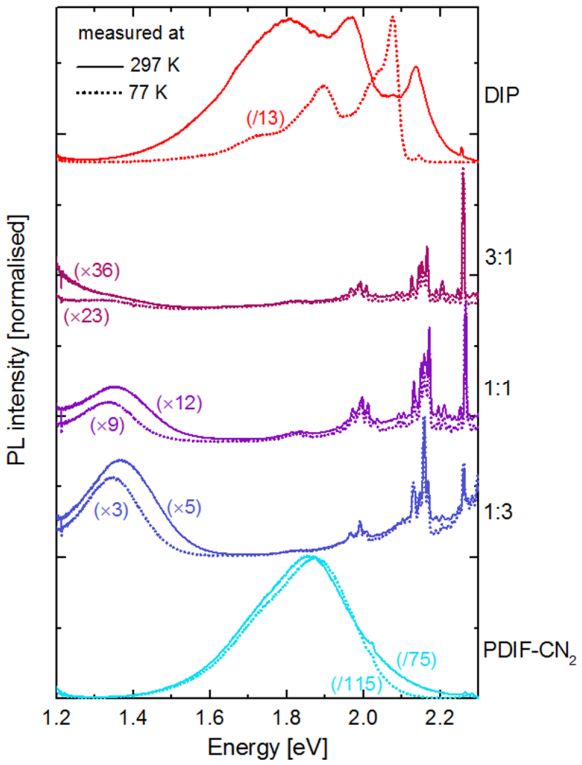


Figure C.1. Photoluminescence spectra of DIP:PDIF-CN_2 grown at RT recorded at 297 K (solid) and 77 K (dotted). All intensities are normalized to the donor. An intensity increase at 1.2 eV is a background due to the instrument limit.

List of Abbreviations

1(2,3)D	One-(two-, three-)dimensional
4T	Quaterthiophene
6T	α-sexithiophene
A	Acceptor; active area
A^*	Excited acceptor
A^-	Ionized acceptor
α_c	Critical angle
C_{60}	Fullerene
D	Donor
D^*	Excited donor
D^+	Ionized acceptor
d	Thickness; lattice spacing
d_{ox}	Oxide thickness
δ	Charge degree
$(\Delta)E_A$	Acceptor energy gap
$(\Delta)E^{CPX}$	Splitting energy in charge transfer complex
$(\Delta)E_D$	Donor energy gap
$(\Delta)E_{DA}$	Energy gap between donor and acceptor energy levels
$\Delta E_{H,H}$	HOMO level offset
$(\Delta)E_{opt}$	Optical gap
ΔF_{mix}	Free energy of mixing
$\Delta\Phi$	Work function shift
E	Energy
E_{el}	Electronic energy
E_{EXC}	Excitation energy
E_n	Nuclear energy
E_{rot}	Rotational energy
E_{CT}	Charge transfer state energy
E_{Stokes}	Stokes shift
E_{vac}	Vacuum energy level
E_{vib}	Vibrational energy
ε	Dielectric function
η	Solar cell efficiency
I	Intensity
$I_{f,i}$	Emission
j-V	Current density - voltage
j_{sc}	Short circuit current
K	Scherrer´s constant

k	Rate constant; wave vector; extinction coefficient
k_B	Boltzmann constant
L	Quantum angular momentum vector
L_D	Diffusion length
l_s	Coherently scattering island size
λ	Wavelength
λ_0	Reorganization energy
λ^2	Huang-Rhys parameter
μ	Transition dipole moment
N	Number
P	Degree of polarization
q	Scattering vector; elementary charge
$q\Delta V_{OC}$	Energy loss
Q_e	Ground state nuclear coordinate
Q'_e	Excited state nuclear coordinate
R	Reflectivity
r	Distance
ρ_e	Electron density
S	Spin; Huang-Rhys parameter
$S_{1..n}$	Singlet states
S_{01}	Overlap integral
σ	Roughness
σ_{dark}	Electrical conductivity in dark
σ_i	Absorption
σ_{photo}	Electrical conductivity under illumination
σ_{RMS}	Root mean square roughness
T	Temperature
$T_{1..n}$	Triplet states
T_{sub}	Substrate temperature
τ	(Life)time
V	Transfer integral; volume
V_{OC}	Open circuit voltage
W	Exciton bandwidth
W_{AB}	Interaction Energy
ω_0	Nuclei reorganization energy
x	Concentration
χ	Interparticle interaction parameter
ψ	Wave function
AFM	Atomic force microscopy
AOI	Angle of incidence
BCP	Bathocuproine
BHJ	Bulk heterojunction
CCD	Charge-coupled device
CS	Charge separation

CT	Charge transfer
DBP	Tetra-phenyldibenzoperiflanthene
DFH-*n*Tc	Diperfluorohexylthiophene
DFT	Density functional theory
DIP	Diindenoperylene
DRS	Differential reflectance spectroscopy
DS	Davydov splitting
EA	Electron affinity
EL	Electroluminescence
EMA	Effective medium approximation
F_4-TCNQ	2,3,5,6-tetrafluoro-7,7,8,8-tetracyanoquinodimethane
F_{16}CoPc	Perfluorinated cobalt phthalocyanine
FE	Frenkel exciton
FF	Fill factor
FTIR	Fourier transform infrared
FWHM	Full width at half-maximum
GIXD	Grazing incidence X-ray diffraction
GS	Ground state
HIL	Hole injection layer
HOMO	Highest occupied molecular orbital
HOPG	Highly oriented pyrolytic graphite
HT	High temperature
IC	Internal conversion
IE	Ionization energy
IPCE	Incident photon-to-current efficiency
IR	Infrared
ISC	Intersystem Crossing
ITO	Indium tin oxide
LCAO	Linear combination of atomic orbitals
LDC	Lower Davydov component
LUMO	Lowest unoccupied molecular orbital
ML	Monolayer
MO	Molecular orbital
NEXAFS	Near-edge X-ray absorption fine structure
NIR	Near infrared
NPD	N,N'-bis(1-naphthyl)-N,N'-diphenyl-1,1'-biphenyl-4,4'-diamine
OFET	Organic field-effect transistor
(O)LED	Light-emitting diode
OMBD	Organic molecular beam deposition
OPV	Organic photovoltaic
OSC	Organic semiconductor
PDI	Perylene diimide derivative
PDI8-CN_2	N,N′-bis(n-octyl)-dicyanoperylene-3,4:9,10-bis(dicarboximide)

PDIR-CN_2	N,N′-bis-(2-ethylhexyl)-1,7-dicyanoperylene-3,4:9,10-bis(dicarboxyimide)
PDIF-CN_2	N,N′-1H,1H-perfluorobutyl-dicyanoperylene-3,4:9,10-bis(dicarboxyimide)
PEN	Pentacene
PHJ	Planar heterojunction
PIC	Picene
PL	Photoluminescence
PM-HJ	Planar-mixed heterojunction
PTCDI-C_8	N,N′-dioctyl-3,4,9,10-perylene tetracarboxylicdiimide
QCM	Quartz crystal microbalance
RT	Room temperature
SL	Superlattice
SLD	Scattering length density
TDM	Transition dipole moment
TMP	Tetramethoxypyrene
TRPL	Time-resolved photoluminescence
UDC	Upper Davydov component
UHV	Ultra-high vacuum
UPS	Ultraviolet photoelectron spectroscopy
UV	Ultraviolet
VASE	Variable angle spectroscopic ellipsometry
VB	Valence bond
Vis	Visible
WF	Work function
XRD	X-ray diffraction
XRR	X-ray reflectivity
ZCl	Zinc chlorodipyrrin

BIBLIOGRAPHY

[1] V. Belova, B. Wagner, B. Reisz, C. Zeiser, G. Duva, J. Rozbořil, J. Novák, A. Gerlach, A. Hinderhofer, and F. Schreiber, J. Phys. Chem. C. **122**, 8589–8601 (2018): *Real-Time Structural and Optical Study of Growth and Packing Behavior of Perylene Diimide Derivative Thin Films: The Influence of Side-Chain Modification*.

[2] V. Belova, P. Beyer, E. Meister, T. Linderl, M.-U. Halbich, M. Gerhard, S. Schmidt, T. Zechel, T. Meisel, A. V Generalov, A.S. Anselmo, R. Scholz, O. Konovalov, A. Gerlach, M. Koch, A. Hinderhofer, A. Opitz, W. Brütting, and F. Schreiber, J. Am. Chem. Soc. **139**, 8474–8486 (2017): *Evidence for Anisotropic Electronic Coupling of Charge Transfer States in Weakly Interacting Organic Semiconductor Mixtures*.

[3] G. Witte, and C. Wöll, Phys. Status Solidi. **510**, 497–510 (2008): *Molecular beam deposition and characterization of thin organic films on metals for applications in organic electronics*.

[4] A. Ringk, W.S.C. Roelofs, E.C.P. Smits, C. Van Der Marel, I. Salzmann, A. Neuhold, G.H. Gelinck, R. Resel, D.M. De Leeuw, and P. Strohriegl, Org. Electron. **14**, 1297–1304 (2013): *n-Type self-assembled monolayer field-effect transistors for flexible organic electronics*.

[5] F. Liscio, C. Albonetti, K. Broch, A. Shehu, S.D. Quiroga, L. Ferlauto, C. Frank, S. Kowarik, R. Nervo, A. Gerlach, and S. Milita, **2**, 1257–1264 (2013): *Molecular Reorganization in Organic Field-Effect Transistors and Its Effect on Two-Dimensional Charge Transport Pathways*.

[6] J.E. Anthony, Chem. Mater. **23**, 583–590 (2011): *Small-Molecule, Nonfullerene Acceptors for Polymer Bulk Heterojunction Organic Photovoltaics*.

[7] U. Hörmann, C. Lorch, A. Hinderhofer, A. Gerlach, M. Gruber, J. Kraus, B. Sykora, S. Grob, T. Linderl, A. Wilke, A. Opitz, R. Hansson, A. So, Y. Ozawa, Y. Nakayama, H. Ishii, N. Koch, E. Moons, F. Schreiber, and W. Brütting, J. Phys. Chem. C. **118**, 26462–26470 (2014): *Voc from a Morphology Point of View: the Influence of Molecular Orientation on the Open Circuit Voltage of Organic Planar Heterojunction Solar Cells*.

[8] A. Wilke, J. Endres, U. Hörmann, J. Niederhausen, R. Schlesinger, J. Frisch, P. Amsalem, J. Wagner, M. Gruber, A. Opitz, A. Vollmer, W. Brütting, A. Kahn, and N. Koch, Appl. Phys. Lett. **101**, 233301 (2012): *Correlation between interface energetics and open circuit voltage in organic photovoltaic cells*.

[9] R.H. Friend, R.W. Gymer, A.B. Holmes, J.H. Burroughes, R.N. Marks, C. Taliani, D.D.C. Bradley, M. Lo, W.R. Salaneck, D.A. Dos Santos, J.L. Bredas, M. Lögdlund, and W.R. Salaneck, Nature. **397**, 121–128 (1999): *Electroluminescence in conjugated polymers*.

[10] S.B. Heidenhain, Y. Sakamoto, T. Suzuki, A. Miura, H. Fujikawa, T. Mori, S. Tokito, and Y. Taga, J. Am. Chem. Soc. **122**, 10240–10241 (2000): *Perfluorinated Oligo(p-Phenylene)s: Efficient n-Type Semiconductors for Organic Light-Emitting Diodes*.

[11] C.J. Brabec, Sol. Energy Mater. Sol. Cells. **83**, 273–292 (2004): *Organic photovoltaics: technology and market*.

[12] Y. Yamaguchi, J. Chem. Phys. **122**, 184702 (2005): *Effects of fluorination on electronic and excited states of fused zinc oligoporphyrins*.

[13] F. Babudri, G.M. Farinola, F. Naso, and R. Ragni, Chem. Commun. **10**, 1003–1022 (2007): *Fluorinated organic materials for electronic and optoelectronic applications: the role of the fluorine atom*.

[14] J.S. Reddy, T. Kale, G. Balaji, A. Chandrasekaran, and S. Thayumanavan, J. Phys. Chem. Lett. **2**, 648–654 (2011): *Cyclopentadithiophene-Based Organic Semiconductors: Effect of Fluorinated Substituents on Electrochemical and Charge Transport Properties*.

[15] A. Facchetti, M. Mushrush, H.E. Katz, and T.J. Marks, Adv. Mater. **15**, 33–38 (2003): *n-Type Building Blocks for Organic Electronics: A Homologous Family of Fluorocarbon-Substituted Thiophene Oligomes with High Carrier Mobility*.

[16] Y. Sakamoto, T. Suzuki, M. Kobayashi, Y. Gao, Y. Fukai, Y. Inoue, F. Sato, and S. Tokito, J. Am. Chem. Soc. **126**, 8138–8140 (2004): *Perfluoropentacene: High-Performance p-n Junctions and Complementary Circuits with Pentacene*.

[17] S. Subramanian, S.K. Park, S.R. Parkin, V. Podzorov, T.N. Jackson, and J.E. Anthony, J. Am. Chem. Soc. **130**, 2706–2707 (2008): *Chromophore Fluorination Enhances Crystallization and Stability of Soluble Anthradithiophene Semiconductors*.

[18] S. Uttiya, L. Raimondo, M. Campione, L. Miozzo, A. Yassar, M. Moret, E. Fumagalli, A. Borghesi, and A. Sassella, Synth. Met. **161**, 2603–2606 (2012): *Stability to photo-oxidation of rubrene and fluorine-substituted rubrene*.

[19] F. Anger, T. Breuer, A. Ruff, M. Klues, R. Scholz, S. Ludwigs, G. Witte, and F. Schreiber, **120**, 5515–5522 (2016): *Enhanced Stability of Rubrene against Oxidation by Partial and Complete Fluorination*.

[20] F. Ponzini, R. Zagha, K. Hardcastle, and J.S. Siegel, Angew. Chem. Int. Ed. **39**, 2323–2325 (2000): *Phenyl/Pentafluorophenyl Interactions and the Generation of Ordered Mixed Crystals: sym-Triphenethynylbenzene and sym-Tris(perfluorophenethynyl)benzene*.

[21] J.C. Collings, K.P. Roscoe, R.L. Thomas, A.S. Batsanov, L.M. Stimson, J.A.K. Howard, and T.B. Marder, New J. Chem. **25**, 1410–1417 (2001): *Arene-perfluoroarene interactions in crystal engineering. Part 3. Single-crystal structures of 1 : 1 complexes of octafluoronaphthalene with fused-ring polyaromatic hydrocarbons*.

[22] M. Fourmigue, and P. Batail, Chem. Rev. **104**, 5379–5418 (2004): *Activation of Hydrogen- and Halogen-Bonding Interactions in Tetrathiafulvalene-Based Crystalline Molecular Conductors*.

[23] R. Taylor, Cryst. Growth Des. **16**, 4165–4168 (2016): *It Isn't, It Is: The C–H···X (X = O, N, F, Cl) Interaction Really Is Significant in Crystal Packing*.

[24] J.H. Wilhams, Acc. Chem. Res. **26**, 593–598 (1993): *The Molecular Electric Quadrupole Moment and Solid-State Architecture*.

[25] A. Nangia, J. Chem. Sci. **122**, 295–310 (2010): *Supramolecular chemistry and crystal engineering*.

[26] W.A. Ogden, S. Ghosh, M.J. Bruzek, K.A. Mcgarry, L. Balhorn, V. Young, L.J. Purvis, S.E. Wegwerth, Z. Zhang, N.A. Serratore, C.J. Cramer, L. Gagliardi, and C.J. Douglas, Cryst. Growth Des. **17**, 643–658 (2017): *Partial Fluorination as a Strategy for Crystal Engineering of Rubrene Derivatives*.

[27] M.-M. Begona, and J. Gierschner, J. Phys. Chem. Lett. **8**, 91–101 (2017): *"Though It Be but Little, It Is Fierce": Excited State Engineering of Conjugated Organic Materials by Fluorination*.

[28] J.-H. Dou, Y.-Q. Zheng, Z.-F. Yao, Z.-A. Yu, T. Lei, X. Shen, X.-Y. Luo, J. Sun, S.-D. Zhang, Y.-F. Ding, G. Han, Y. Yi, J.-Y. Wang, and J. Pei, J. Am. Chem. Soc. **137**, 15947–15956 (2015): *Fine-Tuning of Crystal Packing and Charge Transport Properties of BDOPV Derivatives through Fluorine Substitution*.

[29] Y. Shao, G.-Z. Yin, X. Ren, X. Zhang, J. Wang, K. Guo, X. Li, C. Wesdemiotis, W.-B. Zhang, S. Yang, M. Zhu, and B. Sun, RSC Adv. **7**, 6530–6537 (2017): *Engineering p–p interactions for enhanced photoluminescent properties: unique discrete dimeric packing of perylene diimides*.

[30] S. Ghosh, X.-Q. Li, V. Stepanenko, and F. Würthner, Chem. Eur. J. **14**, 11343–11357 (2008): *Control of H- and J-Type p Stacking by Peripheral Alkyl Chains and Self-Sorting Phenomena in Perylene Bisimide Homo- and Heteroaggregates*.

[31] K. Balakrishnan, A. Datar, T. Naddo, J. Huang, R. Oitker, M. Yen, J. Zhao, and L. Zang, J. Am. Chem. Soc. **128**, 7390–7398 (2006): *Effect of Side-Chain Substituents on Self-Assembly of Perylene Diimide Molecules: Morphology Control*.

[32] S. Vijayalakshmi, A. Föhlich, P.S. Kirchmann, F. Hennies, A. Pietzsch, M. Nagasono, and W. Wurth, Surf. Sci. **600**, 4972–4977 (2006): *Bond polarization and image-potential screening in adsorbed C6F6 on Cu(111)*.

[33] S.L. Wong, H. Huang, Y.L. Huang, Y.Z. Wang, X.Y. Gao, T. Suzuki, W. Chen, and A.T.S. Wee, J. Phys. Chem. C. **114**, 9356–9361 (2010): *Effect of Fluorination on the Molecular Packing of Perfluoropentacene and Pentacene Ultrathin Films on Ag (111)*.

[34] H. Jiang, P. Hu, J. Ye, Y. Li, X. Zhang, R. Li, H. Dong, W. Hu, and C. Kloc, Adv. Mater. **29**, 1605053 (2017): *Molecular Crystal Engineering: Tuning Organic Semiconductor from p-type to n-type by Adjusting Their Substitutional Symmetry*.

[35] R.R. Lunt, J.B. Benziger, and S.R. Forrest, Adv. Mater. **22**, 1233–1236 (2010): *Relationship between Crystalline Order and Exciton Diffusion Length in Molecular Organic Semiconductors*.

[36] Y. Geng, H.-B. Li, S.-X. Wu, and Z.-M. Su, J. Mater. Chem. **22**, 20840–20851 (2012): *The interplay of intermolecular interactions, packing motifs and electron transport properties in perylene diimide related materials: a theoretical perspective*.

[37] M. Klues, A. Rinn, K. Harms, S. Chatterjee, and G. Witte, Cryst. Growth Des. **15**, 5495–5504 (2015): *Polymorph-Selective Preparation and Structural Characterization of Perylene Single Crystals*.

[38] K. Vasseur, C. Rolin, S. Vandezande, K. Temst, L. Froyen, and P. Heremans, J. Phys. Chem. C. **114**, 2730–2737 (2010): *A Growth and Morphology Study of Organic Vapor Phase Deposited Perylene Diimide Thin Films for Transistor Applications*.

[39] J. Puigdollers, M. Della Pirriera, A. Marsal, A. Orpella, S. Cheylan, C. Voz, and R. Alcubilla, Thin Solid Films. **517**, 6271–6274 (2009): *N-type PTCDI–C13H27 thin-film transistors deposited at different substrate temperature*.

[40] C.W. Tang, Appl. Phys. Lett. **48**, 183–185 (1986): *Two-layer organic photovoltaic cell*.

[41] J.-L. Brédas, J.E. Norton, J. Cornil, and V. Coropceanu, Acc. Chem. Res. **42**, 1691–1699

(2009): *Molecular Understanding of Organic Solar Cells: The Challenges*.

[42] C.W. Tang, and S.A. VanSlyke, Appl. Phys. Lett. **51**, 913–915 (1987): *Organic electroluminescent diodes*.

[43] R.S. Mulliken, J. Am. Chem. Soc. **74**, 811–824 (1952): *Molecular Compounds and their Spectra. II*.

[44] R.S. Mulliken, J. Phys. Chem. **56**, 801–822 (1952): *Molecular Compounds and theit Spectra. III. The Interaction of Electron Donors and Acceptors*.

[45] K. Vandewal, Annu. Rev. Phys. Chem. **67**, 113–133 (2016): *Interfacial Charge Transfer States in Condensed Phase Systems*.

[46] K. Vandewal, S. Albrecht, E.T. Hoke, K.R. Graham, J. Widmer, J.D. Douglas, M. Schubert, W.R. Mateker, J.T. Bloking, G.F. Burkhard, A. Sellinger, J.M.J. Fréchet, A. Amassian, M.K. Riede, M.D. McGehee, D. Neher, and A. Salleo, Nat. Mater. **13**, 63–68 (2014): *Efficient charge generation by relaxed charge-transfer states at organic interfaces*.

[47] C. Deibe, T. Strobe, and V. Dyakonov, Adv. Mater. **22**, 4097–4111 (2010): *Role of the charge transfer state in organic donor-acceptor solar cells*.

[48] K. Vandewal, K. Tvingstedt, A. Gadisa, O. Inganäs, and J. V. Manca, Phys. Rev. B. **81**, 125204 (2010): *Relating the open-circuit voltage to interface molecular properties of donor:acceptor bulk heterojunction solar cells*.

[49] K. Vandewal, K. Tvingstedt, A. Gadisa, O. Inganäs, and J. V. Manca, Nat. Mater. **8**, 904–909 (2009): *On the origin of the open-circuit voltage of polymer-fullerene solar cells*.

[50] J.J. Benson-Smith, L. Goris, K. Vandewal, K. Haenen, J. V. Manca, D. Vanderzande, D.D.C. Bradley, and J. Nelson, Adv. Funct. Mater. **17**, 451–457 (2007): *Formation of a Ground-State Charge-Transfer Complex in Polyfluorene/[6,6]-Phenyl-C61 Butyric Acid Methyl Ester (PCBM) Blend Films and Its Role in the Function of Polymer/PCBM Solar Cells*.

[51] K. Vandewal, L. Goris, I. Haeldermans, M. Nesládek, and K. Haenen, **516**, 7135–7138 (2008): *Fourier-Transform Photocurrent Spectroscopy for a fast and highly sensitive spectral characterization of organic and hybrid solar cells*.

[52] D.Y. Paraschuk, S.G. Elizarov, A.N. Khodarev, A.N. Shchegolikhin, S.A. Arnautov, and E.M. Nechvolodova, JETP Lett. **81**, 467–470 (2005): *Weak Intermolecular Charge Transfer in the Ground State of a π-Conjugated Polymer Chain*.

[53] I.-W. Hwang, S. Cho, J.Y. Kim, K. Lee, N.E. Coates, D. Moses, and A.J. Heeger, J. Appl. Phys. **104**, 033706 (2008): *Carrier generation and transport in bulk heterojunction films processed with 1,8-octanedithiol as a processing additive*.

[54] B.C.J. Brabec, A. Cravino, D. Meissner, N.S. Sariciftci, T. Fromherz, M.T. Rispens, L. Sanchez, and J.C. Hummelen, Adv. Funct. Mater. **11**, 374–380 (2001): *Origin of the Open Circuit Voltage of Plastic Solar Cells*.

[55] J. Cremer, P. Bäuerle, M.M. Wienk, and R.A.J. Janssen, Chem. Mater. **18**, 5832–5834 (2006): *High Open-Circuit Voltage Poly (ethynylene bithienylene):Fullerene Solar Cells*.

[56] H. Kim, J.Y. Kim, S.H. Park, K. Lee, Y. Jin, J. Kim, and H. Suh, Appl. Phys. Lett. **86**, 183502 (2005): *Electroluminescence in polymer-fullerene photovoltaic cells*.

[57] A.F. Eftaiha, J.-P. Sun, G.I. Hill, and G.C. Welch, J. Mater. Chem. A. **2**, 1201–1213 (2014): *Recent advances of non-fullerene, small molecular acceptors for solution processed bulk heterojunction solar cells.*

[58] C.H. Wu, C.C. Chueh, Y.Y. Xi, H.L. Zhong, G.P. Gao, Z.H. Wang, L.D. Pozzo, T.C. Wen, and A.K.Y. Jen, Adv. Funct. Mater. **25**, 5326–5332 (2015): *Influence of Molecular Geometry of Perylene Diimide Dimers and Polymers on Bulk Heterojunction Morphology Toward High-Performance Nonfullerene Polymer Solar Cells*.

[59] M.C. Scharber, Adv. Mater. **28**, 1994–2001 (2016): *On the Efficiency Limit of Conjugated Polymer:Fullerene-Based Bulk Heterojunction Solar Cells*.

[60] J. Shi, A. Isakova, A. Abudulimu, M. van den Berg, O.K. Kwon, A.J. Meixner, S.Y. Park, D. Zhang, J. Gierschner, and L. Lüer, Energy Environ. Sci. **11**, 211–220 (2018): *Designing high performance all-small molecule solar cells with non-fullerene acceptors: comprehensive studies on photoexcitation dynamics and charge separation kinetics.*

[61] E.B. Isaacs, S. Sharifzadeh, B. Ma, and J.B. Neaton, J. Phys. Chem. Lett. **2**, 2531–2537 (2011): *Relating trends in first-principles electronic structure and open-circuit voltage in organic photovoltaics*.

[62] J. Benduhn, K. Tvingstedt, F. Piersimoni, S. Ullbrich, Y. Fan, M. Tropiano, K.A. McGarry, O. Zeika, M.K. Riede, C.J. Douglas, S. Barlow, S.R. Marder, D. Neher, D. Spoltore, and K. Vandewal, Nat. Energy. **2**, 17053 (2017): *Intrinsic Non-Radiative Voltage Losses in Fullerene-Based Organic Solar Cells*.

[63] M.P. Thekaekara, NASA TR R-531, National Aeronautics and Space Administration, Washington (1970): *The Solar Constant and the Solar Spectrum Measured from a Research Aircraft*.

[64] M. Hallermann, E. Da Como, J. Feldmann, M. Izquierdo, S. Filippone, N. Martín, S. Jüchter, and E. Von Hauff, Appl. Phys. Lett. **97**, 023301 (2010): *Correlation between charge transfer exciton recombination and photocurrent in polymer/fullerene solar cells*.

[65] X.-K. Chen, M.K. Ravva, H. Li, S.M. Ryno, and J.-L. Brédas, Adv. Energy Mater. **6**, 1601325 (2016): *Effect of Molecular Packing and Charge Delocalization on the Nonradiative Recombination of Charge-Transfer States in Organic Solar Cells*.

[66] J. Clark, R. Archer, T. Redding, C. Foden, J. Tant, Y. Geerts, R.H. Friend, and C. Silva, J. Appl. Phys. **103**, 124510 (2008): *Charge recombination in distributed heterostructures of semiconductor discotic and polymeric materials*.

[67] M.J. Kendrick, A. Neunzert, M.M. Payne, B. Purushothaman, B.D. Rose, J.E. Anthony, M.M. Haley, and O. Ostroverkhova, J. Phys. Chem. C. **116**, 18108–18116 (2012): *Formation of the Donor – Acceptor Charge-Transfer Exciton and Its Contribution to Charge Photogeneration and Recombination in Small-Molecule Bulk Heterojunctions*.

[68] M.L. Jones, and E. Jankowski, Mol. Simul. **43**, 756–773 (2017): *Computationally connecting organic photovoltaic performance to atomistic arrangements and bulk morphology*.

[69] Y. Huang, E.J. Kramer, A.J. Heeger, and G.C. Bazan, Chem. Rev. **114**, 7006–7043 (2014): *Bulk Heterojunction Solar Cells: Morphology and Performance Relationships*.

[70] J. Fischer, J. Widmer, H. Kleemann, W. Tress, C. Koerner, M. Riede, K. Vandewal, and K. Leo, J. Appl. Phys. **117**, 045501 (2015): *A charge carrier transport model for donor-acceptor blend layers*.

[71] S. Shoaee, S. Subramaniyan, H. Xin, C. Keiderling, P.S. Tuladhar, F. Jamieson, S.A. Jenekhe, and J.R. Durrant, Adv. Funct. Mater. **23**, 3286–3298 (2013): *Charge Photogeneration for a Series of Thiazolo-Thiazole Donor Polymers Blended with the Fullerene Electron Acceptors PCBM and ICBA*.

[72] A. Zusan, K. Vandewal, B. Allendorf, N.H. Hansen, J. Pflaum, A. Salleo, V. Dyakonov, and C. Deibel, Adv. Energy Mater. **4**, 1400922 (2014): *The Crucial Influence of Fullerene Phases on Photogeneration in Organic Bulk Heterojunction Solar Cells*.

[73] S. Kraner, R. Scholz, C. Koerner, and K. Leo, J. Phys. Chem. C. **119**, 22820–22825 (2015): *Design Proposals for Organic Materials Exhibiting a Low Exciton Binding Energy*.

[74] A. Opitz, J. Wagner, W. Brütting, A. Hinderhofer, and F. Schreiber, Phys. Status Solidi A. **206**, 2683–2694 (2009): *Molecular semiconductor blends: Mictrostructure, charge carrier transport, and application in photovoltaic cells*.

[75] A. Opitz, J. Wagner, W. Brütting, I. Salzmann, N. Koch, J. Manara, J. Pflaum, A. Hinderhofer, and F. Schreiber, IEEE J. Sel. Top. Quantum Electron. **16**, 1707–1717 (2010): *Charge Separation at Molecular Donor – Acceptor Interfaces: Correlation Between Morphology and Solar Cell Performance*.

[76] P.K. Watkins, A.B. Walker, and G.L.B. Verschoor, Nano Lett. **5**, 1814–1818 (2005): *Dynamical Monte Carlo Modelling of Organic Solar Cells: The Dependence of Internal Quantum Efficiency on Morphology*.

[77] A. Hinderhofer, and F. Schreiber, ChemPhysChem. **13**, 628–643 (2012): *Organic-organic heterostructures: Concepts and applications*.

[78] J.-O. Vogel, I. Salzmann, S. Duhm, M. Oehzelt, J.P. Rabe, and N. Koch, J. Mater. Chem. **20**, 4055–4066 (2010): *Phase-separation and mixing in thin films of co-deposited rod-like conjugated molecules*.

[79] J. Dieterle, K. Broch, H. Frank, G. Duva, T. Storzer, A. Hinderhofer, J. Novák, A. Gerlach, and F. Schreiber, Phys. Status Solidi RRL. **11**, 1600428 (2017): *Delayed phase separation in growth of organic semiconductor blends with limited intermixing*.

[80] J. Dieterle, K. Broch, A. Hinderhofer, H. Frank, J. Novák, A. Gerlach, T. Breuer, R. Banerjee, G. Witte, and F. Schreiber, J. Phys. Chem. C. **119**, 26339–26347 (2015): *Structural Properties of Picene-Perfluoropentacene and Picene-Pentacene Blends: Superlattice Formation versus Limited Intermixing*.

[81] J.P. Reinhardt, A. Hinderhofer, K. Broch, U. Heinemeyer, S. Kowarik, A. Vorobiev, A. Gerlach, and F. Schreiber, J. Phys. Chem. C. **116**, 10917–10923 (2012): *Structural and Optical Properties of Mixed Diindenoperylene–Perfluoropentacene Thin Films*.

[82] J. Bredas, Mater. Horiz. **1**, 17–19 (2014): *Mind the gap!*

[83] T. Linderl, U. Hörmann, S. Beratz, M. Gruber, S. Grob, A. Hofmann, and W. Brütting, J. Opt. **18**, 024007 (2016): *Temperature dependent competition between different recombination channels in organic heterojunction solar cells*.

[84] A.N. Bartynski, S. Grob, T. Linderl, M. Gruber, W. Brütting, and M.E. Thompson, J. Phys. Chem. C. **120**, 19027–19034 (2016): *Organic Solar Cells with Open Circuit Voltage over 1.25 V Employing Tetraphenyldibenzoperiflanthene as the Acceptor*.

[85] A.N. Bartynski, M. Gruber, S. Das, S. Rangan, S. Mollinger, C. Trinh, S.E. Bradforth, K. Vandewal, A. Salleo, R.A. Bartynski, W. Bruetting, and M.E. Thompson, J. Am. Chem. Soc.

137, 5397–5405 (2015): *Symmetry-Breaking Charge Transfer in a Zinc Chlorodipyrrin Acceptor for High Open Circuit Voltage Organic Photovoltaics*.

[86] H. Ulrich, J. Kraus, M. Gruber, C. Schuhmair, T. Linderl, S. Grob, S. Kapfinger, K. Klein, M. Stutzman, H.J. Krenner, and W. Brütting, Phys. Rev. B. **88**, 235307 (2013): *Quantification of energy losses in organic solar cells from temperature-dependent device characteristics*.

[87] M. Aghamohammadi, A. Fernandez, M. Schmidt, A. Perez-Rodriguez, A.R. Goni, J. Fraxedas, G. Sauthier, M. Paradinas, C. Ocal, and E. Barrena, J. Phys. Chem. C. **118**, 14833–14839 (2014): *Influence of the Relative Molecular Orientation on Interfacial Charge-Transfer Excitons at Donor/Acceptor Nanoscale Heterojunctions*.

[88] B. Bernardo, D. Cheyns, B. Verreet, R.D. Schaller, B.P. Rand, and N.C. Giebink, Nat. Commun. **5**, 3245 (2014): *Delocalization and dielectric screening of charge transfer states in organic photovoltaic cells*.

[89] H. Méndez, G. Heimel, S. Winkler, J. Frisch, A. Opitz, K. Sauer, B. Wegner, M. Oehzelt, C. Röthel, S. Duhm, D. Többens, N. Koch, and I. Salzmann, Nat. Commun. **6**, 8560 (2015): *Charge-transfer crystallites as molecular electrical dopants*.

[90] I. Salzmann, G. Heimel, S. Duhm, M. Oehzelt, P. Pingel, B.M. George, A. Schnegg, K. Lips, R.-P. Blum, A. Vollmer, and N. Koch, Phys. Rev. B. **108**, 035502 (2012): *Intermolecular Hybridization Governs Molecular Electrical Doping*.

[91] B. Mahns, O. Kataeva, D. Islamov, S. Hampel, F. Steckel, C. Hess, M. Knupfer, B. Büchner, C. Himcinschi, T. Hahn, R. Renger, and J. Kortus, Cryst. Growth Des. **14**, 1338–1346 (2014): *Crystal Growth, Structure, and Transport Properties of the Charge-Transfer Salt Picene/2,3,5,6-Tetrafluoro-7,7,8,8-tetracyanoquinodimethane*.

[92] C. Deibel, T. Strobel, and V. Dyakonov, Adv. Mater. **22**, 4097–4111 (2010): *Role of the Charge Transfer State in Organic Donor–Acceptor Solar Cells*.

[93] M.L. Tietze, J. Benduhn, P. Pahner, B. Nell, M. Schwarze, H. Kleeman, M. Krammer, K. Zojer, K. Vandewal, and K. Leo, Nat. Commun. **9**, 1182 (2018): *Elementary steps in electrical doping of organic semiconductors*.

[94] G.N. Lewis, J. Am. Chem. Soc. **38**, 762–785 (1916): *The atom and the molecule*.

[95] W. Heitler, and F. London, F. Z. Phys. **44**, 455–472 (1927): *Wechselwirkung neutraler Atome und homöopolare Bindung nach der Quantenmechanik*.

[96] F.A. Carey, and R.J. Sundberg, 4th ed. Kluwer Academic/Plenum Publishers, New York (2000): *Advanced Organic Chemistry. Part A: Structure and Mechanisms*.

[97] P. Jordan, and E. Wigner, Z. Phys. **47**, 631–651 (1928): *Über das Paulische Äquivalenzverbot*.

[98] M. Born, and R. Oppenheimer, Ann. d. Phys. **389**, 457–484 (1927): *Zur Quamtentheorie der Molekeln*.

[99] E. Condon, Phys. Rev. **28**, 1182–1201 (1926): *Theory of intensity distribution in band systems*.

[100] M. De Jong, L. Seijo, A. Meijerink, and F.T. Rabouw, Phys. Chem. Chem Phys. **17**, 16959–16969 (2015): *Resolving the ambiguity in the relation between Stokes shift and Huang–Rhys parameter*.

[101] C. Sutton, C. Risko, and J. Bredas, Chem. Mater. **28**, 3–16 (2016): *Noncovalent Intermolecular Interactions in Organic Electronic Materials: Implications for the Molecular Packing vs Electronic Properties of Acenes*.

[102] F. London, Trans. Faraday Soc. **33**, 8–26 (1937): *The general theory of molecular forces*.

[103] C.A. Hunter, and J.K.M. Sanders, J. Am. Chem. Soc. **112**, 5525–5534 (1990): *The Nature of π-π Interactions*.

[104] M.O. Sinnokrot, and C.D. Sherrill, J. Phys. Chem. A. **110**, 10656–10668 (2006): *High-Accuracy Quantum Mechanical Studies of π-π Interactions in Benzene Dimers*.

[105] S. Grimme, Angew. Chem. Int. Ed. **47**, 3430–3434 (2008): *Do Special Noncovalent p – p Stacking Interactions Really Exist?*

[106] C.R. Martinez, and B.L. Iverson, Chem. Sci. **3**, 2191–2201 (2012): *Rethinking the term "pi-stacking."*

[107] C.D. Sherrill, Acc. Chem. Res. **46**, 1020–1028 (2013): *Energy Component Analysis of π Interactions*.

[108] A.I. Kitaigorodsky, Springer, Berkin, Heidelberg (1984): *Mixed Crystals*.

[109] U. Heinemeyer, R. Scholz, L. Gisslén, M.I. Alonso, J.O. Ossó, M. Garriga, A. Hinderhofer, M. Kytka, S. Kowarik, A. Gerlach, and F. Schreiber, Phys. Rev. B. **78**, 085210 (2008): *Exciton-phonon coupling in diindenoperylene thin films*.

[110] N.J. Hestand, H. Yamagata, B. Xu, D. Sun, Y. Zhong, A.R. Harutyunyan, G. Chen, H. Dai, Y. Rao, and F.C. Spano, J. Phys. Chem. C. **119**, 22137–22147 (2015): *Polarized Absorption in Crystalline Pentacene: Theory vs Experiment*.

[111] J. Dieterle, Ph.D. Thesis, Eberhard Karls Universität Tübingen (2016): *The Influence of Dilution on Structural and Optical Properties of Organic Semiconductors*.

[112] B.-K. An, J. Gierschner, and S.Y. Park, Acc. Chem. Res. **45**, 544–554 (2012): *π-Conjugated Cyanostilbene Derivatives: A Unique Self-Assembly Motif for Molecular Nanostructures with Enhanced Emission and Transport*.

[113] M. Kasha, H.R. Rawls, and M.A. El-Bayoumi, Pure Appl. Chem. **11**, 371–392 (1965): *The exciton model in molecular spectroscopy*.

[114] A. Austin, N.J. Hestand, I.G. Mckendry, C. Zhong, X. Zhu, M.J. Zdilla, F.C. Spano, and J.M. Szarko, J. Phys. Chem. Lett. **8**, 1118–1123 (2017): *Enhanced Davydov Splitting in Crystals of a Perylene Diimide Derivative*.

[115] R.L. Fulton, and M. Gouterman, J. Chem. Phys. **35**, 1059–1071 (1961): *Vibronic Coupling. I. Mathematical Treatment for Two Electronic States*.

[116] A.M. Kelley, J. Chem. Phys. **119**, 3320–3331 (2003): *A multimode vibronic treatment of absorption, resonance Raman, and hyper-Rayleigh scattering of excitonically coupled molecular dimers*.

[117] F.C. Spano, Acc. Chem. Res. **43**, 429–439 (2010): *The Spectral Signatures of Frenkel Polarons in H- and J-Aggregates*.

[118] N.J. Hestand, R. V Kazantsev, A.S. Weingarten, L.C. Palmer, S.I. Stupp, and F.C. Spano, J. Am. Chem. Soc. **138**, 11762–11774 (2016): *Extended-Charge-Transfer Excitons in*

Crystalline Supramolecular Photocatalytic Scaffolds.

[119] S.K. Park, I. Cho, J. Gierschner, J.H. Kim, J.H. Kim, J.E. Kwon, O.K. Kwon, D.R. Whang, J.-H. Park, B.-K. An, and S.Y. Park, Angew. Chem. Int. Ed. **55**, 203–207 (2016): *Stimuli-Responsive Reversible Fluorescence Switching in a Crystalline Donor–Acceptor Mixture Film: Mixed Stack Charge-Transfer Emission versus Segregated Stack Monomer Emission*.

[120] K. Vandewal, S. Albrecht, E.T. Hoke, K.R. Graham, J. Widmer, J.D. Douglas, M. Schubert, W.R. Mateker, J.T. Bloking, G.F. Burkhard, A. Sellinger, J.M.J. Fréchet, A. Amassian, M.K. Riede, M.D. McGehee, D. Neher, and A. Salleo, Nat. Mater. **13**, 63–68 (2014): *Efficient charge generation by relaxed charge-transfer states at organic interfaces*.

[121] F. Schreiber, Phys. Status Solidi. **201**, 1037–1054 (2004): *Organic molecular beam deposition: Growth studies beyond the first monolayer*.

[122] G. Witte, and C. Wöll, J. Mater. Res. **19**, 1889–1916 (2004): *Growth of aromatic molecules on solid substrates for applications in organic electronics*.

[123] S.M. Kowarik, Ph.D. Thesis, Wadham college, Oxford (2006): *Real-time studies of thin film growth of organic semiconductors*.

[124] G. Ehrlich, and F.G. Hudda, J. Chem. Phys. **44**, 1039–1049 (1966): *Atomic View of Surface Self-Diffusion: Tungsten on Tungsten*.

[125] R.L. Schwoebel, and E.J. Shipsey, J. Appl. Phys. **37**, 3682–3686 (1966): *Step Motion on Crystal Surfaces*.

[126] A. Hinderhofer, Ph.D. Thesis, Eberhard Karls Universität Tübingen (2011): *Growth Studies of Organic Heterostructures for Photovoltaic Applications*.

[127] C. Lorch, Ph.D. Thesis, Eberhard Karls Universität Tübingen (2015): *Influence of Morphological and Structural Properties on Organic Photovoltaic Cells*.

[128] L. Ferlauto, Ph.D. Thesis, Université de Strasbourg (2015): *Correlation between structural and electrical properties of organic semiconducting materials*.

[129] M. Björck, and G. Andersson, J. Appl. Cryst. **40**, 1174–1178 (2007): *GenX: an extensible X-ray reflectivity refinement program utilizing differential evolution*.

[130] L.G. Parratt, Phys. Rev. **95**, 359–369 (1954): *Surface studies of solids by total reflection of x-rays*.

[131] A.L. Patterson, Phys. Rev. **56**, 978–982 (1939): *The Scherrer Formula for X-Ray Particle Size Determination*.

[132] M.I. Alonso, M. Garriga, N. Karl, J.O. Osso, and F. Schreiber, Org. Electron. **3**, 23–31 (2002): *Anisotropic optical properties of single crystalline PTCDA studied by spectroscopic ellipsometry*.

[133] U. Heinemeyer, Ph.D. Thesis, Eberhard Karls Universität Tübingen (2009): *Optical properties of organic semiconductor thin films: Static spectra and real-time growth studies*.

[134] J.A. Woollam Co., *WVASE32, Manual*.

[135] D.A.G. Bruggeman, Ann. d. Phys. **416**, 636–664 (1935): *Berechnung verschiedener*

physikalischer Konstanten von heterogenen Substanzen. I. Dielektrizitätskonstanten und Leitfähigkeiten der Mischkörper aus isotropen Substanzen.

[136] B.E.A. Saleh, and M.C. Teich, John Wiley & Sons, Inc., New York (1991): *Fundamentals of photonics*.

[137] J.S. Toll, Phys. Rev. **104**, (1956): *Causality and Dispersion Relation: Logical Foundations*.

[138] A. Brillante, T. Salzillo, R.G. Della, E. Venuti, F. Borgatti, E. Lunedei, F. Liscio, S. Milita, and C. Albonetti, J. Lumin. **187**, 403–409 (2017): *Photoluminescence as a probe of molecular organization in PDI8-CN2 ultra-thin films*.

[139] F. Anger, Ph.D. Thesis, Eberhard Karls Universität Tübingen (2010): *Photoluminescence and Raman spectroscopy of pentacene/perfluoropentacene mixed thin films*.

[140] K. Broch, Ph.D. Thesis, Eberhard Karls Universität Tübingen (2013): *Interplay of Ordering Behavior and Optical Properties in Organic Semiconductor Blends*.

[141] T. Hosokai, A. Gerlach, A. Hinderhofer, C. Frank, G. Ligorio, U. Heinemeyer, A. Vorobiev, and F. Schreiber, Appl. Phys. Lett. **97**, 063301 (2010): *Simultaneous in situ measurements of x-ray reflectivity and optical spectroscopy during organic semiconductor thin film growth*.

[142] K. Broch, A. Gerlach, C. Lorch, J. Dieterle, J. Novák, A. Hinderhofer, and F. Schreiber, J. Chem. Phys. **139**, 174709 (2013): *Structure formation in perfluoropentacene:diindenoperylene blends and its impact on transient effects in the optical properties studied in real-time during growth*.

[143] U. Heinemeyer, K. Broch, A. Hinderhofer, M. Kytka, R. Scholz, A. Gerlach, and F. Schreiber, Phys. Rev. Lett. **104**, 257401 (2010): *Real-Time Changes in the Optical Spectrum of Organic Semiconducting Films and Their Thickness Regimes during Growth*.

[144] H. Proehl, R. Nitsche, T. Dienel, K. Leo, and T. Fritz, Phys. Rev. B. **71**, 165207 (2005): *In situ differential reflectance spectroscopy of thin crystalline films of PTCDA on different substrates*.

[145] J.D.E. McIntyre, and D.E. Aspnes, **24**, 417–434 (1971): *Differential Reflection Spectroscopy of Very Thin Surface Films*.

[146] D. Necás, and P. Klapetek, Cent. Eur. J. Phys. **10**, 181–188 (2012): *Gwyddion: an open-source software for SPM data analysis*.

[147] J. Stöhr, and A. Outka, **36**, 7891–7905 (1987): *Determination of molecular orientations on surfaces from the angular dependence of near-edge x-ray-absorption fine-structure spectra*.

[148] B. Watts, L. Thomsen, and P.C. Dastoor, **151**, 105–120 (2006): *Methods in carbon K-edge NEXAFS : Experiment and analysis*.

[149] B.J. Wagner, M. Gruber, A. Hinderhofer, A. Wilke, B. Bröker, J. Frisch, P. Amsalem, A. Vollmer, A. Opitz, N. Koch, F. Schreiber, and W. Brütting, Adv. Funct. Mater. **20**, 4295–4303 (2010): *High Fill Factor and Open Circuit Voltage in Organic Photovoltaic Cells with Diindenoperylene as Donor Material*.

[150] M. Gruber, M. Rawolle, J. Wagner, D. Magerl, U. Hörmann, J. Perlich, S. V Roth, A. Opitz, F. Schreiber, P. Müller-Buschbaum, and W. Brütting, Adv. Energy Mater. **3**, 1075–1083 (2013): *Correlating Structure and Morphology to Device Performance of Molecular*

Organic Donor–Acceptor Photovoltaic Cells Based on Diindenoperylene (DIP) and C60.

[151] S. Yoo, B. Domercq, and B. Kippelen, Appl. Phys. Lett. **85**, 5427–5429 (2004): *Efficient thin-film organic solar cells based on pentacene/C60 heterojunctions*.

[152] C.D. Dimitrakopoulos, A.R. Brown, and A. Pomp, J. Appl. Phys. **80**, 2501–2508 (1996): *Molecular beam deposited thin films of pentacene for organic field effect transistor applications*.

[153] D. Feili, M. Schuettler, T. Doerge, S. Kammer, and T. Stieglitz, Sensors Actuators A. **120**, 101–109 (2005): *Encapsulation of organic field effect transistors for flexible biomedical microimplants*.

[154] S. Krause, A. Schöll, and E. Umbach, Org. Electron. **14**, 584–590 (2013): *Interplay of geometric and electronic structure in thin films of diindenoperylene on Ag (111)*.

[155] W. Han, H. Yoshida, N. Ueno, and S. Kera, Appl. Phys. Lett. **103**, 123303 (2013): *Electron affinity of pentacene thin film studied by radiation-damage free inverse photoemission spectroscopy*.

[156] R.G. Endres, C.Y. Fong, L.H. Yang, G. Witte, and C. Wöll, Comput. Mater. Sci. **29**, 362–370 (2004): *Structural and electronic properties of pentacene molecule and molecular pentacene solid*.

[157] J. Lee, Appl. Phys. Lett. **103**, 036101 (2016): *Comment on "Investigation of the device instability feature caused by electron trapping in pentacene field effect transistors" [Appl. Phys. Lett. 100, 063306 (2012)]*.

[158] M.A. Heinrich, J. Pflaum, A.K. Tripathi, W. Frey, M.L. Steigerwald, and T. Siegrist, J. Phys. Chem. C. **111**, 18878–18881 (2007): *Enantiotropic Polymorphism in Di-indenoperylene*.

[159] D. Nabok, P. Puschnig, C. Ambrosch-Draxl, O. Werzer, R. Resel, and D.-M. Smilgies, Phys. Rev. B. **76**, 235322 (2007): *Crystal and electronic structures of pentacene thin films from grazing-incidence x-ray diffraction and first-principles calculations*.

[160] R.B. Campbell, and J.M. Robertson, Acta Cryst. **15**, 289–290 (1962): *The crystal structure of hexacene, and a revision of the crystallographic data for tetracene and pentacene*.

[161] C. Piliego, F. Cordella, D. Jarzab, S. Lu, Z. Chen, A. Facchetti, and M.A. Loi, Appl. Phys. A. **95**, 303–308 (2009): *Functionalized perylenes: origin of the enhanced electrical performances*.

[162] J. Kim, S. Han, H. Jeong, H. Jang, S. Baek, J. Hu, M. Lee, B. Choi, and H.S. Lee, ACS Appl. Mater. Interfaces. **9**, 9910–9917 (2017): *Thermal Gradient During Vacuum-Deposition Dramatically Enhances Charge Transport in Organic Semiconductors: Toward High-Performance N-Type Organic Field-Effect Transistors*.

[163] J. Sun, A.D. Hendsbee, A.J. Dobson, G.C. Welch, and I.G. Hill, Org. Electron. **35**, 151–157 (2016): *Perylene diimide based all small-molecule organic solar cells: Impact of branched-alkyl side chains on solubility, photophysics, self-assembly, and photovoltaic parameters*.

[164] C. Huang, S. Barlow, and S.R. Marder, J. Org. Chem. **76**, 2386–2407 (2011): *Perylene-3,4,9,10-tetracarboxylic Acid Diimides: Synthesis, Physical Properties, and Use in Organic Electronics*.

[165] C. Li, and H. Wonneberger, Adv. Mater. **24**, 613–636 (2012): *Perylene Imides for Organic Photovoltaics: Yesterday, Today, and Tomorrow*.

[166] B.A. Jones, A. Facchetti, M.R. Wasielewski, and T.J. Marks, J. Am. Chem. Soc. **129**, 15259–15278 (2007): *Tuning Orbital Energetics in Arylene Diimide Semiconductors. Materials Design for Ambient Stability of n-Type Charge Transport*.

[167] F. Würthner, C.R. Saha-Möller, B. Fimmel, S. Ogi, P. Leowanawat, and D. Schmidt, Chem. Rev. **116**, 962–1052 (2016): *Perylene Bisimide Dye Assemblies as Archetype Functional Supramolecular Materials*.

[168] J. Schill, L. Milroy, J.A.M. Lugger, A.P.H.J. Schenning, and L. Brunsveld, ChemistryOpen. **6**, 266–272 (2017): *Relationship between Side-Chain Polarity and the Self-Assembly Characteristics of Perylene Diimide Derivatives in Aqueous Solution*.

[169] S. Chen, P. Slattum, C. Wang, and L. Zang, Chem. Rev. **115**, 11967–11998 (2015): *Self-Assembly of Perylene Imide Molecules into 1D Nanostructures: Methods, Morphologies, and Applications*.

[170] F. Liscio, S. Milita, C. Albonetti, P.D. D´Angelo, A. Guagliardi, N. Masciocchi, R.G. Della Valle, E. Venuti, A. Brillante, and F. Biscarini, Adv. Funct. Mater. **22**, 943–953 (2012): *Structure and Morphology of PDI8-CN2 for n-Type Thin-Film Transistors*.

[171] C. Keil, H. Graaf, T. Baumgärtel, I. Trenkmann, and D. Schlettwein, Org. Electron. **14**, 2833–2839 (2013): *Intralayer vs. interlayer electronic coupling in perylene imide thin films*.

[172] B.B.A. Jones, A. Facchetti, M.R. Wasielewski, and T.J. Marks, Adv. Funct. Mater. **18**, 1329–1339 (2008): *Effects of Arylene Diimide Thin Film Growth Conditions on n-Channel OFET Performance*.

[173] F. Chiarella, T. Toccoli, M. Barra, L. Aversa, F. Ciccullo, R. Tatti, R. Verucchi, S. Iannotta, and A. Cassinese, Appl. Phys. Lett. **104**, 143302 (2014): *High mobility n-type organic thin-film transistors deposited at room temperature by supersonic molecular beam deposition*.

[174] Y. Sakamoto, S. Komatsu, and T. Suzuki, J. Am. Chem. Soc. **123**, 4643–4644 (2001): *Tetradecafluorosexithiophene: The First Perfluorinated Oligothiophene*.

[175] A. Hinderhofer, U. Heinemeyer, A. Gerlach, S. Kowarik, R.M.J. Jacobs, Y. Sakamoto, T. Suzuki, and F. Schreiber, J. Chem. Phys. **127**, 194705 (2007): *Optical properties of pentacene and perfluoropentacene thin films*.

[176] H. Peisert, M. Knupfer, T. Schwieger, G.G. Fuentes, D. Olligs, J. Fink, and T. Schmidt, J. Appl. Phys. **93**, 9683 (2003): *Fluorination of copper phthalocyanines: Electronic structure and interface properties*.

[177] G. Heimel, I. Salzmann, S. Duhm, and N. Koch, Chem. Mater. **23**, 359–377 (2011): *Design of Organic Semiconductors from Molecular Electrostatics*.

[178] L. Ferlauto, F. Liscio, E. Orgiu, N. Masciocchi, A. Guagliardi, F. Biscarini, P. Samorì, and S. Milita, Adv. Funct. Mater. **24**, 5503–5510 (2014): *Enhancing the Charge Transport in Solution-Processed Perylene Di-imide Transistors via Thermal Annealing of Metastable Disordered Films*.

[179] B.A. Jones, M.J. Ahrens, M. Yoon, A. Facchetti, T.J. Marks, and M.R. Wasielewski, Angew. Chem. **116**, 6523–6526 (2004): *High-Mobility Air-Stable n-Type Semiconductors with*

Processing Versatility: Dicyanoperylene-3,4:9,10-bis(dicarboximides).

[180] C. Musumeci, I. Salzmann, S. Bonacchi, C. Röthel, S. Duhm, N. Koch, and P. Samorì, Adv. Funct. Mater. **25**, 2501–2510 (2015): *The Relationship between Structural and Electrical Characteristics in Perylenecarboxydiimide-Based Nanoarchitectures*.

[181] T. Watanabe, T. Hosokai, T. Koganezawa, and N. Yoshimoto, Mol. Cryst. Liq. Cryst. **566**, 18–21 (2012): *In Situ Real-Time X-Ray Diffraction During Thin Film Growth of Pentacene*.

[182] C. Lorch, R. Banerjee, C. Frank, J. Dieterle, A. Hinderhofer, A. Gerlach, and F. Schreiber, J. Phys. Chem. C. **119**, 819–825 (2015): *Growth of Competing Crystal Phases of α-Sexithiophene Studied by Real-Time in Situ X-ray Scattering*.

[183] S. Herbst, B. Soberats, P. Leowanawat, M. Lehmann, and F. Würthner, Angew. Chem. Int. Ed. **56**, 2162–2165 (2017): *A Columnar Liquid-Crystal Phase Formed by Hydrogen-Bonded Perylene Bisimide J-Aggregates*.

[184] F. May, V. Marcon, R.M. Hansen, F. Grozema, and D. Andrienko, J. Mater. Chem. **21**, 9538–9545 (2011): *Relationship between supramolecular assembly and charge-carrier mobility in perylenediimide derivatives: The impact of side chains*.

[185] R. Resel, M. Bainschab, A. Pichler, T. Dingemans, C. Simbrunner, J. Stangl, and I. Salzmann, J. Synchrotron Rad. **23**, 729–734 (2016): *Multiple scattering in grazing-incidence X-ray diffraction: impact on lattice-constant determination in thin films research papers*.

[186] T.N. Krauss, E. Barrena, D.G. De Oteyza, X.N. Zhang, J. Major, V. Dehm, F. Würthner, and H. Dosch, J. Phys. Chem. C. **113**, 4502–4506 (2009): *X-ray/Atomic Force Microscopy Study of the Temperature-Dependent Multilayer Structure of PTCDI-C8 Films on SiO2*.

[187] E. Ghanbari, T. Wagner, and P. Zeppenfeld, J. Phys. Chem. C. **119**, 24174–24181 (2015): *Layer-Resolved Evolution of Organic Thin Films Monitored by Photoelectron Emission Microscopy and Optical Reflectance Spectroscopy*.

[188] J. Gierschner, L. Lüer, B. Milián-Medina, D. Oelkrug, and H.-J. Egelhaaf, J. Phys. Chem. Lett. **4**, 2686–2697 (2013): *Highly Emissive H-Aggregates or Aggregation-Induced Emission Quenching? The Photophysics of All-Trans para-Distyrylbenzene*.

[189] M. Wykes, S.K. Park, S. Bhattacharyya, S. Varghese, J.E. Kwon, D.R. Whang, I. Cho, R. Wannemacher, L. Lüer, S.Y. Park, and J. Gierschner, J. Phys. Chem. Lett. **6**, 3682–3687 (2015): *Excited State Features and Dynamics in a Distyrylbenzene-Based Mixed Stack Donor–Acceptor Cocrystal with Luminescent Charge Transfer Characteristics*.

[190] B.M. Muccini, M. Murgia, F. Biscarini, and C. Taliani, Adv. Funct. Mater. **13**, 355–358 (2001): *Morphology Controlled Energy Transfer in Conjugated Molecular Thin Films*.

[191] P. Mei, M. Murgia, C. Taliani, E. Lunedei, and M. Muccini, J. Appl. Phys. **88**, 5158 (2000): *Luminescence quantum yield of molecular aggregates and excitons in α-sexithienyl thin films at variable temperature*.

[192] M. Son, K.H. Park, C. Shao, F. Würthner, and D. Kim, J. Phys. Chem. Lett. **5**, 3601–3607 (2014): *Spectroscopic Demonstration of Exciton Dynamics and Excimer Formation in a Sterically Controlled Perylene Bisimide Dimer Aggregate*.

[193] R.E. Cook, B.T. Phelan, R.J. Kamire, M.B. Majewski, R.M. Young, and M.R. Wasielewski,

J. Phys. Chem. A. **121**, 1607–1615 (2017): *Excimer Formation and Symmetry-Breaking Charge Transfer in Cofacial Perylene Dimers*.

[194] H. Liu, L. Shen, Z. Cao, and X. Li, Phys. Chem. Chem Phys. **16**, 16399 (2014): *Covalently linked perylenetetracarboxylic diimide dimers and trimers with rigid "'J-type"' aggregation structure*.

[195] J.M. Giaimo, J. V Lockard, L.E. Sinks, A.M. Scott, T.M. Wilson, and M.R. Wasielewski, J. Phys. Chem. A. **112**, 2322–2330 (2008): *Excited Singlet States of Covalently Bound, Cofacial Dimers and Trimers of Perylene-3,4:9,10-bis(dicarboximide)s*.

[196] A. Zykov, S. Bommel, C. Wolf, L. Pithan, C. Weber, P. Beyer, C. Santoro, J.P. Rabe, and S. Kowarik, J. Chem. Phys. **146**, 052803 (2017): *Diffusion and nucleation in multilayer growth of PTCDI-C8 studied with in situ X-ray growth oscillations and real-time small angle X-ray scattering*.

[197] A.E. Lita, and J.E.J. Sanchez, Phys. Rev. B. **61**, 7692–7699 (2000): *Effects of grain growth on dynamic surface scaling during the deposition of Al polycrystalline thin films*.

[198] T. V Desai, E.R. Kish, A.R. Woll, and J.R. Engstrom, J. Phys. Chem. C. **115**, 18221–18234 (2011): *Hyperthermal Growth of N,N´-Ditridecylperylene-3,4,9,10-tetracarboxylic Diimide on Self-Assembled Monolayers: Adsorption Dynamics and Sub- and Multilayer Thin Film Growth*.

[199] F. Anger, H. Glowatzki, A. Franco-Canellas, C. Bürker, A. Gerlach, R. Scholz, Y. Sakamoto, T. Suzuki, N. Koch, and F. Schreiber, J. Phys. Chem. C. **119**, 6769–6776 (2015): *Interface Dipole and Growth Mode of Partially and Fully Fluorinated Rubrene on Au(111) and Ag(111)*.

[200] B. Reisz, S. Weimer, R. Banerjee, C. Zeiser, C. Lorch, G. Duva, J. Dieterle, K. Yonezawa, J.-P. Yang, N. Ueno, S. Kera, A. Hinderhofer, A. Gerlach, and F. Schreiber, J. Mater. Res. **32**, 1908–1920 (2017): *Structural, optical, and electronic characterization of per fluorinated sexithiophene films and mixed films with sexithiophene*.

[201] S.-A. Savu, A. Sonström, R. Bula, H.F. Bettinger, T. Chassé, and M.B. Casu, ACS Appl. Mater. Interfaces. **7**, 19774–19780 (2015): *Intercorrelation of Electronic, Structural, and Morphological Properties in Nanorods of 2,3,9,10-Tetrafluoropentacene*.

[202] J. Rivnay, L.H. Jimison, J.E. Northrup, M.F. Toney, R. Noriega, S. Lu, T.J. Marks, A. Facchetti, and A. Salleo, Nat. Mater. **8**, 952–958 (2009): *Large modulation of carrier transport by grain-boudary molecular packing and microstructure in organic thin films*.

[203] R.M. Osuna, V. Hernández, J.T.L. Navarrete, E. D´Oria, and J.J. Novoa, Theor. Chem. Acc. **128**, 541–553 (2011): *Theoretical evaluation of the nature and strength of the F...F intermolecular interactions present in fluorinated hydrocarbons*.

[204] P. Panini, and D. Chopra, CrystEngComm. **15**, 3711–3733 (2013): *Quantitative insights into energy contributions of intermolecular interactions in fluorine and trifluoromethyl substituted isomeric N-phenylacetamides and N-methylbenzamides*.

[205] B.-E. Schuster, T. V Basova, V.A. Plyashkevich, H. Peisert, and T. Chassé, Thin Solid Films. **518**, 7161–7166 (2010): *Effects of temperature on structural and morphological features of CoPc and CoPcF16 thin films*.

[206] M. Hird, Chem. Soc. Rev. **36**, 2070–2095 (2007): *Fluorinated liquid crystals – properties and applications*.

[207] P. Zugenmaier, J. Duff, and T.L. Bluhm, Cryst. Res. Technol. **35**, 1095–1115 (2000): *Crystal and Molecular Structures of Six Differently with Halogen Substituted Bis (benzylimido) perylene*.

[208] F.C. Spano, J. Am. Chem. Soc. **131**, 4267–4278 (2009): *Analysis of the UV/Vis and CD Spectral Line Shapes of Carotenoid Assemblies: Spectral Signatures of Chiral H-Aggregates*.

[209] L. Gisslén, and R. Scholz, Phys. Rev. B. **83**, 155311 (2011): *Crystallochromy of perylene pigments: Influence of an enlarged polyaromatic core region*.

[210] A.C. Dürr, F. Schreiber, K.A. Ritley, V. Kruppa, J. Krug, H. Dosch, and B. Struth, Phys. Rev. Lett. **90**, 016104 (2003): *Rapid Roughening in Thin Film Growth of an Organic Semiconductor (Diindenoperylene)*.

[211] S. Kowarik, A. Gerlach, S. Sellner, F. Schreiber, L. Cavalcanti, and O. Konovalov, Phys. Rev. Lett. **96**, 125504 (2006): *Real-Time Observation of Structural and Orientational Transitions during Growth of Organic Thin Films*.

[212] A. Hinderhofer, T. Hosokai, C. Frank, J. Novák, A. Gerlach, and F. Schreiber, J. Phys. Chem. C. **115**, 16155–16160 (2011): *Templating Effect for Organic Heterostructure Film Growth: Perfluoropentacene on Diindenoperylene*.

[213] A. Hinderhofer, C. Frank, T. Hosokai, A. Resta, A. Gerlach, and F. Schreiber, J. Chem. Phys. **134**, 104702 (2011): *Structure and morphology of coevaporated pentacene-perfluoropentacene thin films*.

[214] A. Opitz, A. Wilke, P. Amsalem, M. Oehzelt, R.-3. Blum, J.P. Rabe, T. Mizokuro, U. Hörmann, R. Hansson, E. Moons, and N. Koch, Sci. Rep. **6**, 21291 (2016): *Organic heterojunctions: Contact-induced molecular reorientation, interface states, and charge re-distribution*.

[215] P. Beyer, T. Breuer, S. Ndiaye, A. Zykov, A. Viertel, M. Gensler, J.P. Rabe, S. Hecht, G. Witte, and S. Kowarik, ACS. **6**, 21484–21493 (2014): *Lattice Matching as the Determining Factor for Molecular Tilt and Multilayer Growth Mode of the Nanographene Hexa-peri-hexabenzocoronene*.

[216] S.M. Menke, C.D. Lindsay, and R.J. Holmes, Appl. Phys. Lett. **104**, 243302 (2014): *Optical spacing effect in organic photovoltaic cells incorporating a dilute acceptor layer*.

[217] T.M. Clarke, and J.R. Durrant, Chem. Rev. **110**, 6736–6767 (2010): *Charge Photogeneration in Organic Solar Cells*.

[218] K. Vandewal, A. Gadisa, W.D. Oosterbaan, S. Bertho, F. Banishoeib, I. Van Severen, L. Lutsen, T.J. Cleij, D. Vanderzande, and J. V Manca, Adv. Funct. Mater. **18**, 2064–2070 (2008): *The Relation Between Open-Circuit Voltage and the Onset of Photocurrent Generation by Charge-Transfer Absorption in Polymer : Fullerene Bulk Heterojunction Solar Cells*.

[219] V. V Bruevich, T.S. Makhmutov, S.G. Elizarov, E.M. Nechvolodova, and D.Y. Paraschuk, J. Chem. Phys. **127**, 104905 (2007): *Raman spectroscopy of intermolecular charge transfer complex between a conjugated polymer and an organic acceptor molecule*.

[220] L. Goris, K. Haenen, M. Nesládek, P. Wagner, D. Vanderzande, L. De Schepper, J. D´Haen, L. Lutsen, and J. V. Manca, J. Mater. Sci. **40**, 1413–1418 (2005): *Absorption phenomena in organic thin films for solar cell applications investigated by photothermal*

deflection spectroscopy.

[221] L. Goris, A. Poruba, L. Hod´ákova, M. Vaněček, K. Haenen, M. Nesládek, P. Wagner, D. Vanderzande, L. De Schepper, and J. V Manca, J. Appl. Phys. **88**, 052113 (2006): *Observation of the subgap optical absorption in polymer-fullerene blend solar cells*.

[222] M.P. Seah, and W.A. Dench, Surf. Interface Anal. **1**, 2–11 (1979): *Quantitative Electron Spectroscopy of Surfaces: A Standart Base for Electron Inelastic Mean Free Paths in Solids*.

[223] J.S. Chappell, A.N. Bloch, W.A. Bryden, Maxfield, T.O. Poehler, and D.O. Cowan, J. Am. Chem. Soc. **103**, 2442–2443 (1981): *Degree of Charge Transfer in Organic Conductors by Infrared Absorption SPectroscopy*.

[224] D. Nanova, S. Beck, A. Fuchs, T. Glaser, C. Lennartz, W. Kowalsky, A. Pucci, and M. Kroeger, Org. Electron. **13**, 1237–1244 (2012): *Charge transfer in thin films of donor–acceptor complexes studied by infrared spectroscopy*.

[225] M. Rudloff, K. Ackermann, M. Huth, H.O. Jeschke, M. Tomic, R. Valentí, B. Wolfram, M. Bröring, M. Bolte, D. Chercka, M. Baumgarten, and K. Müllen, Phys. Chem. Chem Phys. **17**, 4118–4126 (2015): *Charge transfer tuning by chemical substitution and uniaxial pressure in the organic complex tetramethoxypyrene-tetracyanoquinodimethane*.

[226] K. Medjanik, S. Perkert, S. Naghavi, M. Rudloff, V. Solovyeva, D. Chercka, M. Huth, S.A. Nepijko, T. Methfessel, C. Felser, M. Baumgarten, K. Müllen, H.J. Elmers, and G. Schönhense, Phys. Rev. B. **82**, 245419 (2010): *Formation of an intermolecular charge-transfer compound in UHV codeposited tetramethoxypyrene and tetracyanoquinodimethane*.

[227] W.N. Han, K. Yonezawa, R. Makino, K. Kato, A. Hinderhofer, R. Murdey, R. Shiraishi, H. Yoshida, N. Sato, N. Ueno, and S. Kera, Appl. Phys. Lett. **103**, 253301 (2013): *Quantitatively identical orientation-dependent ionization energy and electron affinity of diindenoperylene*.

[228] G.M. Rangger, O.T. Hofmann, L. Romaner, G. Heimel, B. Bröker, R.-P. Blum, R.L. Johnson, N. Koch, and E. Zojer, Phys. Rev. B. **79**, 165306 (2009): *F4TCNQ on Cu, Ag, and Au as prototypical example for a strong organic acceptor on coinage metals*.

[229] C. Christodoulou, A. Giannakopoulos, G. Ligorio, M. Oehzelt, M. Timpel, J. Niederhausen, L. Pasquali, A. Giglia, K. Parvez, K. Müllen, D. Beljonne, N. Koch, and M. V Nardi, ACS Appl. Mater. Interfaces. **7**, 19134–19144 (2015): *Tuning the Electronic Structure of Graphene by Molecular Dopants: Impact of the Substrate*.

[230] A. Wilke, P. Amsalem, J. Frisch, B. Bröker, A. Vollmer, and N. Koch, Appl. Phys. Lett. **98**, 123304 (2011): *Electric fields induced by energy level pinning at organic heterojunctions*.

[231] C. Arantes, M. Scholz, R. Schmidt, V. Dehm, M.L.M. Rocco, A. Schöll, F. Reinert, and F. Würthner, Appl. Phys. A. **108**, 629–637 (2012): *Comparative analysis of the energy levels of planar and core-twisted perylene bisimides in solution and solid state by UV/VIS, CV, and UPS/IPES*.

[232] A. Opitz, J. Frisch, R. Schlesinger, A. Wilke, and N. Koch, J. Electron Spectros. Relat. Phenomena. **190**, 12–24 (2013): *Energy level alignment at interfaces in organic photovoltaic devices*.

[233] K. Akaike, N. Koch, G. Heimel, and M. Oehzelt, Adv. Mater. Interfaces. **2**, 1500232 (2015): *The Impact of Disorder on the Energy Level Alignment at Molecular Donor–Acceptor*

Interfaces.

[234] M. Schwarze, W. Tress, B. Beyer, F. Gao, R. Scholz, C. Poelking, K. Ortstein, A.A. Günther, D. Kasemann, D. Andrienko, and K. Leo, Science. **352**, 1446–1450 (2016): *Band structure engineering in organic organic semiconductors*.

[235] I. Salzmann, S. Duhm, G. Heimel, M. Oehzelt, R. Kniprath, R.L. Johnson, J.P. Rabe, and N. Koch, J. Am. Chem. Soc. **130**, 12870–12871 (2008): *Tuning the Ionization Energy of Organic Semiconductor Films: The Role of Intramolecular Polar Bonds*.

[236] S. Duhm, G. Heimel, I. Salzmann, H. Glowatzki, R.L. Johnson, A. Vollmer, J.P. Rabe, and N. Koch, Nat. Mater. **7**, 326–332 (2008): *Orientation-dependent ionization energies and interface dipoles in ordered molecular assemblies*.

[237] F.E. Osterloh, M.A. Holmes, J. Zhao, L. Chang, S. Kawula, J.D. Roehling, and A.J. Moule, J. Phys. Chem. C. **118**, 14723–14731 (2014): *P3HT:PCBM Bulk-Heterojunctions: Observing Interfacial and Charge Transfer States with Surface Photovoltage Spectroscopy*.

[238] R.A. Street, D. Davies, P.P. Khlyabich, B. Burkhart, and B.C. Thompson, J. Am. Chem. Soc. **135**, 986–989 (2013): *Origin of the Tunable Open-Circuit Voltage in Ternary Blend Bulk Heterojunction Organic Solar Cells*.

[239] S.M. Tuladhar, D. Poplavskyy, S.A. Choulis, J.R. Durrant, D.D.C. Bradley, and J. Nelson, Adv. Funct. Mater. **15**, 1171–1182 (2005): *Ambipolar Charge Transport in Films of Methanofullerene and Poly(phenylenevinylene)/Methanofullerene Blends*.

[240] K. Tvingstedt, K. Vandewal, A. Gadisa, F. Zhang, J. Manca, and O. Inganäs, J. Am. Chem. Soc. **131**, 11819–11824 (2009): *Electroluminescence from Charge Transfer States in Polymer Solar Cells*.

[241] S.D. Dimitrov, A.A. Bakulin, C.B. Nielsen, B.C. Schroeder, J. Du, H. Bronstein, I. Mcculloch, R.H. Friend, and J.R. Durrant, J. Am. Chem. Soc. **134**, 18189–18192 (2012): *On the Energetic Dependence of Charge Separation in Low-Band- Gap Polymer/Fullerene Blends*.

[242] J. Behrends, A. Sperlich, A. Schnegg, T. Biskup, C. Teutloff, K. Lips, V. Dyakonov, and R. Bittl, Phys. Rev. B. **85**, 125206 (2012): *Direct Detection of Photoinduced Charge Transfer Complexes in Polymer:Fullerene Blends*.

[243] P. Panda, D. Veldman, J. Sweelssen, J.J.A.M. Bastiaansen, B.M.W. Langeveld-Voss, and S.C.J. Meskers, J. Phys. Chem. B. **111**, 5076–5081 (2007): *Charge Transfer Absorption for π-Conjugated Polymers and Oligomers Mixed with Electron Acceptors*.

[244] M. Imoto, H. Ikeda, T. Fujii, H. Taniguchi, A. Tamaki, M. Takeda, and K. Mizuno, Org. Lett. **12**, 1940–1943 (2010): *Contrasting Intermolecular and Intramolecular Exciplex Formation of a 1,4-Dicyano-2-methylnaphthalene-N,N-Dimethyl-p-toluidine Dyad*.

[245] M. Hallermann, S. Haneder, and E. Da Como, Appl. Phys. Lett. **93**, 053307 (2008): *Charge-transfer states in conjugated polymer/fullerene blends: Below-gap weakly bound excitons for polymer photovoltaics*.

[246] S.P. Gromov, E.N. Ushakov, A.I. Vedernikov, N.A. Lobova, M. V Alfimov, Y.A. Strelenko, J.K. Whitesell, and M.A. Fox, Org. Lett. **1**, 1697–1699 (1999): *A Novel Optical Sensor for Metal Ions Based on Ground-State Intermolecular Charge-Transfer Complexation*.

[247] S. Sweetnam, K. Vandewal, E. Cho, C. Risko, V. Coropceanu, A. Salleo, J.-L. Brédas, and

M.D. McGehee, Chem. Mater. **28**, 1446–1452 (2016): *Characterizing the Polymer: Fullerene Intermolecular Interactions*.

[248] M. Heilig, M. Domhan, and H. Port, J. Lumin. **110**, 290–295 (2004): *Optical properties and morphology of thin diindenoperylene films*.

[249] D. Zhang, A. Horneber, J. Mihaljevic, U. Heinemeyer, K. Braun, F. Schreiber, R. Scholz, and A.J. Meixner, J. Lumin. **131**, 502–505 (2011): *Plasmon resonance modulated photoluminescence and Raman spectroscopy of diindenoperylene organic semiconductor thin film*.

[250] K. Tvingstedt, K. Vandewal, F. Zhang, and O. Ingana, J. Phys. Chem. C. **114**, 21824–21832 (2010): *On the Dissociation Efficiency of Charge Transfer Excitons and Frenkel Excitons in Organic Solar Cells: A Luminescence Quenching Study*.

[251] F. Anger, J.O. Ossó, U. Heinemeyer, K. Broch, R. Scholz, A. Gerlach, and F. Schreiber, J. Chem. Phys. **136**, 0054701 (2012): *Photoluminescence spectroscopy of pure pentacene, perfluoropentacene, and mixed thin films*.

[252] D. Jarzab, F. Cordella, J. Gao, M. Scharber, H.-J. Egelhaaf, and M.A. Loi, Adv. Energy Mater. **1**, 604–609 (2011): *Low-Temperature Behaviour of Charge Transfer Excitons in Narrow-Bandgap Polymer-Based Bulk Heterojunctions*.

[253] A.P. Arndt, M. Gerhard, A. Quintilla, I.A. Howard, M. Koch, and U. Lemmer, J. Phys. Chem. C. **119**, 13516–13523 (2015): *Time-Resolved Charge-Transfer State Emission in Organic Solar Cells: Temperature and Blend Composition Dependences of Interfacial Traps*.

[254] P.B. Deotare, W. Chang, E. Hontz, D.N. Congreve, L. Shi, P.D. Reusswig, B. Modtland, M.E. Bahlke, C.K. Lee, A.P. Willard, V. Bulovic, T. Van Voorhis, and M.A. Baldo, Nat. Mater. **14**, 1130–1134 (2015): *Nanoscale transport of charge-transfer states in organic donor–acceptor blends*.

[255] U. Heinemeyer, A. Hinderhofer, M.I. Alonso, J.O. Ossó, M. Garriga, M. Kytka, A. Gerlach, and F. Schreiber, Phys. Stat. Sol. **205**, 927–930 (2008): *Uniaxial anisotropy of organic thin films determined by ellipsometry*.

[256] K. Broch, U. Heinemeyer, A. Hinderhofer, F. Anger, R. Scholz, A. Gerlach, and F. Schreiber, Phys. Rev. B. **83**, 245307 (2011): *Optical evidence for intermolecular coupling in mixed films of pentacene and perfluoropentacene*.

[257] A. Opitz, B. Ecker, J. Wagner, A. Hinderhofer, F. Schreiber, J. Manara, J. Pflaum, and W. Brütting, Org. Electron. **10**, 1259–1267 (2009): *Mixed crystalline films of co-evaporated hydrogen- and fluorine-terminated phthalocyanines and their application in photovoltaic devices*.

[258] M. Gruber, J. Wagner, K. Klein, U. Hörmann, A. Opitz, M. Stutzmann, and W. Brütting, Adv. Energy Mater. **2**, 1100–1108 (2012): *Thermodynamic Efficiency Limit of Molecular Donor-Acceptor Solar Cells and its Application to Diindenoperylene/C60-Based Planar Heterojunction Devices*.

[259] U. Rau, Phys. Rev. B. **76**, 085303 (2007): *Reciprocity relation between photovoltaic quantum efficiency and electroluminescent emission of solar cells*.

[260] A.N. Brigeman, M.A. Fusella, Y. Yan, G.E. Purdum, Y.-L. Loo, B.P. Rand, and N.C. Giebink, Adv. Energy Mater. **6**, 1601001 (2016): *Revealing the Full Charge Transfer State Absorption Spectrum of Organic Solar Cells*.

[261] G.O.N. Ndjawa, K.R. Graham, S. Mollinger, D.M. Wu, D. Hanifi, R. Prasanna, B.D. Rose, S. Dey, L. Yu, J. Brédas, M.D. McGehee, A. Salleo, and A. Amassian, Adv. Energy Mater. **7**, 1601995 (2017): *Open-Circuit Voltage in Organic Solar Cells: The Impacts of Donor Semicrystallinity and Coexistence of Multiple Interfacial Charge-Transfer Bands*.

[262] N. Karl, Synth. Met. **133**, 649–657 (2003): *Charge carrier transport in organic semiconductors*.

[263] X. Cheng, M. Caironi, Y.-Y. Noh, C. Newman, J. Wang, M.J. Jung, K. Banger, R. Di Pietro, A. Facchetti, and H. Sirringhaus, Org. Electron. **13**, 320–328 (2012): *Downscaling of n-channel organic field-effect transistors with inkjet-printed electrodes*.

[264] I. Salzmann, and G. Heimel, J. Electron Spectros. Relat. Phenomena. **204**, 208–222 (2015): *Toward a comprehensive understanding of molecular doping organic semiconductors*.

[265] M. Pope, and C.E. Swenberg, Oxford University Press, New York (1999): *Electronic Processes in Organic Crystals and Polymers*.

[266] I.G. Hill, A. Kahn, Z.G. Soos, and R.A. Pascal Jr., Chem. Phys. Lett. **327**, 181–188 (2000): *Charge-separation energy in films of p-conjugated organic molecules*.

[267] M.H. Hennessy, Z.G. Soos, R.A. Pascal Jr., and A. Girlando, Chem. Phys. **245**, 199–212 (1999): *Vibronic structure of PTCDA stacks: the exciton–phonon-charge-transfer dimer*.

[268] X. Xu, T. Xiao, X. Gu, X. Yang, S. V Kershaw, N. Zhao, J. Xu, and Q. Miao, ACS Appl. Mater. Interfaces. **7**, 28019–28026 (2015): *Solution-Processed Ambipolar Organic Thin-Film Transistors by Blending p-and n-Type Semiconductors: Solid Solution versus Microphase Separation*.

[269] H. Méndez, G. Heimel, A. Opitz, K. Sauer, P. Barkowski, M. Oehzelt, J. Soeda, T. Okamoto, J. Takeya, J.-B. Arlin, Y. Balandier, Y. Geerts, N. Koch, and I. Salzmann, Angew. Chem. Int. Ed. **52**, 7751–7755 (2013): *Doping of Organic Semiconductors: Impact of Dopant Strength and Electronic Coupling*.

[270] S. Joseph, M.K. Ravva, and J.-L. Bredas, J. Phys. Chem. Lett. **8**, 5171–5176 (2017): *Charge-Transfer Dynamics in the Lowest Excited State of a Pentacene–Fullerene Complex: Implications for Organic Solar Cells*.

[271] J. Gierschner, H.-G. Mack, D. Oelkrug, I. Waldner, and H. Rau, J. Phys. Chem. A. **108**, 257–263 (2004): *Modeling of the Optical Properties of Cofacial Chromophore Pairs: Stilbenophane*.

[272] J. Gierschner, M. Ehni, H.-J. Egelhaaf, B. Milián-Medina, D. Beljonne, H. Benmansour, and G.C. Bazan, J. Chem. Phys. **123**, 144914 (2013): *Solid-state optical properties of linear polyconjugated molecules: π-stack contra herringbone*.

[273] Y. Yi, V. Coropceanu, and J.-L. Brédas, J. Am. Chem. Soc. **131**, 15777–15783 (2009): *Exciton-Dissociation and Charge-Recombination Processes in Pentacene/C60 Solar Cells: Theoretical Insight into the Impact of Interface Geometry*.

[274] C. Wang, J. Wang, N. Wu, M. Xu, X. Yang, Y. Lu, and L. Zang, RSC Adv. **7**, 2382–2387 (2017): *Donor–acceptor single cocrystal of coronene and perylene diimide: molecular self-assembly and charge-transfer photoluminescence*.

[275] I.M. Lifschitz, and V. V. Slyozov, J. Phys. Chem. Solids. **19**, 35–50 (1961): *The kinetics of precipitation from supersaturated solid solutions*.

[276] R.A. Marcus, J. Phys. Chem. **93**, 3078–3086 (1989): *Relation between Charge Transfer Absorption and Fluorescence Spectra and the Inverted Region*.

[277] E. Buchaca-Domingo, K. Vandewal, Z. Fei, S.E. Watkins, F.H. Scholes, J.H. Bannock, J.C. de Mello, L.J. Richter, D.M. DeLongchamp, A. Amassian, M. Heeney, A. Salleo, and N. Stingelin, J. Am. Chem. Soc. **137**, 5256–5259 (2015): *Direct Correlation of Charge Transfer Absorption with Molecular Donor:Acceptor Interfacial Area via Photothermal Deflection Spectroscopy*.

[278] K.R. Graham, P. Erwin, D. Nordlund, K. Vandewal, R. Li, G.O.N. Ndjawa, E.T. Hoke, A. Salleo, M.E. Thompson, M.D. McGehee, and A. Amassian, Adv. Mater. **25**, 6076–6082 (2013): *Re-evaluating the Role of Sterics and Electronic Coupling in Determining the Open-Circuit Voltage of Organic Solar Cells*.

[279] C. Sagui, and M. Grant, Phys. Rev. E. **59**, 4175–4187 (1999): *Theory of nucleation and growth during phase separation*.

[280] B. Ray, P. Nair, and M.A. Alam, Sol. Energy Mater. Sol. Cells. **95**, 3287–3294 (2011): *Annealing dependent performance of organic bulk- heterojunction solar cells: A theoretical perspective*.

[281] C. Zheng, D. Bleier, I. Jalan, S. Pristash, A.R. Penmetcha, N.J. Hestand, F.C. Spano, M.S. Pierce, J.A. Cody, and C.J. Collison, Sol. Energy Mater. Sol. Cells. **157**, 366–376 (2016): *Phase separation, crystallinity and monomer-aggregate population control in solution processed small molecule solar cells*.

[282] T. Breuer, and G. Witte, J. Chem. Phys. **138**, 114901 (2013): *Thermally activated intermixture in pentacene-perfluoropentacene heterostructures*.

[283] N. Ueno, Science. **352**, 1395–1396 (2016): *Tuning organic band structures with Coulomb interactions*.

[284] B. Siegmund, M.T. Sajjad, J. Widmer, D. Ray, C. Koerner, M. Riede, K. Leo, I.D.W. Samuel, and K. Vandewal, Adv. Mater. **29**, 1604424 (2017): *Exciton Diffusion Length and Charge Extraction Yield in Organic Bilayer Solar Cells*.

[285] J. Lee, P. Jadhav, P.D. Reusswig, S.R. Yost, N.J. Thompson, D.N. Congreve, E. Hontz, T.V.A.N. Voorhis, and M.A. Baldo, Acc. Chem. Res. **46**, 1300–1311 (2013): *Singlet Exciton Fission Photovoltaics*.

[286] J. Lee, M.J. Bruzek, N.J. Thompson, M.Y. Sfeir, J.E. Anthony, and M.A. Baldo, Adv. Mater. **25**, 1445–1448 (2013): *Singlet Exciton Fission in a Hexacene Derivative*.

LIST OF PUBLICATIONS

[1] V. Belova, C. Zeiser, T. Storzer, J. Rozbořil, J. Novak, A. Hinderhofer, A. Gerlach, and F. Schreiber, in preparation: *Structure-Dependent Charge Transfer in Donor/Acceptor Systems for Organic Photovoltaics*.

[2] V. Belova, B. Wagner, B. Reisz, C. Zeiser, G. Duva, J. Rozbořil, J. Novák, A. Gerlach, A. Hinderhofer, and F. Schreiber, J. Phys. Chem. C, 2018, **122**, 8589-8601: *Real-Time Structural and Optical Study of Growth and Packing Behavior of Perylene Diimide Derivative Thin Films: Influence of Side-Chain Modification*.

[3] V. Belova, P. Beyer, E. Meister, T. Linderl, M.-U. Halbich, M. Gerhard, S. Schmidt, T. Zechel, T. Meisel, A. V. Generalov, A. S. Anselmo, R. Scholz, O. Konovalov, A. Gerlach, M. Koch, A. Hinderhofer, A. Opitz, W. Brütting, and F. Schreiber. "Highlight" of the ESRF Annual Report 2017 (published 2018), 66 (Invited Article): *Revealing the interplay between structure and electronic coupling in donor/acceptor systems for organic photovoltaics*.

[4] T. Storzer, A. Hinderhofer , C. Zeiser, J. Novák, Z. Fišer, V. Belova, B. Reisz, S. Maiti, G. Duva, R. K. Hallani, A. Gerlach, J. E. Anthony, and F. Schreiber, J. Phys. Chem. C, 2017, **121**, 21011−21017: *Growth, Structure, and Anisotropic Optical Properties of Difluoro-anthradithiophene Thin Films*.

[5] M. Hänsel, V. Belova, A. Hinderhofer, F. Schreiber, K. Broch, and P. Tegeder, J. Phys. Chem. C, 2017, **121**, 17900−17906: *Ultrafast Excited State Dynamics in Diindenoperylene Films*.

[6] K. Broch, M. Gerhard, M. Halbich, S. Lippert, V. Belova, M. Koch, and F. Schreiber, Phys. Status Solidi RRL, 2017, **11**, 1700064: *Time-resolved photoluminescence spectroscopy of charge transfer states in blends of pentacene and perfluoropentacene*.

[7] V. Belova, P. Beyer, E. Meister, T. Linderl, M.-U. Halbich, M. Gerhard, S. Schmidt, T. Zechel, T. Meisel, A. V. Generalov, A. S. Anselmo, R. Scholz, O. Konovalov, A. Gerlach, M. Koch, A. Hinderhofer, A. Opitz, W. Brütting, and F. Schreiber, J. Am. Chem. Soc., 2017, **139**, 8474−8486: *Evidence for Anisotropic Electronic Coupling of Charge Transfer States in Weakly Interacting Organic Semiconductor Mixtures*.

[8] M. I. Dar, A. Hinderhofer, G. Jacopin, V. Belova, N. Arora, S. M. Zakeeruddin, F. Schreiber, and M. Grätzel, Adv. Funct. Mater., 2017, **27**, 1701433: *Function Follows Form: Correlation between the Growth and Local Emission of Perovskite Structures and the Performance of Solar Cells*.

[9] C. Lorch, K. Broch, V. Belova, G. Duva, A. Hinderhofer, A. Gerlach, M. Jankowski and F. Schreiber, J. Appl. Cryst., 2016, **49**, 1266-1275: *Growth and annealing kinetics of [alpha]-sexithiophene and fullerene C60 mixed films*.

[10] Y. Nakayama, Y. Mizuno, T. Hosokai, T. Koganezawa, R. Tsuruta, A. Hinderhofer, A. Gerlach, K. Broch, V. Belova, H. Frank, M. Yamamoto, J. Niederhausen, H. Glowatzki, J. P. Rabe, N. Koch, H. Ishii, F. Schreiber, and N. Ueno, ACS Appl. Mater. Interfaces, 2016, **8**, 13499−13505: *Epitaxial Growth of an Organic p−n Heterojunction: C60 on Single-Crystal Pentacene*.

[11] V. A. Belova, V. F. Borodzjulja, T. F. Ivanova, V. M. Kapralova, and N. T. Sudar, Technical Physics, 2015, **60**, 588-591: *Pecular Dielectric Properties of Poly(diphenylene Phthalide) at Elevated Temperatures*.

DEUTSCHE ZUSAMMENFASSUNG

Diese Arbeit befasst sich mit der Untersuchung von binär gemischten molekularen Heterostrukturen auf der Basis kleiner organischer Halbleiter durch den Einsatz komplementärer, experimenteller Methoden. Dabei werden fundamentale Aspekte des Filmwachstums durch organische Molekularstrahlabscheidung - insbesondere das Mischungsverhalten der Moleküle, die Nukleation und die zeitliche Entwicklung der Kristallphasen während des Filmwachstums, sowie strukturelle, morphologische, spektroskopische und elektronische Eigenschaften - berücksichtigt.

Als organische Halbleiter mit Anwendungsperspektive in der Photovoltaik wurden folgende Materialien ausgewählt, um daraus vier verschiedene Donor/Akzeptor-Paare zu bilden: Diindenoperylen (DIP) und Pentacen (PEN) als Donatoren und Perylendiimidderivate (PDIs), PDIR-CN_2 und PDIF-CN_2 als Akzeptoren. Sowohl PDIR-CN_2- als auch PDIF-CN_2-Moleküle enthalten ein Perylendiimid-Gerüst, ähnlich der DIP-Struktur, sowie verschiedene Seitenketten, d.h. verzweigte Alkylketten und fluorierte lineare Ketten.

Für die strukturelle Charakterisierung wurden oberflächenempfindliche Röntgenbeugungs-methoden sowohl in Echtzeit während des Filmwachstums als auch post-growth angewandt. Die morphologischen Eigenschaften der hergestellten Filme wurden mittels Rasterkraftmikroskopie analysiert. Die durch intermolekulare Wechselwirkungen bedingte Exziton-Phonon-Kopplung wurde mit optischen Methoden wie der spektroskopischen Ellipsometrie, der temperaturabhängigen Photolumineszenz (PL) und der differentiellen Reflexionsspektroskopie untersucht. Wie in Kapitel 5 diskutiert, führt aufgrund der unterschiedlichen Elektronendichten der Seitenketten der Einfluss auf die intermolekulare Kopplung zu sehr unterschiedlichen strukturellen und optischen Eigenschaften in dünnen Filmen im Vergleich zu Monomeren.

Die Fähigkeit der Moleküle, einen Ladungstransfer (CT)-Komplex zu bilden, wird in Kapitel 6 am Beispiel von DIP: PDIR-CN_2 untersucht, wobei verschiedene Heterostrukturkonfigurationen verglichen werden. Die Bildung einer Mischphase mit einer bevorzugten π-π-Stapelung der Moleküle in dünnen Filmen, wurde mit XRD und Nahkanten-Röntgenabsorptionsfeinstruktur-Spektroskopie (NEXAFS) beobachtet. Das Auftreten eines partiellen Ladungstransfers (CT) im elektronischen Grundzustand wurde durch Infrarot- und Ultraviolett-Photoelektronen-spektroskopie in Mischungen gegenüber planaren Bi-(Mehrfach-) Schichten gezeigt. Die entsprechenden Solarzellen wurden hergestellt und vollständig charakterisiert, so dass ihre Effizienz mit der Dünnschichtstruktur und den Eigenschaften des CT-Komplexes korreliert werden konnte. Für starke, im angeregten Zustand zu beobachtende CT-Übergänge, die durch optische Absorption, zeitaufgelöste PL, Elektrolumineszenz und Photonen-zu-Strom-Effizienz-Messungen untersucht wurden, konnte deren anisotrope Natur nachgewiesen werden.

Der Vergleich zwischen den vier Donor/Akzeptor-Systemen wird in Kapitel 7 vorgestellt. Die daraus resultierenden unterschiedlichen Mischungsszenarien als Funktion der intermolekularen Wechselwirkung und der Wachstumsbedingungen, sowie deren Einfluss auf die CT-Komplexbildung werden diskutiert. Es wird gezeigt, dass nur das aromatische Rückgrat der PDI-Akzeptormaterialien an diesem anisotropen und in Richtung der π-π-Stapelung orientiertem CT-Übergang beteiligt ist, während die Seitenketten nur die Umgebungseigenschaften beeinflussen. Ersetzt man DIP als Donator durch PEN, führt das aufgrund des unterschiedlichen aromatischen Systems zu einer entsprechenden Änderung der CT-Anregungsenergien.

Die erhaltenen Ergebnisse sind nicht nur für das Verständnis grundlegender Aspekte intermolekularer Wechselwirkungen und Dünnschichteigenschaften von Bedeutung, sondern auch für die Anpassung der Funktionalität aktiver Schichten in organischen, photovoltaischen Bauelementen.

ACKNOLEDGEMENTS

I am using this opportunity to express my gratitude to everyone who supported me throughout these four years of my Ph.D. study.

Firstly, I would like to thank my thesis advisor Prof. Dr. Frank Schreiber for his scientific guidance, support and this great opportunity to be a part of the group and participate in this exciting project.

I would like to express my sincere gratitude to Dr. Alexander Hinderhofer for the supervising and continuous support of my Ph.D. study and related research, for his patience, motivation, and immense knowledge. I also express my warm thanks to Dr. Alexander Gerlach and Dr. Katharina Broch. Guidance of these people helped me in all the time of research and writing of this thesis.

I must acknowledge that this research was financially supported by the Deutsche Forschungsgemeinschaft (SCHR 700/20-1).

I am very grateful to our colleagues from Prof. Dr. Wolfgang Brütting´s group (University of Augsburg) for providing the solar cell data, Dr. Andreas Opitz´s group (Humboldt University of Berlin) for performing the UPS and NEXAFS measurements, Prof. Dr. Martin Koch´s group (University of Marburg) for exploring the TRPL properties of my samples, and all of them together for the fruitful collaboration.

I would like to thank Prof. Dr. Reinhard Scholz (IAPP, TU Dresden) for performing the IR spectra calculations, Dr. Marcus Scheele for providing equipment for the PL measurements in solution, Benjamin Wagner for his great effort on the electron density fits, and Dr. Jiří Novák (Masaryk University) for his productive support and fruitful discussion on the X-ray diffraction results.

I would like to acknowledge with thanks the following people for being a part of the beamtime experiments: Clemens Zeiser, Jakub Rozbořil, Berthold Reisz, Giuliano Duva, Timo Storzer. The beamtimes would not be possible without generous granting by the ESRF, the SLS, and Soleil and helpful assistance of the staff of the ID10 (ESRF), the MS-Surf. diffraction (SLS), and SixS (Soleil) beamlines.

I have to thank Hanna Maurer and Aleksandra Rötschke for their thoughtful assistance with administrative tasks and also Bernd Hofferberth who always came up with prompt and smart solutions of technical problems. I wish to express my sincere thanks to Jan Hagenlocher, Martin Hodas, Antoni Franco-Canellas, Madeleine Fries, Olga Matsarskaia, Oleg Vladimirov, and the rest part of the Soft Matter group for proofreading of the thesis and for continuous encouragement, support, and help.

I also place on record, my sense of gratitude to my parents for all their love and care which have made all the work possible.